

A590211

Dz. 6

POLISH ACADEMY OF SCIENCES – WROCLAW BRANCH
WROCLAW UNIVERSITY OF TECHNOLOGY

ISSN 1644-9665
INDEX 375667



ARCHIVES
OF CIVIL AND MECHANICAL
ENGINEERING

Quarterly
Vol. VII, No. 1

WROCLAW 2007

ADVISORY COMMITTEE

<i>Chairman</i> – JAN KMITA ¹	ADOLF MACIEJNY (Poland)
JAN BILISZCZUK (Poland)	ZDZISŁAW MARCINIAK (Poland)
CZESŁAW CEMPEL (Poland)	KAZIMIERZ RYKALUK (Poland)
JERZY GRONOSTAJSKI (Poland)	ANDRZEJ RYŻYŃSKI (Poland)
ANTONI GRONOWICZ (Poland)	ZDZISŁAW SAMSONOWICZ (Poland)
M.S.J. HASHMI (Ireland)	WOJCIECH SZCZEPIŃSKI (Poland)
HENRYK HAWRYŁAK (Poland)	PAWEŁ ŚNIADY (Poland)
RYSZARD IZBICKI (Poland)	RYSZARD TADEUSIEWICZ (Poland)
WAĆLAW KASPRZAK (Poland)	TARRAS WANHEIM (Denmark)
MICHAEL KETTING (Germany)	WŁADYSŁAW WŁOSIŃSKI (Poland)
MICHAŁ KLEIBER (Poland)	JERZY ZIÓLKO (Poland)
VADIM L. KOLMOGOROV (Russia)	JÓZEF ZASADZIŃSKI (Poland)

EDITORIAL BOARD

<i>Editor-in-chief</i> – JERZY GRONOSTAJSKI ²	ANDRZEJ KOCANĀDA (Poland)
ROBERT ARRIEUX (France)	WAĆLAW KOLLEK (Poland)
AUGUSTO BARATA DA ROCHA (Portugal)	PIOTR KONDERLA (Poland)
GHEORGHE BRABIE (Romania)	ZBIGNIEW KOWAL (Poland)
LEŚLAW BRUNARSKI (Poland)	TED KRAUTHAMMER (USA)
EDWARD CHLEBUS (Poland)	ERNEST KUBICA (Poland)
LESZEK F. DEMKOWICZ (USA)	CEZARY MADRYAS (Poland)
KAZIMIERZ FLAGA (Poland)	TADEUSZ MIKULCZYŃSKI (Poland)
YOSHINOBI FUJITANI (Japan)	HARTMUT PASTERNAK (Germany)
FRANCISZEK GROSMAN (Poland)	MACIEJ PIETRZYK (Poland)
MIECZYŚLAW KAMIŃSKI (Poland)	EUGENIUSZ RUSIŃSKI (Poland)
<i>Scientific secretary</i> – SYLWESTER KOBIELAK	HANNA SUCHNICKA (Poland)

¹ The Faculty of Civil Engineering, Wrocław University of Technology
Wybrzeże Wyspiańskiego 27, 50-370 Wrocław, Poland
Tel. +48 71 320 41 35, Fax. +48 71 320 41 05, E-mail: jan.kmita@pwr.wroc.pl

² The Faculty of Mechanical Engineering, Wrocław University of Technology
ul. Łukasiewicza 5, 50-371 Wrocław, Poland
Tel. +48 71 320 21 73, Fax. +48 71 320 34 22, E-mail: jerzy.gronostajski@itma.pwr.wroc.pl

POLISH ACADEMY OF SCIENCES – WROCLAW BRANCH
WROCLAW UNIVERSITY OF TECHNOLOGY

ARCHIVES OF CIVIL AND MECHANICAL ENGINEERING

Quarterly
Vol. VII, No. 1

WROCLAW 2007

EDITOR IN CHIEF

JERZY GRONOSTAJSKI

EDITORIAL LAYOUT AND PROOF-READING

EWA SOBESTO, pp. 1–84

WIOLETTA GÓRALCZYK, pp. 85–100

TYPESETTING

SEBASTIAN ŁAWRUSEWICZ

SECRETARY

TERESA RYGLOWSKA

Publisher: Committee of Civil and Mechanical Engineering
of Polish Academy of Sciences – Wrocław Branch,
Faculty of Civil Engineering and Faculty of Mechanical Engineering
of Wrocław University of Technology

© Copyright by Oficyna Wydawnicza Politechniki Wrocławskiej, Wrocław 2007

OFICYNA WYDAWNICZA POLITECHNIKI WROCŁAWSKIEJ

Wybrzeże Wyspiańskiego 27, 50-370 Wrocław

<http://www.oficyna.pwr.wroc.pl>

e-mail: oficwyd@pwr.wroc.pl

ISSN 1644-9665

Drukarnia Oficyny Wydawniczej Politechniki Wrocławskiej. Zam. nr 243/2007.

Contents

T. BŁASZCZYŃSKI, A. ŁOWIŃSKA-KLUGE, Experimental investigation and assessment of damage in the case of swimming-pool repairs.....	5
D. PAWLUS, Critical static loads calculations in finite element method of three-layered annular plates	21
D. SZELIGA, M. PIETRZYK, Testing of the inverse software for identification of rheological models of materials subjected to plastic deformation	35
J. RYSZKOWSKA, J. RĘBIŚ, M. LANGNER, Polyurethane coating for protecting concrete floors using the system with fillers produced by recycling	53
W. KOLLEK, Z. KUDŹMA, M. STOSIAK, J. MACKIEWICZ, Possibilities of diagnosing cavitation in hydraulic systems	61
B. REIFUR, Optimum assembly automation level selection module as the component of advisory system	75
J. PRZONDZIONO, D. HALACZEK, J. SZYMSZAL, Determination of the flow curves of austenite steel wire in the drawing process	85
I. SCHINDLER, M. LEGERSKI, P. SUCHÁNEK, S. RUSZ, M. JANOŠEC, R. PACHLOPNIK, Deformation behaviour of low carbon deep-drawing steels influenced by phase transformation	93

Spis treści

T. BŁASZCZYŃSKI, A. ŁOWIŃSKA-KLUGE, Diagnostyka uszkodzeń basenów kąpielowych	5
D. PAWLUS, Obliczenia krytycznych obciążeń statycznych trójwarstwowych płyt pierścieniowych metodą elementów skończonych	21
D. SZELIGA, M. PIETRZYK, Testy numeryczne oprogramowania do analizy odwrotnej do identyfikacji parametrów reologicznych materiałów odkształczanych plastycznie	35
J. RYSZKOWSKA, J. RĘBIŚ, M. LANGNER, Poliuretanowe pokrycia do ochrony betonowych posadzek z wypełniaczem pochodzącym z recyklingu	53
W. KOLLEK, Z. KUDŹMA, M. STOSIAK, J. MACKIEWICZ, Możliwości diagnozowania kavitacji w układach hydraulicznych	61
B. REIFUR, Moduł wyboru optymalnego poziomu automatyzacji montażu jako składnik systemu doradczego	75
J. PRZONDZIONO, D. HALACZEK, J. SZYMSZAL, Wyznaczanie krzywych umocnienia drutów ze stali austenitycznych w procesie ciągnięcia	85
I. SCHINDLER, M. LEGERSKI, P. SUCHÁNEK, S. RUSZ, M. JANOŠEC, R. PACHLOPNIK, Wpływ przemiany fazowej na plastyczność niskowęglowej stali do głębokiego tłoczenia	93



Experimental investigation and assessment of damage in the case of swimming-pool repairs

TOMASZ BŁASZCZYŃSKI, ALDONA ŁOWIŃSKA-KLUGE

Poznań University of Technology, ul. Piotrowo 5, 60-965 Poznań

The paper deals with the problems connected with the assessment (diagnostic testing) and repair of swimming pools. In block diagrams, the successive stages of diagnostic testing are shown. The corrosive environment of swimming pools is also presented. Theoretical assumptions were applied to the assessment and repair of one of damaged swimming pools. The results of the site investigations and some microscopic and chemical examinations are discussed. The ways of repairing swimming pools are shown.

Keywords: *assessment (diagnostic testing), structural and non-structural damage, durability, swimming-pool repair*

1. Introduction

Swimming pools are the objects which during the long-standing exploitation must be durable and hermetic. Each swimming pool has to meet the following requirements:

- a correct creation of structure,
- a proper selection and assembly of the fittings,
- the selection of the proper finishing and protective systems,
- a correct technology of their building in.

The adaptation of the system solutions only is important. In the designs of open swimming pools, their resistance to an internal water pressure has to be taken into account. Their facing ought to be resistant to chemical compounds and all system – to variable weather conditions.

Swimming pool is made of two types of materials (Figure 1):

- structural materials,
- finishing and protective materials.

Traditional swimming pools should be made of a waterproof concrete, grade B25 at least, resistant to cracks and to chemical environment. Most often the waterproofness of $>W-6$ and an ultimate width of crack opening $w_{lim} = 0.1$ mm are taken into account. Additionally we have to remember that according to PN-EN 206-1:2003 [1] the water environment of swimming pool is qualified as XD2, which also imposes ultimate conditions on the composition of concrete and its basic features.

Due to complex swimming pool fittings a large number of ducts pass through its trough, which in consequence may be the cause of leaks. Indispensable dilatations pose the next technical problem that should be solved. Correctly done finishing and

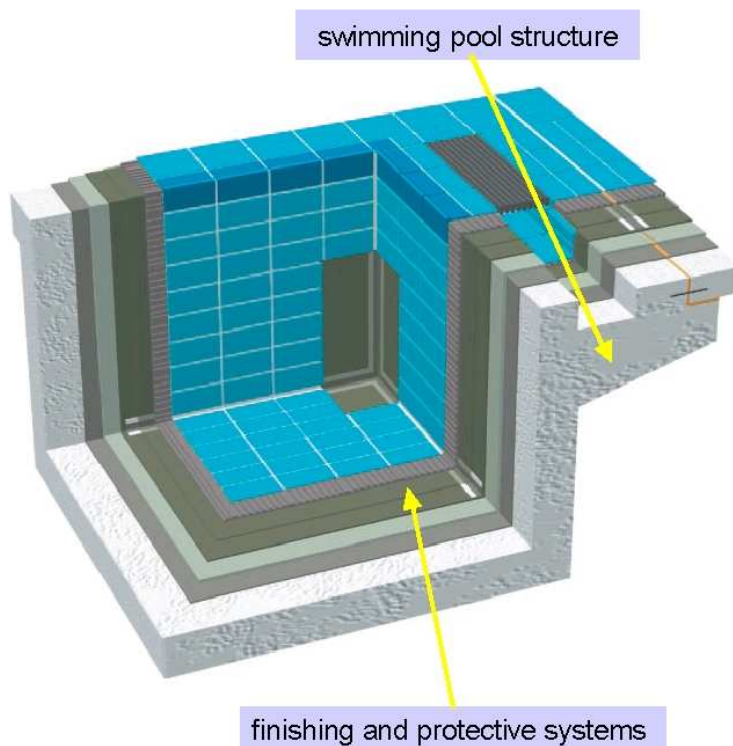


Fig. 1. Swimming-pool components

protective works are not less important than the suitable waterproofness of the concrete used. The efficiently working pool system consists of waterproof elements. A basic component of such a system is watertight mortar, fulfilling the role of damp-course, and supplementary elements are cement-based glue mortar and joint mortar. In the case of traditional swimming pools, the finishing is made of ceramics or glass mosaic.

2. Swimming-pool environment

A basic environment affecting the swimming pool is water. It is always a very weak solution of salts, acids, alkali and gases. Besides solutes also colloidal systems and suspensions can be present. Additionally in a closed reservoir, water is continuously polluted by bathers. In the case of the open swimming pool, rainfall interference must be taken into account. Therefore a constant cleaning of such a water is indispensable. Basic methods for pool water cleaning are mechanical filtration, coagulation, disinfection and pH adjusting. During cleaning the swimming-pool water usually all these processes take place.

The coagulation process allows us to remove colloidal system from water. Because of very small diameters (1–100 μm) it cannot be eliminated simply by filtration alone. As the most common coagulant a technical aluminium sulphate is used. However recently more and more often coagulants based on PAC (i.e., solution of the polyvinyl chloride of aluminium) are employed.

The pool water disinfection consists in introducing such strong oxidants as gaseous chlorine, chlorine dioxide, sodium hypochlorite, calcium hypochlorite, trichloroisocyanic acid, ozone and UV radiation into the water. Ozone and UV radiation only facilitate the disinfection process. The chlorination of the inflow water is necessary for enhancing the effect of disinfection in swimming pools, where microorganisms are constantly present. In order to encourage the disinfection efficiency and coagulation, pH adjustment is indispensable. Optimum disinfection results are obtained at pH range of 7–7.5. As a result of chlorination, pH of water in pool should be decreased. A 10% solution of sulfuric acid is most often used to reduce pH. In order to increase pH, 10% solution of the sodium carbonate is usually added.

Admissible concentrations of chemical compounds in pool water are as follows:

- free chlorine content in water: 0.3–0.5 mg/dm^3 ,
- chemically bounded chlorine content in water: 0.2–0.3 mg/dm^3 ,
- ozone content in water: 0.05 mg/dm^3 ,
- THM content in water: 0.02 mg/dm^3 .

The water temperature in swimming pools should range from 25 to 34 $^{\circ}\text{C}$.

3. Assessment of swimming pools

Swimming pools as other structures during their service life should be characterized by definite functional quality. The idea of functional quality, accepted by the European Union in the Directive No. 89/106/ECC [2], creates the basis for a new formulation of requirements for building engineering. Also the Polish building code is based on this Directive [3].

In spite of the above during swimming-pool exploitation many problems arise. More and more seldom the problems with a faulty foundation of pool trough occur. The proportion of the problems connected with the selection of concrete and reinforcement and also with placing the concrete is also smaller. Lately most problems lie in the swimming-pool tightness. This is the water test that allows us to check whether or not the RC pool trough is tight. After finding leaks their causes have to be found. Most frequently we deal with shrinkage cracks or structural cracks which ought to be filled by injection and thus water-tight.

In most cases, the tightness of swimming pools is not affected by the structure conditions, but by finishing and protective technologies. The quality of the materials used in all layers, including external facing, is also important.

Dealing with the damage to swimming pools, first we have to set out their causes which allow development of the repair concept. This process can be called the diagno-

sis of the existing state. The development of the repair concept and the methods of its realization, and then the choice of the materials or systems for the direct use are the domains of the repair process (Figure 2).

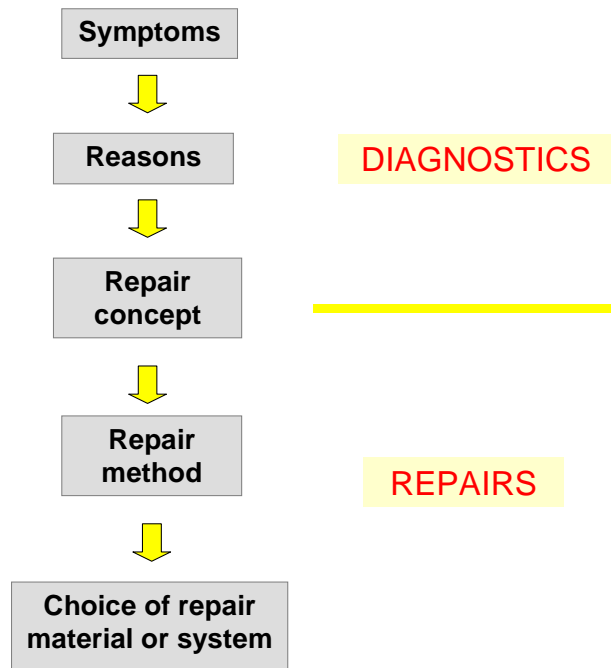


Fig. 2. The block diagram of the diagnostics–repair process

The diagnostic process can be based on a general block diagram proposed by Ciesielski [4]. It consists of the block of assumptions, the block of operations, the block of results and the block of diagnosis. Taking into account the swimming-pool specificity as a complex structure, special attention must be paid to the block of analysis hidden in Ciesielski's diagram, in the block of diagnosis. In the case of pools, the range of the works performed in this stage is comprehensive (Figure 3).

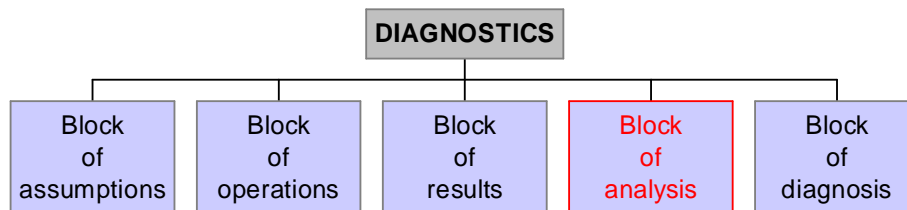


Fig. 3. The modification of Ciesielski's diagnostic scheme

The block of operations consists, among others, of site investigation of cracks and other damage. Further it takes into account indispensable outcrops both from the inside and outside of the basin trough (Figure 4).

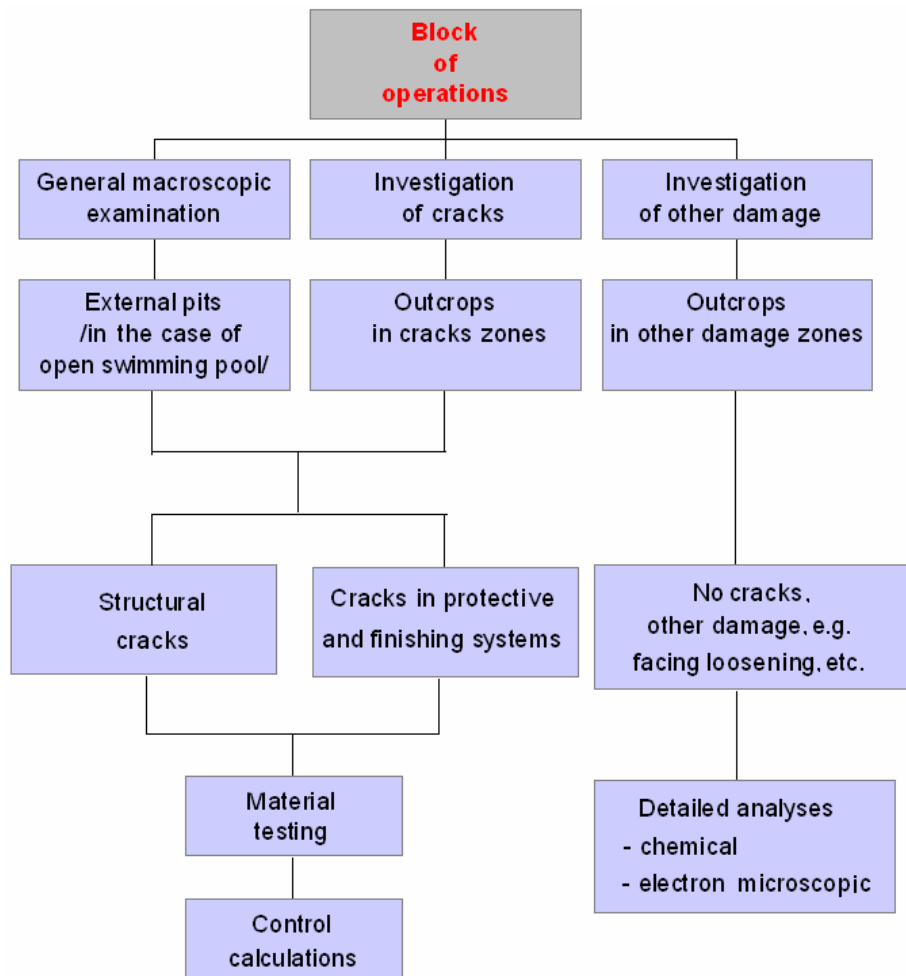


Fig. 4. The block of operations in the case of swimming-pool diagnosis

If cracks appear, one ought to check whether they are only in the finishing and protective zones or also in the structure itself and whether they are through cracks. The structural material testing and control calculations also must be done. If there are no cracks, but other damage appears, e.g., facing loosening, then detailed chemical analyses and examinations under electron microscope are indispensable. This is especially important in the era of more and more modern and complicated technologies swimming-pool design.

In the block of diagnosis, we compare technical parameters with codes of practice and admissible conditions. A final diagnosis underlies the proposed technology of future repair process (Figure 5).

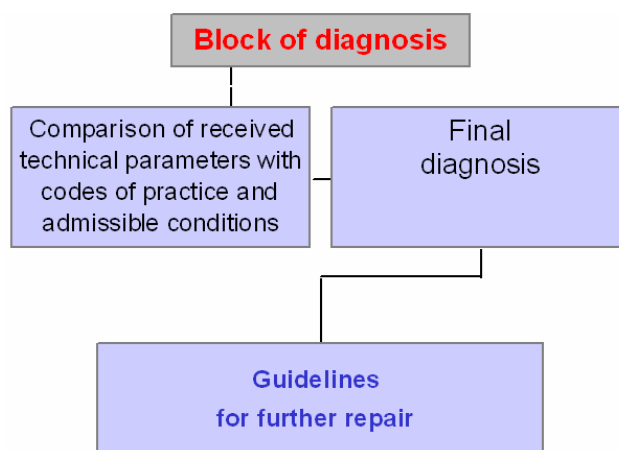


Fig. 5. The block of diagnosis in the case of swimming pool

As is commonly known, it is necessary to see the effect of damage, to explain its causes and next to develop the concept of its repair. Now we can design the repair algorithm leading us to an efficient repair method and a right choice of materials or repair system.

The European PN-EN 1504-1:2000 code [5] has introduced classification of repair works into the following kinds:

- structural repair,
- non-structural repair,
- surface protection.

Nowadays, in the case of swimming pools, most often we deal with two last kinds of repair.

The first group of repair deals mostly with crack repair. In the case of structural cracks, their repair should be done by means of the materials based on polyester resins. If the tightness is the only problem and simultaneously the elasticity should be maintained, materials based on polyurethane resins must be used.

Non-structural repair and surface protection of swimming pools refer to facing and protection zone. These can be partial repair or repair in some of layers. Also the whole damaged swimming-pool system may often be replaced with a new one.

4. Case study investigations

A practical application of diagnostic testing and repair process was described based on one of damaged swimming pools. After about one-year of exploitation of this

swimming pool a facing upthrust on the ground slab was noticed. Therefore we decided to empty the swimming pool and to assess the extent of its damage (Figure 6).

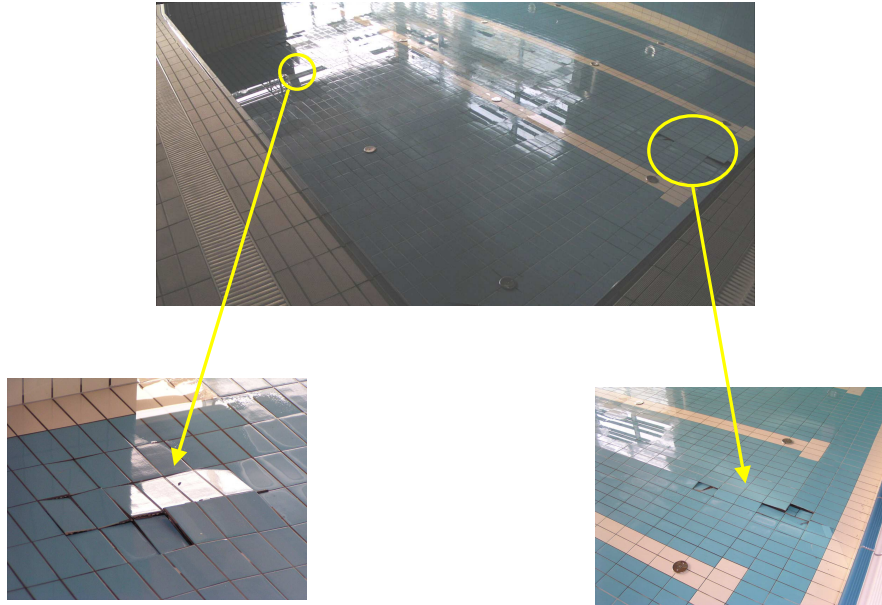


Fig. 6. The upthrust zones of ceramic tiles in the swimming pool investigated

It was noticed that ceramic tiles had loosened within cement-based glue mortar, hence a thin waterproof layer was almost clean. There were also the places where mortar glue was coming off the waterproof layer and ceramic tiles. On the third day after emptying the pool the mortar glue dried up and its structure changed. Practically, for the first 10 days after emptying the pool the ceramic tiles in the upthrust zones could be loosened by hand.

After removing the ceramic tiles from the ground slab, the water from under the wall ceramic tiles was continuously flowing out. Also the outcrops at the considerable distance from the upthrust zones were done. Ceramic tiles were locally removed and a hydrated glue mortar in the form of the white greasy substance appeared below them (Figure 7). The samples of this mortar were taken for further laboratory tests. The same phenomenon as that in the ground slab was also observed in the case of walls. After a total removal of ceramic tiles, only local loosening of damp-course was observed.

4.1. Site investigation

The diagnostic and repair process, whose scheme is shown in Figure 2, began with the attempts to identify the immediate cause of damage. Accordingly the method of

experimental diagnostics based on the modified block scheme presented in Figure 3 was used. After completing the works specified in the block of assumptions and after the works done according to the scheme from Figure 4 detailed laboratory analyses were carried out.

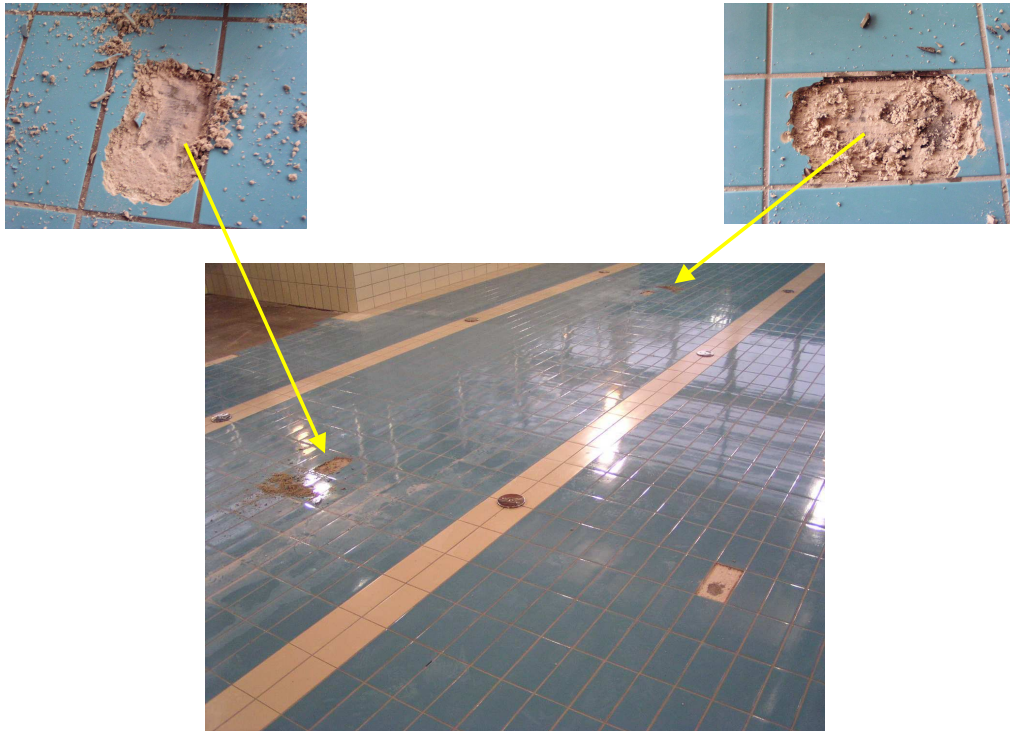


Fig. 7. Outcrops of ceramic tiles on the ground slab outside the upthrusts

4.2. Experimental investigation

4.2.1. Examination of specimens under electron microscope

The collected cement-based mortar glue specimens were examined under electron microscope. The examination was done with scanning electron microscope, VEGA TS 5135 MM type, at a high vacuum in secondary electrons, on the samples metallized with platinum and at a low vacuum in backscattered electrons on non-metallized samples. During examination characteristic features of surface topography were digitally registered.

In the case of the samples collected from the ground slab of the swimming pool (samples No. 1 and 2), we can observe (Figure 8) relatively loose structures formed

during cement hydration, in the form of crystallites and gel: fine-crystalline portlandite with a predominance of lamellar forms, fine-crystalline and gelatinous phases of tobermorite, ettringite and organic compounds in the form of loose balls.

In the case of the samples collected from the wall of the swimming pool (sample No. 3), we can observe (Figure 9) the structures formed during cement hydration in the form of crystallites and gels: portlandite with a predominance of lamellar forms, fine-crystalline and gelatinous phases of tobermorite, copious amounts of ettringite and organic compounds in the form of loose balls and the balls that adhere to each other.

Large quantity of fine-fibrous ettringite indicates that some local sulfuric corrosion centers are formed.

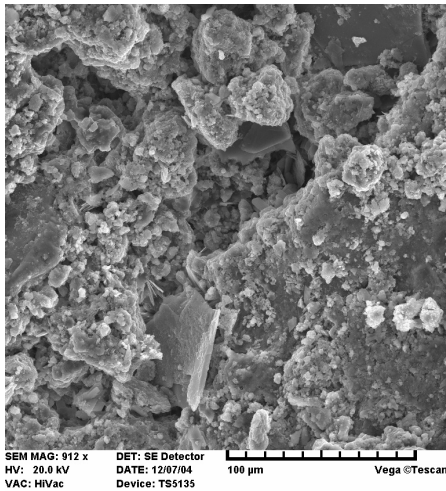


Fig. 8. Photomicrograph of sample No. 1

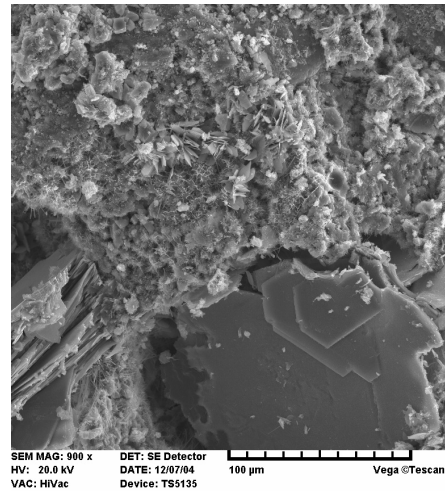


Fig. 9. Photomicrograph of sample No. 3

Additionally the test of “witness sample” (sample No. 4) was performed under laboratory conditions.

In the case of “witness sample” we can also observe (Figure 10) the structures formed during cement hydration in the form of crystallites and gels: portlandite with a predominance of lamellar forms, fine-crystalline and gelatinous phases of tobermorite, ettringite, and organic compounds in the form of foils, agglomerates, fibres and the balls adhering to each other.

Standardless EDS microanalyses in low-vacuum mode have been performed for the products of the reactions occurring in mortars taken from the pool (samples No. 1–3) and in “witness sample” (sample 4) after its hydration. It was found that calcium prevailed in mortars, while the concentration of other elements detected, i.e., C, O, Mg, Al, S, Na, K, was low (Figure 11).

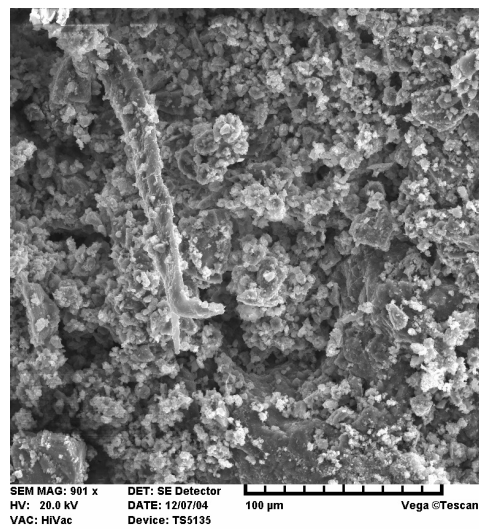


Fig. 10. Photomicrograph of sample No. 4 – “witness sample” after hydration

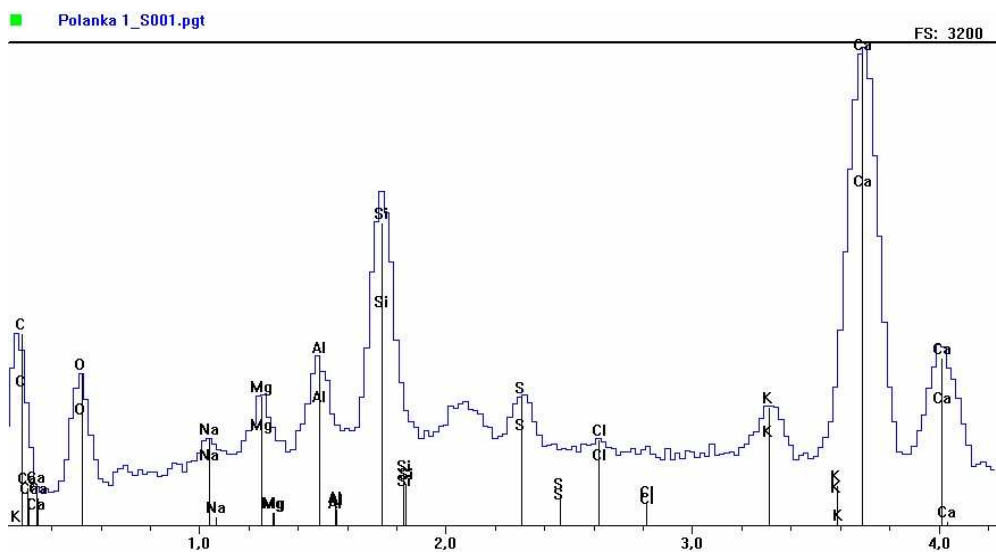


Fig. 11. Standardless EDS microanalyses of reaction products in sample No. 1

This finding pointed to a lack of a polymer net formed in a proper way. Much higher concentration of carbon as well as Ca, O, Si, S, Al and K in sample No. 4 (“witness sample” after hydration) proved that cement and polymer nets were properly formed (Figure 12).

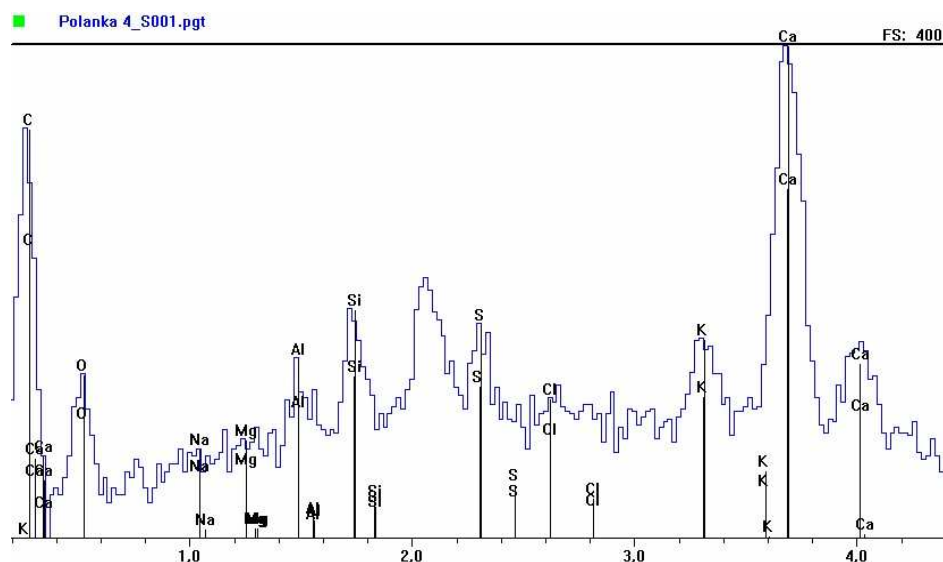


Fig. 12. Standardless EDS microanalyses of reaction products in sample No. 4

4.2.2. Chemical tests

Two kinds of chemical tests were carried out:

- the determination of inorganic compounds,
- the determination of organic compounds.

In the samples of mortar glue collected from the pool (samples No. 1, 2 and 3) and in the “witness sample” made of green mortar (sample No. 4), the content of basic inorganic compounds was determined. Additionally pH was measured. The results obtained are presented in Table 1.

Table 1. The content of inorganic compounds in the samples collected

Composition of samples	Sample number			
	1	2	3	4
CaO [%]	21.94	24.64	24.69	29.10
MgO [%]	0.40	0.35	0.35	0.40
Cl ⁻ [%]	traces below the determination threshold			
SO ₄ ²⁻ [%]	0.83	0.96	1.18	1.22
pH	11.22	11.22	11.28	11.39

In the samples No. 1–3, the content of calcium compounds (from ~22% to ~25%) was lower than that in the “witness sample” (over 29%). This can be the result of washing out the calcium compounds from the mortar glue. In all the samples, the

content of magnesium compounds is fairly similar (within the limits of error). The content of sulphates in the samples No. 1–3 is lower (from ~0.83% to ~1.18%) than in the “witness sample” No. 4 (1.22%), which creates unfavourable conditions for chemical corrosion. pH of the samples collected from the pool (the samples No. 1–3) is slightly lower than pH of the “witness sample” (the sample No. 4).

In the mortar glue samples from the pool (samples No. 1, 2 and 3) as well as in the “witness samples” made of green mortar (the sample No. 4 bis) and in green mortar after its hydration (the sample No. 4), the content of organic parts was determined (Table 2).

Table 2. The content of organic compounds in the samples tested

Sample number	Sample mass before roasting m_0 [g]	Sample mass after roasting m_1 [g]	Content of organic parts [percentage by weight]	Average content of organic [parts percentage by weight]
1 a	2.1613	1.1613	8.63	8.6
1 b	0.9013	0.8233	8.66	
2 a	1.6138	1.4873	7.84	8.1
2 b	0.8416	0.7711	8.38	
3 a	1.3610	1.2128	10.9	10.7
3 b	1.8983	1.6995	10.47	
4 bis a	0.9550	0.9165	4.03	4.1
4 bis b	1.5399	1.4759	4.16	
4 a	1.5220	1.4445	5.10	4.9
4 b	1.4633	1.3938	4.75	

In the samples No. 1–3, the content of organic parts was twice as high as that of “witnesses” samples (4 and 4 bis) both before and after their hydration. These results provide evidence of adding some supplementary dispersing agent, which improves the mortar glue characteristics.

The results of laboratory tests allowed the causes of the phenomena observed to be identified.

5. Case study assessment

A detailed site investigation of the swimming-pool structure revealed its good technical condition (no external cracks and other defects) and no signs of water leaks. This indicated that the damage took place above the waterproof layer. The waterproof layer adhered properly to a whole surface of concrete which proved that the latter had been prepared properly. Ceramic tiles were put down on an elastic mortar glue. This mortar was a hydraulically binding thin-layer glue based on cement, modified by polymer and supplemented with fibres. The physical properties of such a mortar glue are the best when cement and polymer nets are developed. They penetrate mutually, which makes them stronger and satisfactorily complete.

Chemical tests revealed that the conditions in the pool were unfavourable to a chemical corrosion, though on some micrographs the signs of this process appeared. On the basis of chemical tests and microscopic examination it can be concluded that calcium compounds are washed out from cement part of mortar glue, which deteriorates its compactness due to a partial disintegration of its structure. This phenomenon is observed first of all in the samples No. 1 and 2, collected from the bottom of pool slab, and also, to lesser extent, in the sample No. 3, taken from the pool wall. This testifies to the weakness of the cement-based net. When assessing the content of organic compounds it was revealed that in the samples collected from the pool the content of polymer was more than twice as high as that in the “witnesses” samples. This can prove that a modifier was added into the used mortar glue. We do not know the reason for such a decision and at which stage it was undertaken. Perhaps the used mortar glue approached the limit of its service life.

An internal polymer network is considered to be the next important feature of mortar glue. Mechanical properties of polymers depend greatly on the degree of their polymerisation as well as the kind and quantity of their additional components. Polymers are degraded by UV radiation, oxygen, water and temperature. Some polymers swell in the water. The powdered resins that form polymers release water. Because the water passes into the mortar glue, it has to be evaporated, otherwise the resin not be properly dispersed, because the binding processes do not proceed in a proper way. In such a case only agglomerates should be formed. Microscopic examinations of the mortar glue samples collected from the pool revealed only dispersed and concentrated balls, sometimes only beads of balls. Because of the above the mortar glue was not characterized by the features required.

In the case of organically modified glues, the joints should be opened for the period of approx. 5 to 7 days. During that time the reticulation processes take place. They allow the water released to be evaporated. After the seventh day the polymers lose their ability to reticulate. Non-evaporated water suspends the process of mortar glue binding, which can be observed on microscopic photos as the lack of agglomerates and the occurrence of separate polymer balls. If the setting of mortar glue is appropriate, polymer balls appear only locally (compare Figure 10).

Filling the joints of tiles just after 24 hours, which is recommended by the system manufacturer, is a technological error, leading to above phenomenon. The results of additional tests carried out on the joint watertightness showed that water permeated these joints, hence some additional water was penetrated the mortar glue, causing its gradual degradation, both by preventing the formation of the cement and polymer nets and by destroying them. Because there was no chemical corrosion and the mortar glue was highly hydrated, the progressive degradation of mortar glue inner structure occurred due to physicochemical corrosion.

The physicochemical deterioration of the structure of cement-based materials by surface-active liquid (as water) occurs due to:

- the surface energy drop in the structure of solid,

- the unbinding effect.

On one hand water allows the development of cement-based network, but on the other one it is responsible for its getting damp. In such a case, free water particles (which are strongly polar) in microspaces cause unbinding and hence weak the mortar structure. A decrease in the strength of hydrated cement-based materials is explained by the phenomena which take place at the solid–liquid interface, and also by the change in a free surface energy. A decrease in tensile axial strength due to water is larger than compressive strength. The strength of wet porous materials results from the interfacial surface pressure and the unbinding effect. This effect takes place at the polar fluid (water)–solid interface. When a microcrack or other microdefect occurs the polar molecules move along its surface to the apex. Therefore, at the apexes, microcracks and other microdefects are subjected to pressure. The polar molecules adsorbed on the surface reduce the surface energy, which can make this surface more ductile.

Taking account of the above we can conclude that getting damp of the mortar glue and its continuous hydration due to the untight joints is the primary cause of damage. The process of physicochemical corrosion, and especially the unbinding effect, brought about a fundamental weakness at the point where a waterproof layer came into contact with mortar glue. The lack of adhesion in this zone and natural deformations of pool trough caused the loss of stability in the plane of tile, which were connected only by joints. This led to facing loosening within the waterproof layer and the upthrust. The water still penetrating the mortar intensifies this process and allows the finishing tile layer to be loosened by hand. Because of such a condition of the mortar glue even the smallest stresses in the pool trough zone cause the facing loosening. We did not observe chemical corrosion induced by the chlorine action, which can be explained by the mortar glue resistance or a protective action of the joints.

6. Repair process

After assessing the causes of the waterpool damage the repair procedure could be carried out. Since the existing water-proof layer quite firmly adhered to the pool surface, the decision about its maintenance could be undertaken. On the other hand, its removal would unnecessarily increase the cost of all repair works. To be able to assess univocally the adhesion of new water-proof layer to the existing pool surface (with the existing water-proof layer), we had to carry out some preliminary pull-off tests. The test revealed that the adhesion of new layers to the existing surface reached on average 1.08 MPa, which was twice as much as the standard required.

After investigating the swimming-pool surface the repair technology was developed. In the case analyzed, a totally new finishing and protective system was installed. This system is composed in such a way that particular layers improve its waterproofness. This means that not only the waterproof layer is tight, but mortar glue and joints have to be tight (waterproof) as well. Technical details of the repair technology are presented in Figure 13.

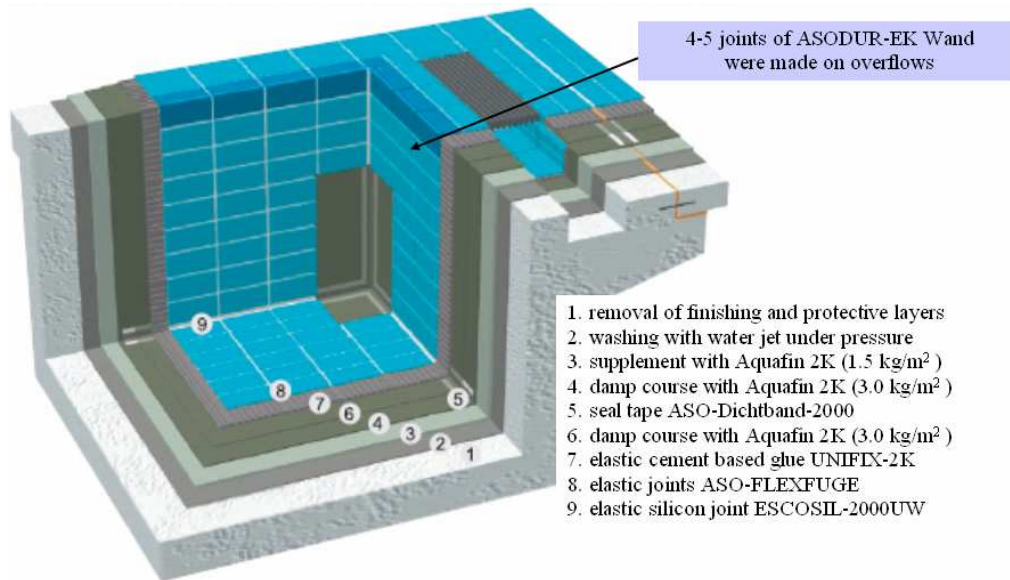


Fig. 13. The technology of repair works

7. Conclusions

In the assessment of swimming-pool technical condition, the method of its repair is of a prime importance. Diagnostic testing should be complex independently of the method used. Sometimes special laboratory tests ought to be done.

Due to significant differentiation of the materials and their purposes it is difficult to select a proper repair technology. This process is important, because it often affects greatly the repair efficiency. A close and effective cooperation between various elements of repair system (the compatibility in different repair phases and future exploitation conditions) is principal and indispensable condition of each repair. However, even the best repair system can prove to be ineffective, if the assessment of its technical condition is inaccurate or false.

References

- [1] PN-EN 206-1:2003. Concrete – Part 1: *Specification, performance, production and conformity*.
- [2] The Council of the European Communities Directive 89/106/ECC.
- [3] Act from 7.07.94. Polish building code (Law gazette, 2003, No. 207, entry 2016 with later amendments).

- [4] Ciesielski R., *Diagnostics and technical state assessment of engineering structures in terms of the construction materials used* (in Polish), Proceedings of XX Structural Failure Conference, Szczecin-Międzyzdroje, 2001, 171.
- [5] PN-EN 1504-1:2000. *Products and systems for the protection and repair of concrete structures. Definitions, requirements, quality control and evaluation of conformity. Part 1: Definitions.*

Diagnostyka uszkodzeń basenów kąpielowych

Praca dotyczy zagadnień związanych z diagnostyką i naprawami basenów kąpielowych. Omówiono środowisko korozyjne oddziałujące na baseny kąpielowe. Przedstawiono kolejne etapy postępowania w formie układów blokowych. Przyjęte założenia teoretyczne zastosowano do diagnozowania i naprawy jednego z uszkodzonych basenów. Przedstawiono kolejne efekty badań przeprowadzonych na obiekcie oraz badań laboratoryjnych (elektrono-mikroskopowych i chemicznych). Na zakończenie omówiono przyjęte technologie naprawy.



Critical static loads calculations in finite element method of three-layered annular plates

D. PAWLUS

University of Bielsko-Biała, ul. Willowa 2, 43-309 Bielsko-Biała

This paper presents the results of critical, static loads calculations of three-layered, annular plates with a soft core. The plate with slidably clamped edges, uniformly loaded with compressive stress on the inner edges of outer layers and of the symmetric cross-section structure is the subject of consideration. In the description of deformation of layers, the assumption of the equal deflections of plate layers has or has not been used. The calculations were carried out for several plate models built of finite elements using the system ABAQUS. The analysis of the distribution of values of critical loads, depending on various thicknesses of plate core, different values of facing thicknesses and on two kinds of core foam material of different stiffnesses, indicates some essential results, which are important in the plate stability problems. Among them the observation of possible area of too high values of critical loads shows the limitation of usage of rather universally applied assumption of equal layers deflections in cross-section deformation of the plates with thick core. This conclusion seems to be particularly important for designers.

Keywords: *critical loading, sandwich annular plate, numerical models, finite element method, ABAQUS*

1. Introduction

The solution to the stability problem of three-layered annular plate with soft core presented in [1, 2] is based on the classical theory of sandwich plate with the broken line hypothesis [3]. The numerical calculations were performed using the approximation finite difference method. This analysis from the viewpoint of quantitative evaluation of the values of critical static loads and qualitative analysis of deformation forms of plates and their critical behaviours could be supplemented by the suggested (in this paper) calculations carried out using the finite element method, which yield the essential development in comparison to the observations presented earlier in [4].

Using the possibilities offered by the finite element method in the range of structure of computational plate model differing in the type of finite elements and arrangement of finite elements in the model mesh in relation to the additional geometric and kinematic constraints, the domain of problem analysis could be suitably wider and due to this, even more inquiring. The conclusions drawn from the observation of the deformation forms of plates with thick, soft core corresponding to minimal values of critical static loads or the influence of the structure in finite element method of plate model on the investigation results presented in this paper can inform us about certain possibilities and limitations of the solution to the undertaken problem using the two indicated methods: the finite difference method in [1, 2] and the finite element method universally applied in engineering calculations.

2. Problem formulation

The three-layered, annular plate built of thin, steel facings and a soft, foam core is the subject of the analysis. The example of plate with slidably clamped inner and outer edges subjected to a uniformly distributed compressive, radial stress loading the inner edges of plate facings is considered. The scheme of the plate under analysis is presented in Figure 1. The cross-sectional system of plate layers is symmetric, the thicknesses and materials of facings are the same. The numerical calculations have been carried out for the plates exemplifying the following geometrical and material parameters:

- the inner radius $r_i = 0.2$ m;
- the outer radius $r_o = 0.5$ m;
- the facing thicknesses (equal for each facing) $h' = h_1 = h_3$, $h' = 0.0005$ m or $h' = 0.001$ m;
- the core thicknesses $h_2 = 0.025$ m, 0.005 m, 0.01 m, 0.02 m, 0.04 m, 0.06 m;
- the steel facing material: Young's modulus $E = 2.1 \cdot 10^5$ MPa and Poisson's ratio $\nu = 0.3$;
- two kinds of polyurethane foam as a core material with the value of Kirchhoff's modulus $G_2 = 5$ MPa [5] and $G_2 = 15.82$ MPa [6], equal value of Poisson's ratio $\nu = 0.3$ accepted in accordance with the PN-84/B-03230 and the values of Young's modulus $E_2 = 13$ MPa and $E_2 = 41.13$ MPa calculated assuming that the foam is isotropic material.

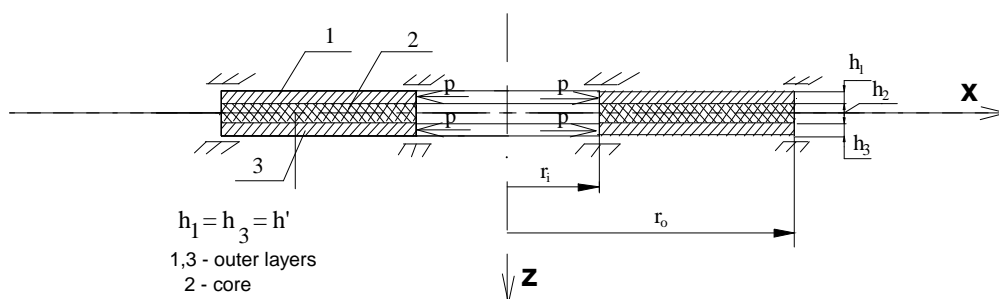


Fig. 1. The scheme of the plate

The critical static load calculations were carried out for elastic plate core, solving the eigenproblem.

3. Computational plate models

The numerical calculations were carried out for several plate models built of finite elements. The plate models under analysis are as follows:

- The model in the form of a full annulus (Figure 2) composed of 9-node 3D shell elements and 27-node 3D solid elements creating the facing and core meshes, respectively.

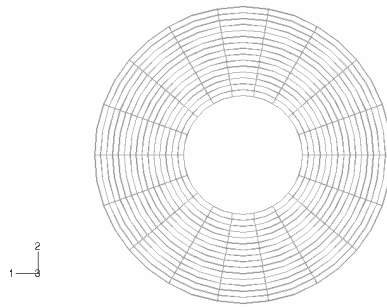


Fig. 2. The full annulus plate model

- The model in the form of an annular sector (1/8 part) with a proper formulation of symmetry conditions on the partitioned edges. The facings are also built of 9-node 3D shell elements. The 27-node 3D solid core elements are arranged in single or double layers presented in Figures 3 and 4, respectively.

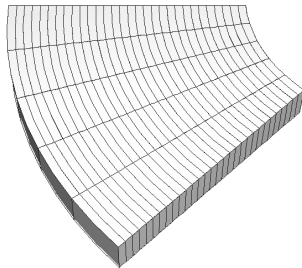


Fig. 3. The annular sector of plate model with the single layer of core elements

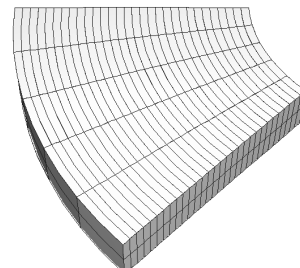


Fig. 4. The annular sector of plate model with the double layers of core elements

- The model in the form of a radial sector of a plate built of axisymmetric elements: shell 3-nodes and solid 8-nodes arranged in single, double or quaternary core mesh layers presented in Figures 5, 6, 7, respectively.



Fig. 5. The plate model with single core layer

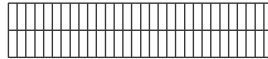


Fig. 6. The plate model with double core layers



Fig. 7. The plate model with quaternary core layers

The application of shell and solid elements in creating the plate mesh assures a proper distribution of basic stresses among the plate layers. The facings carry the normal stress, but the soft core is subjected to shear stress. The proposal of such a selection of elements in sandwich plate mesh has been presented in work [7].

Making use of the surface contact interaction, the inner surfaces of facing mesh elements have been tied with the outer surfaces of the core mesh. The boundary conditions with the limitation of radial relative displacements in the plate slidably clamped edges are imposed on the outer and inner plate edges.

The essential calculations have been carried out without the limitation of individual plate layers deformation. The plate cases where the deformation limitation of the layers occurs through tying in each of them or only the outer layers with the condition of equal deflections could be the additional computational plate models. The calculations were carried out in the ABAQUS system, version 6.3, at the Academic Computer Center CYFRONET-CRACOW (KBN/C3840/CD/034/1996) [8].

4. Analysis of calculation results

The essential analysis of calculation results of the plates considered is preceded by observing the forms of plate critical deformations under the minimal values of critical loads, which are particularly important in the stability problems. The calculations were carried out for the full annulus plate model (Figure 2). Besides several cases of plates with thick core, whose deformation will be presented in the further part of this paper, in all analysed examples of the plates, the minimal values of critical loads correspond to the regular, rotary axisymmetric form of loss of plate static stability. Some examples of the calculation results of the plate with facing thickness $h' = 0.001$ m, core thickness $h_2 = 0.005$ m and core material expressed by Kirchhoff's modulus $G_2 = 5$ MPa are presented in Table 1.

The minimal value of a critical load $p_{cr} = 64.08$ MPa corresponds to axisymmetric form ($m = 0, n = 1/2$) of plate deformation.

This observation has enabled applying the suitable symmetry conditions and building the plate model in the form of the circumferential sector of the annular plate (Figure 3) and finally in the form of quite simple model using the ready axisymmetric elements (Figure 5).

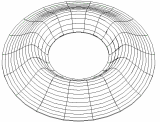
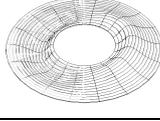
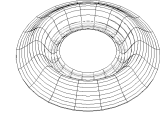
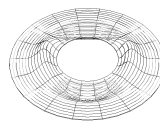
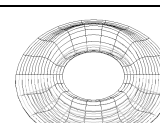
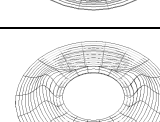
The axisymmetric form of loss of plate stability for the minimal values of critical loads has been observed for the cases of homogeneous plates with the same loading and supports, too [9, 10].

The computational results of minimal values of critical, static loads of the plates with different core thicknesses (h_2 ranging from 0.025 to 0.06 m), different values of core Kirchhoff's modulus ($G_2 = 5$ MPa and $G_2 = 15.82$ MPa) and various facing thicknesses ($h' = 0.0005$ m and $h' = 0.001$ m) are presented in Figures 8, 9.

The lines marked with the by numbers 1, 2, 3 represent the solutions for the annular sector of plate model (Figure 3). Line 1 presents the results for the plates with con-

dition of equal deflections of each plate layer. Line 2 concerns the example of the plate model for which only facings are tied in with the condition of the same deflections. Line 3 corresponds to the example of the plate model without the deformation limitation. Line 4 presents the results obtained for the plate model built of axisymmetric elements (Figure 5). Line 5 shows the results only for the plates with medium ($h_2 = 0.02$ m) and thick ($h_2 = 0.04, 0.06$ m) cores approximated by full annulus model of plate (Figure 2). The results presented on the curves marked with lines 4 and 5 correspond to the plate models without the condition of equal layers deflections. All the results presented in Figures 8 and 9 have been obtained for the plate models with the single layer of core mesh.

Table 1. The values of critical loads and the forms of loss of plate stability

Critical static stress p_{cr} [MPa]	Form of plate buckling m, n – the numbers of circumferential and radial waves, respectively
64.08	 $m = 0, n = 1/2$
74.75	 $m = 1, n = 1/2$
107.04	 $m = 0, n = 1$
109.89	 $m = 2, n = 1/2$
113.95	 $m = 1, n = 1$
141.35	 $m = 2, n = 1$

The results represented by the points visible in the diagrams, except the privileged cross points, correspond to the regular axisymmetric form of loss of plate stability.

Some examples of the deformation forms of the plates modelled as full annulus, annular sector and using the axisymmetric elements without the limitation of layers deformation are presented for the plates with thick core ($h_2 = 0.06$ m) in Figures 10, 11, 12, respectively.

The points marked with cross in the diagrams represent the plates with the critical deformation other than regular, axisymmetric form observed for each of the plate models presented. These cases occur especially for the plates with thin facings ($h' = 0.0005$ m) and stiff core. The values of minimal critical loads are decreasing. The form of buckling is characterized by a strong deformation in the region of a loaded plate edge. Some examples of the deformation forms of the plates with thin facings $h' = 0.0005$ m, thick core $h_2 = 0.06$ m and core material expressed by $G_2 = 15.82$ MPa are presented in Figures 13, 14, 15.

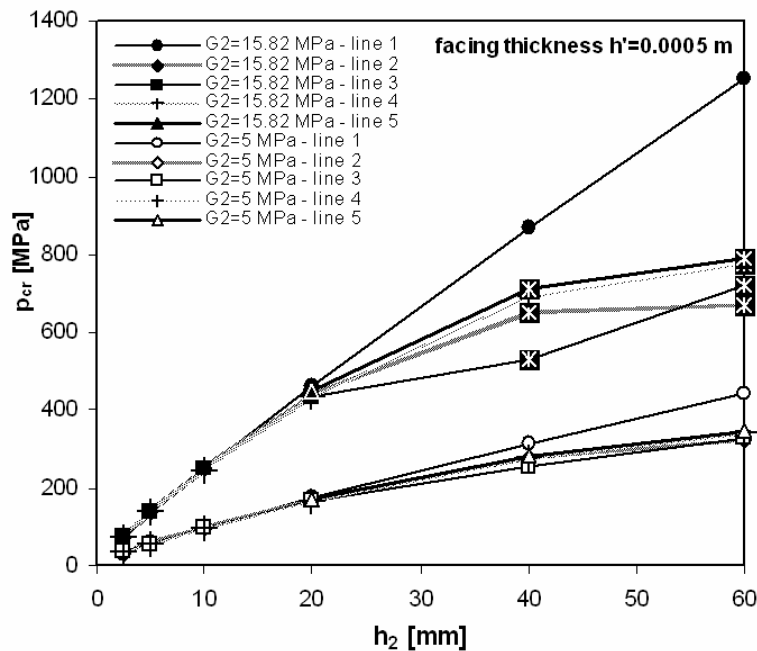


Fig. 8. Distribution of critical loads, depending on core thicknesses, for plate with facing thickness $h' = 0.0005$ m

The curves presented testify to an essential decrease in the values of the critical static loads for the plates with thicker core greater than thickness ($h_2 = 0.02$ m) and for the plates whose models are not based on the assumption of equal layers deflections. This observation is confirmed by the results obtained for the plates models with double (Figures 4, 6) and quaternary (Figure 7) layers of core mesh elements. The examples of such results are presented in Table 2.

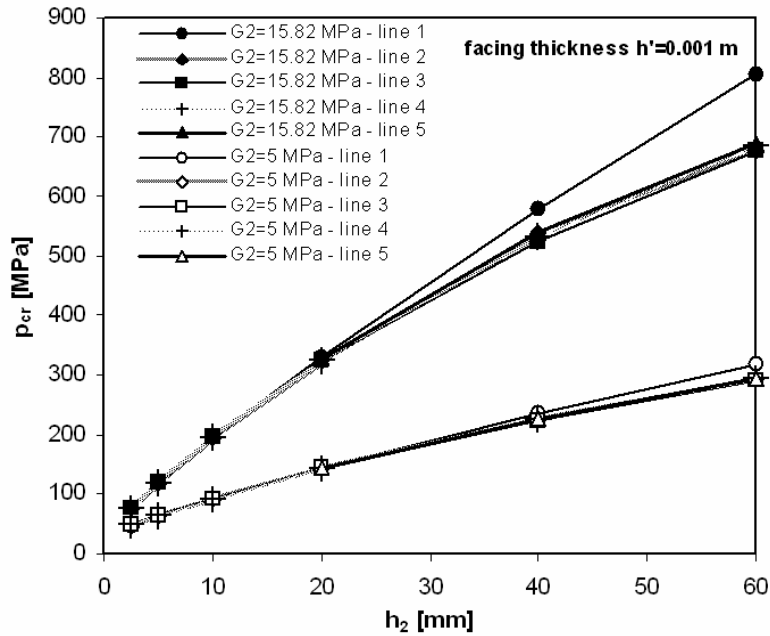


Fig. 9. Distribution of critical loads, depending on core thicknesses, for plate with facing thickness ($h' = 0.001$ m)

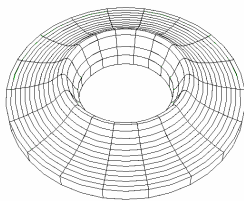


Fig. 10. Buckling of plate with $h' = 0.001$ m and $G_2 = 5$ MPa

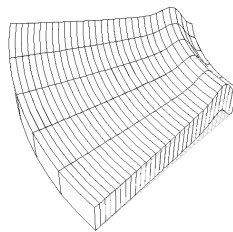


Fig. 11. Buckling of plate as annular sector, $h' = 0.001$ m, $G_2 = 15.82$ MPa



Fig. 12. Buckling of plate modelled by means of the axisymmetric elements, $h' = 0.0005$ m, $G_2 = 5$ MPa

The forms of the buckling of the plates analysed in Table 2 are presented in Figures 13, 14, 15, 16, 17 and 18. The values of the critical loads of the plate models with double or quaternary layers of core elements are lower than the values of the critical loads of plates with single core layer. Some differences in the values of the critical loads and forms of plate deformations in some way characterize the plate models and show that the structure of computational plate model in such an analysis is important.

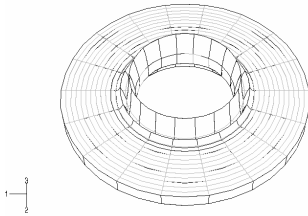


Fig. 13. Buckling of plate modelled as full annulus

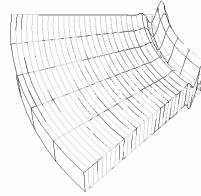


Fig. 14. Buckling of plate modelled as annular sector

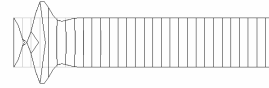


Fig. 15. Buckling of plate modelled by means of the axisymmetric elements

Table 2. The results for different models of plates with $h' = 0.0005$ m, $h_2 = 0.06$ m, $G_2 = 15.82$ MPa without the deflection limitation of layers

Models of plates	p_{cr} [MPa] (number of Figure with the buckling form)		
	Single core layer	Double core layers	Quaternary core layers
Annular sector of plate model	718.51 (Fig. 14)	511.49 (Fig. 16)	—
Model built of axisymmetric elements	774.10 (Fig. 15)	684.19 (Fig. 17)	649.49 (Fig. 18)
Full annulus plate model	791.37 (Fig. 13)	—	—

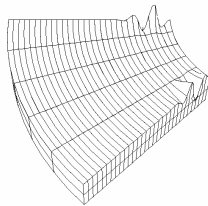


Fig. 16. Buckling of plate modelled as annular sector with double core layers

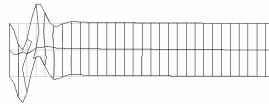


Fig. 17. Buckling of plate modeled with axisymmetric elements with double core layers

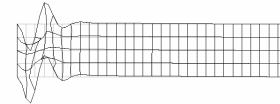


Fig. 18. Buckling of plate modelled with axisymmetric elements with quaternary layers

Critical loads for the plates with the facing thickness $h' = 0.001$ m are given in Table 3. The forms of buckling are regular, axisymmetric except the plate modelled as an annular sector with double layers of the core mesh elements. A decrease in the values of critical loads for the plate models with double or quaternary core mesh layers is observed as well. The form of the buckling of the plate modelled as annular sector with double layers for the minimal value of critical load $p_{cr} = 586.19$ MPa is presented in Figure 19.

The flexibility of the plate model of such a structure is confirmed by the results presented in Table 4 for the plate represented by the following parameters: $h' = 0.001$ m, $h_2 = 0.06$ m and $G_2 = 5$ MPa. All the plate models under examination lose their stabil-

ity in the form of regular, axisymmetric buckling. The lowest value of a critical load is measured exactly for the annular sector of the plate model with double core layers.

Table 3. Critical loads for different models of plates with $h' = 0.001$ m, $h_2 = 0.06$ m and $G_2 = 15.82$ MPa without the deflection limitation of layers

Models of plates	p_{cr} [MPa] (number of Figure with the buckling form)		
	Single core layer	Double core layers	Quaternary core layers
Annular sector of plate model	676.11	586.19 (Fig.19)	—
Model built of axisymmetric elements	686.66	659.77	655.17
Full annulus plate model	689.10	—	—

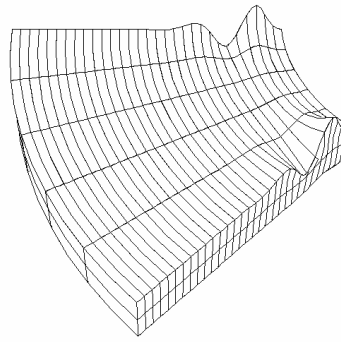


Fig. 19. The form of the buckling of the plate modelled as annular sector with double core layers

Table 4. Critical loads for different models of the plates with $h' = 0.001$ m, $h_2 = 0.06$ m and $G_2 = 5$ MPa without the deflections limitation of layers

Models of plates	p_{cr} [MPa]		
	Single core layer	Double core layers	Quaternary core layers
Annular sector of plate model	291.53	279.29	—
Model built of axisymmetric elements	292.68	288.45	287.84
Full annulus plate model	293.90	—	—

The deformation forms of cross sections of plate models built of axisymmetric elements with quaternary layers of core elements without layers limitation on their equal deflections (Figures 20, 21) show some differences in thin core $h_2 = 0.005$ m and thick core $h_2 = 0.06$ m.

The shape of cross lines of deformation could indicate the possibility of using a classical sandwich theory with the broken line hypothesis for the description of a linear deformation of thin core and the necessity to use the nonlinear formulae in the solution to the plates with a suitably thick core. This has been underlined, e.g., in the work [6].

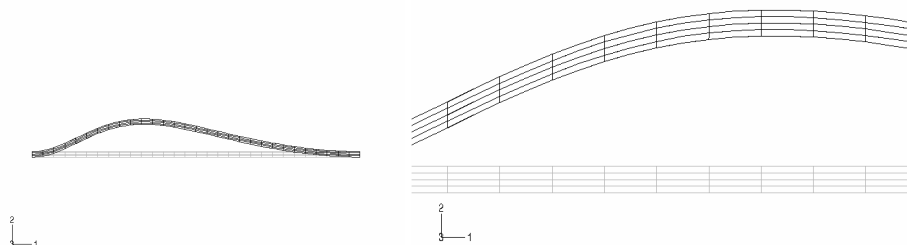


Fig. 20. The buckling and the magnified area of plate with core thickness $h_2 = 0.005$ m

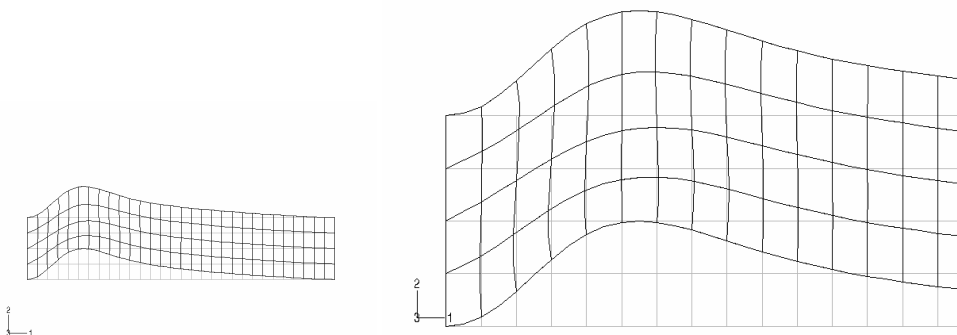


Fig. 21. The buckling and the magnified area of plate with core thickness $h_2 = 0.06$ m

The application of several computational plate models enables use to evaluate the correctness of the numerical calculations performed. The results presented in Figures 8, 9 and in Tables 2, 3, 4 confirm the compatibility of the values of critical loads also for the plate models with the condition of equal deflections of layers at the core thicknesses smaller than $h_2 = 0.02$ m.

An additional evaluation of the correctness of the calculations carried out could be the consistency of the results presented by line 1 in Figures 8, 9 for the annular sector of plate model with the condition of equal deflections of layers with the results obtained using the method presented in works [1, 2] in order to solve the problem analyzed. This method is based on the assumption of a classical sandwich theory with the broken line hypothesis and the condition of equal deflections of plate layers. The solution was obtained using the approximation finite difference method (FDM). The results for the plates with the facing thicknesses $h' = 0.0005$ m and 0.001 m are presented in Figure 22 and in Table 5, for the plate with the core thickness $h_2 = 0.06$ m, with the additional results obtained for plate model built of axisymmetric elements with the deformation limitation of layers.

The consistency of the results testifies to the correctness of the computational methods, but the high values of critical loads, particularly for plate with thin facing $h' = 0.0005$ m and stiff core with $G_2 = 15.82$ MPa, prove that the values of results

could be too high and on this account the use of the solution method presented in [1, 2] should be limited to plates with thin or medium core.

Table 5. The values of critical loads for the annular sector model and the model built of axisymmetric elements for the plates with deflection limitation and for the plate models constructed using finite difference method (FDM)

Models of plates	p_{cr} [MPa]			
	$G_2 = 5$ MPa		$G_2 = 15.82$ MPa	
	$h' = 0.0005$ m	$h' = 0.001$ m	$h' = 0.0005$ m	$h' = 0.001$ m
Annular sector of plate model	445.26	319.62	1252.27	804.84
Model built of axisymmetric elements	440.20	317.34	1238.81	796.31
Plate model constructed using FDM	406.98	312.53	1191.70	749.53

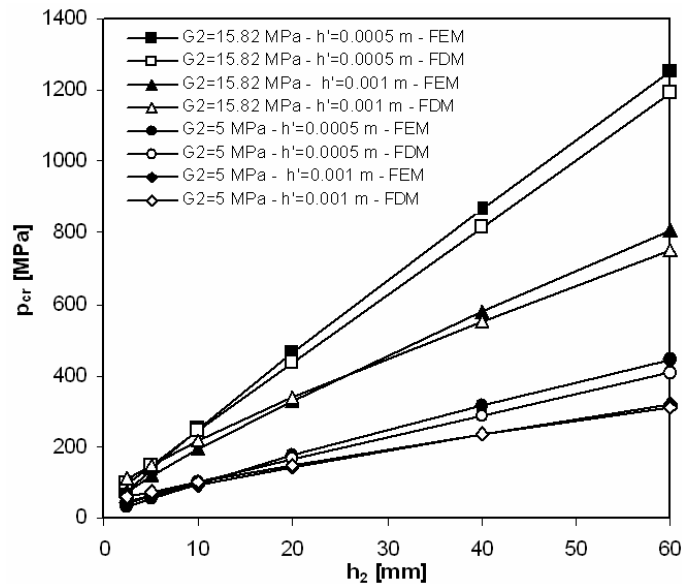


Fig. 22. Distribution of the critical loads with deflection limitation depending on the core thicknesses for plate model constructed using the FEM and FDM

5. Conclusions

The calculations of critical, static loads of three-layered, annular plates with foam core of various thickness allow us to draw the following conclusions, which are essential for the plate stability problems:

- The use of the deflection limitation of plate layers through bounding them up with the condition of equal deflections is possible only for plates with thin or medium core thickness. The values of critical loads for plates with thick core, and particularly with thin facings and stiff core, are too high. Therefore other than regular axisymmetric form of buckling can occur.

- The deformation of the thick core of sandwich plate can be nonlinear, therefore the hypothesis of broken line used for the description of cross-section deformation can induce essential errors in the problem solution.
- The structure of plate model built of finite elements, particularly of plates with stiff core and thin facings, is important. The differences in the values of critical loads are essential. The lowest values have been measured for the plate models with the core composed of several layers of mesh elements. Therefore this structure of plate model should be taken into consideration and can be an important complement of a computational analysis of plate models with the single layer of the core elements.
- Excluding the plates being analysed in detail, the first form of buckling observed for plates with clamped edges and loaded on the inner edges of the facings with compressive stress is regular and axisymmetric.

References

- [1] Pawlus D.: *Calculations of Three-Layered Annular Plates Under Lateral Loads*, *Studia Geotechnica et Mechanica*, 2003, Vol. XXV, No. 3–4.
- [2] Pawlus D.: *Obliczenia statycznych obciążeń krytycznych trójwarstwowych, osiowosymetrycznych płyt pierścieniowych*, *Czasopismo Techniczne*, 2002, z. 6-M, s. 71–86, Wydawnictwo Politechniki Krakowskiej.
- [3] Volmir C.: *Stability of Deformed System* (in Russian), Science, Moscow, 1967.
- [4] Pawlus D.: *Obliczenia metodą elementów skończonych krytycznych obciążeń statycznych trójwarstwowych płyt pierścieniowych*, *Czasopismo Techniczne*, 2003, z. 6-M, s. 137–150, Wydawnictwo Politechniki Krakowskiej.
- [5] Majewski S., Maćkowski R.: *Pełzanie spienionych tworzyw sztucznych stosowanych jako rdzeń płyt warstwowych*, *Inżynieria i Budownictwo*, 1975, 3, 127–131.
- [6] Romanów F.: *Wytrzymałość konstrukcji warstwowych*, WSI, Zielona Góra, 1995.
- [7] Kluesener M.F., Drake M.L.: *Mathematical Modeling. Damped Structure Design Using Finite Element Analysis*, *Shock and Vibration Bulletin*, 1982, Vol. 52, pp.1–12.
- [8] Hibbitt, Karlsson & Sorensen, Inc, *ABAQUS/Standard. User's Manual*, version 6.1, 2000.
- [9] Wojciech S.: *Stateczność dynamiczna ortotropowej płyty pierścieniowej obciążonej w swojej płaszczyźnie ciśnieniem zmiennym w czasie*, PhD Thesis, Politechnika Łódzka, 1978.
- [9] Trombski M., Wojciech S.: *Płyta pierścieniowa o ortotropii cylindrycznej obciążona w swej płaszczyźnie ciśnieniem zmiennym w czasie*, *The Archives of Mechanical Engineering*, 1981, XXVIII, 2.

Obliczenia krytycznych obciążeń statycznych trójwarstwowych płyt pierścieniowych metodą elementów skończonych

Przedstawiono wyniki obliczeń krytycznych obciążeń statycznych trójwarstwowych płyt pierścieniowych z miękkim, piankowym rdzeniem. Przypadkiem poddanym szczegółowej analizie jest płyta o symetrycznej budowie struktury poprzecznej, dwustronnie przesuwnie

utwierdzona, obciążona równomiernym ciśnieniem ściskającym działającym na wewnętrzny brzeg jej okładzin. Obliczenia prowadzono dla kilku rodzajów modeli obliczeniowych. W deformacji poprzecznej ich warstw wykorzystano lub nie założenie o jednakowych ugięciach warstw płyty. Obliczenia metodą elementów skończonych prowadzono, wykorzystując system ABAQUS. Analizowane są obliczone wartości krytycznych obciążeń statycznych i odpowiadające im postacie wyboczenia otrzymane dla płyt o różnych grubościach zarówno okładzin, jak i rdzenia wykonanego pianki poliuretanowej dwóch rodzajów. Wśród kilku – istotnych w zagadnieniach stateczności statycznej płyt – spostrzeżeń przedstawionych w pracy ważną wydaje się obserwacja wyników krytycznych obciążeń statycznych o wartościach znacznie zawyżonych. Może ona wskazywać na ograniczoną możliwość stosowania założenia jednakowego ugięcia warstw płyty w opisie deformacji poprzecznej płyt z rdzeniem grubym.



Testing of the inverse software for identification of rheological models of materials subjected to plastic deformation

D. SZELIGA, M. PIETRZYK

Akademia Górniczo-Hutnicza, Mickiewicza 30, 30-059 Kraków, Poland

The general objective of the present work was to perform numerical tests for the inverse analysis of various plastometric tests. Uniaxial compression, plane strain compression and ring compression were investigated for different materials. The experimental results, in the form of load vs. displacement measurements carried out in two laboratories for various sample dimensions, were used as input for inverse calculations. As a result, a large number of data was obtained and the comparison of flow stress values determined in various tests and in various laboratories was possible. The capabilities of the inverse analysis as well as the influence of the method of testing on the material properties were examined. It is shown, in general, that when the inverse analysis is applied to the interpretation of the plastometric tests, the properties of the material are insensitive to the method of testing and to the sample dimensions.

Keywords: *flow stress, plastometric tests, inverse analysis*

1. Introduction

The accuracy of numerical simulations of metal-forming processes depends, to a large extent, on the correctness of the description of material rheological properties as well as on mechanical and thermal boundary conditions. The former aspect is the topic of this paper. Evaluation of the rheological parameters in various conditions of deformation by performing plastometric tests of compression or tension or torsion [1] is one of the challenges in simulations of thermomechanical processes. The inhomogeneities and localization of strains, the effect of friction and heat generated due to deformation and due to friction are the disturbances in the tests. Thus, the goal of many researchers was to develop the method that eliminates the influence of the disturbances in the tests and allows estimation of material parameters independent of those phenomena. The problem of parameters evaluation is defined as an inverse problem. Several inverse models were proposed in the literature [2–7]. Inverse algorithm developed by the authors is described in [8]. The problem of evaluating the accuracy of the inverse analysis still remains unresolved. Evaluation of the performance of the inverse software on the basis of numerical tests performed for various experiments and sample dimensions is the objective of the present work. This is an extension of the research described in [1].

2. Experiments

Uniaxial compression (UC), ring compression (RC) and plane strain compression (PSC) tests were performed in two laboratories for various materials. Dimensions of the samples are given in Table 1, where: R – the outer diameter, r – the inner diameter, h – the height, l – the length (perpendicular to the platen), b – the width (along the platen). The width of the platen in the PSC tests was 16 mm for samples PSC_0, 10 mm for samples PSC_L and 5 mm for smaller samples PSC_S. The layout of the PSC test is shown in Figure 1. The materials tested were carbon-manganese steel, two alloyed steels, i.e., NV2-4 (LA_1) and P460NV1 (LA_2), niobium microalloyed steel (Nb_MA), aluminum alloy and brass. Chemical composition of steels is given in Table 2. The tests were performed with a Gleeble 3800 simulator in IMZ Gliwice, Poland, and with an INSTRON servohydraulic machine in NPL, Teddington, UK [9].

Table 1. Dimensions of the compression test samples, mm

Sample/ material	R	h	r	Sample/ material	h	l	b
RC/ C-Mn	7.0	4.7	3.6	PSC_0/ LA_1, LA_2	20	25	35
UC/ C-Mn, Nb_MA	5	12	–	PSC_L/ C-Mn	15	20	35
UC/ LA_2, Al alloy, brass	5	15	–	PSC_S/ C-Mn	10	15	20

Table 2. Chemical composition of the steels tested, wt%

Steel	C	Mn	Si	Ni	Cu	Cr	Mo	V	Nb	P	S
C-Mn	0.16	0.43	0.23	–	0.03	0.01	–	–	0.001	0.006	0.015
LA_1	0.075	1.375	0.25	0.3	0.15	0.15	0.08	0.01	0.025	0.015	0.05
LA_2	0.15	1.55	0.52	0.45	0.2	0.1	0.1	0.1	0.035	0.02	0.005
MA_Nb	0.17	0.43	0.35	–	0.04	0.03	–	–	0.03	0.008	0.003

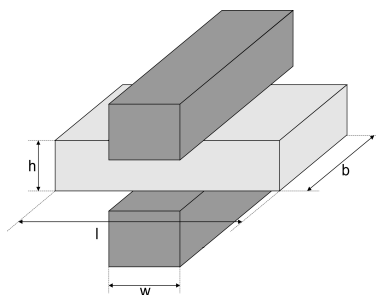


Fig. 1. Layout of the PSC test

Loads and die displacements were measured in the tests. The data recorded were filtered and used as an input for the inverse calculations. Temperature was measured at the centre of the axisymmetrical sample and at two locations (centre and the location close to the contact with the die) in the plane strain compression. Temperature was reasonably uniform after heating axisymmetrical samples. Contrary, some difference between surface and the centre was observed in the plane strain compression tests, see

Figure 2. The influence of deformation heating is seen in this figure. Beyond this, the effect of control system, which turns on heating during the slow test, is also observed. Thus, the measured temperatures were introduced as initial condition into the inverse calculations.

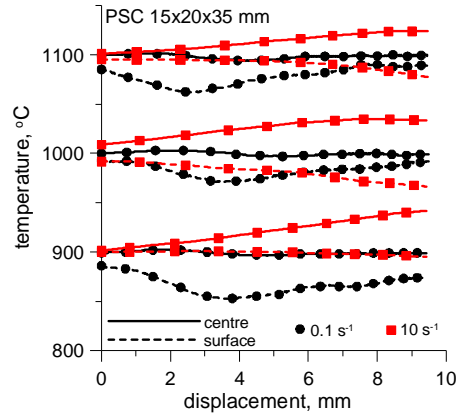


Fig. 2. Time-temperature profiles at two locations during plane strain compression; nominal temperatures of 900, 1000, 1100 °C, strain rates of 0.1 and 10 s⁻¹

3. Inverse method

Full details of the inverse algorithm, which is used, are given in [8]. This algorithm is the basis of the user-friendly inverse software developed by the authors. Briefly, the rheological and friction parameters are determined by searching for the minimum of a goal function:

$$\phi = \sqrt{\frac{1}{Nt} \sum_{i=1}^{Nt} \left[\frac{1}{Nr} \sum_{j=1}^{Nr} \left(\frac{R_{ij}^m - R_{ij}^c}{R_{ij}^m} \right)^2 + \frac{1}{Ns} \sum_{j=1}^{Ns} \left(\frac{F_{ij}^m - F_{ij}^c}{F_{ij}^m} \right)^2 \right]}, \quad (1)$$

where: Nt – the number of tests, Nr – the number of radius measurements along the height of the sample, Ns – the number of load measurement sampling points in one test, F_{ij}^m, F_{ij}^c – the measured and calculated loads, respectively, R_{ij}^m, R_{ij}^c – the measured and calculated radii of the sample after the test, respectively.

The goal function (1) is used for the uniaxial and ring compression tests. Both friction coefficient and flow stress model are determined from these tests. Loads only are measured in the plane strain compression and the goal function (1) contains only the second term under the square root [8]. The calculated values of loads and the shape of the samples are obtained from the direct problem model. This model is based on the

rigid-plastic thermomechanical finite element solution proposed in [10]. A detailed description of the algorithm and the program, which are used in this work, is given in [11]. The main equations are repeated below briefly for completeness. The solution assumes that the material obeys the Huber–Mises yield criterion and the associated Levy–Mises flow rule. The velocity field is calculated by searching for a minimum of the power functional:

$$J = \int_{\Omega} (\sigma_i \dot{\epsilon}_i + \lambda \dot{\epsilon}_V) d\Omega - \int_{\Gamma} \mathbf{f}^T \mathbf{v}_s d\Gamma, \quad (2)$$

where: σ_i – the effective stress equal to the flow stress σ_p , $\dot{\epsilon}_i$ – the effective strain rate, Ω – the volume, Γ – the contact surface, $\dot{\epsilon}_V$ – the volumetric strain rate, λ – the Lagrange multiplier, $\mathbf{f} = \{\tau_x, \tau_y\}^T$ – the vector of boundary tractions, τ_x, τ_y – the components of external stress, which represents friction, $\mathbf{v}_s = \{v_x, v_y\}^T$ – the vector of velocities with the components v_x, v_y .

In the flow theory of plasticity, strain rates are related to stresses by the Levy–Mises flow rule, which for the plane strain problem is:

$$\boldsymbol{\sigma} = \begin{bmatrix} 2G & 0 & 0 \\ 0 & 2G & 0 \\ 0 & 0 & G \end{bmatrix} \dot{\boldsymbol{\epsilon}}, \quad G = \frac{\sigma_p}{\dot{\epsilon}_i}, \quad (3)$$

σ_p – the flow stress, $\boldsymbol{\sigma} = \{\sigma_x, \sigma_y, \sigma_{xy}\}^T$ – the vector of stresses, $\dot{\boldsymbol{\epsilon}} = \{\dot{\epsilon}_x, \dot{\epsilon}_y, \dot{\epsilon}_{xy}\}^T$ – the vector of strain rates, $\sigma_x, \sigma_y, \sigma_{xy}$ – the stress components, $\dot{\epsilon}_x, \dot{\epsilon}_y, \dot{\epsilon}_{xy}$ – the strain rate components.

When axisymmetrical test is simulated, circumferential strain and stress are additionally considered. The flow stress σ_p in Equation (3) is the only one material parameter in the model. This parameter is, however, dependent on a number of the process parameters such as strain, strain rate and temperature. Determination of the function describing these relations is the main objective of the inverse analysis. A number of functions describing the relation between the flow stress and the process parameters have been proposed and discussed in [11, 12]. Some of them deal with specific materials [13]. In the present work, a reasonably simple function proposed in [3] is selected:

$$\sigma_p = \sqrt{3} \left[WK_0 \varepsilon^n \exp\left(\frac{\beta}{T}\right) + (1-W)K_s \exp\left(\frac{\beta_s}{T}\right) \right] (\sqrt{3}\dot{\epsilon})^m, \quad (4)$$

where: $W = \exp(-R_0 \varepsilon)$, and $K_0, n, \beta, K_s, \beta_s, m, R_0$ are material parameters, being determined by means of the inverse analysis.

Equation (4) describes reasonably well the flow stress when the effect of softening due to dynamic recrystallization is not complicated. In some materials, however, dynamic recrystallization leads to a fast softening after the peak strain and then the steady state is reached, when constant saturation stress is maintained. This problem is exactly described in [14]. The equation, which is much more flexible in the description of materials softening, was developed at the University of Sheffield:

$$\sigma = \sigma_0 + (\sigma_{ss(e)} - \sigma_0) \left[1 - \exp\left(-\frac{\varepsilon}{\varepsilon_r}\right) \right]^{1/2} - R, \quad (5)$$

$$R = \begin{cases} 0 & \varepsilon \leq \varepsilon_c \\ (\sigma_{ss(e)} - \sigma_{ss}) \left\{ 1 - \exp\left[-\left(\frac{\varepsilon - \varepsilon_c}{\varepsilon_{xr} - \varepsilon_c}\right)^2\right] \right\} & \varepsilon > \varepsilon_c \end{cases},$$

$$\sigma_0 = \frac{1}{\alpha_0} \sinh^{-1}\left(\frac{Z}{A_0}\right)^{1/n_0},$$

$$\sigma_{ss(e)} = \frac{1}{\alpha_{sse}} \sinh^{-1}\left(\frac{Z}{A_{sse}}\right)^{1/n_{sse}},$$

$$\sigma_{ss} = \frac{1}{\alpha_{ss}} \sinh^{-1}\left(\frac{Z}{A_{ss}}\right)^{1/n_{ss}},$$

$$\varepsilon_r = 0.31[q_1 + q_2(\sigma_{ss(e)})^2],$$

$$\varepsilon_{xr} - \varepsilon_c = \frac{\varepsilon_{xs} - \varepsilon_c}{1.98},$$

$$\varepsilon_c = C_c \left(\frac{Z}{\sigma_{ss(e)}^2} \right)^{N_c},$$

$$\varepsilon_{xs} - \varepsilon_c = C_x \left(\frac{Z}{\sigma_{ss(e)}^2} \right)^{N_x}.$$

This equation is described in [15]. It allows modelling of the variety of materials in a wide range of deformation conditions. The main difficulty in applying this model lies in a large number of parameters, which have to be identified. Nevertheless, Equation (5) was used in the present work for some of the materials investigated.

Friction plays an important role in the inverse analysis of plastometric tests. The friction model suggested first by Chen and Kobayashi [16] is used in the present work:

$$\tau = m\sigma_p \operatorname{arctg} \frac{\Delta v}{a}, \quad (6)$$

where: m – the friction coefficient, Δv – the relative slip velocity, a – a constant, by few orders smaller than an average slip velocity.

The flow formulation, the basis of the mechanical model, is coupled with the finite element solution of the Fourier heat transfer equation:

$$\nabla k(T) \nabla T + Q(T) = c_p(T) \rho(T) \frac{\partial T}{\partial t}, \quad (7)$$

where: $k(T)$ – the conductivity, $Q(T)$ – the heat generation rate due to deformation work, $c_p(T)$ – the specific heat, $\rho(T)$ – the density, T – the temperature, t – the time.

The following boundary conditions are used in the solution:

$$k \frac{\partial T}{\partial \mathbf{n}} = q + \alpha(T_a - T), \quad (8)$$

where: α – the heat transfer coefficient, T_a – the surrounding temperature or tool temperature, q – the heat flux due to friction, \mathbf{n} – the unit vector normal to the surface.

Discretization of the problem is performed in a typical finite element manner and simulations of metal-forming processes can be carried out.

4. Results

The inverse analysis of the ring compression tests yielded different values of the friction coefficient in Equation (8) for different materials. The results are given in Table 3. The difference between friction coefficient in the PSC and UC tests for the low-alloy steels is due to the different tool material. PSC tests for these steels were performed with the Gleeble 3800 with lubrication and UC tests for the LA_1 steel were performed with the INSTRON machine, where no lubricant was used.

Table 3. Values of the friction coefficient obtained for various materials

Steel	LA_1, LA_2	LA_1	C-Mn	MA_Nb	Al alloy	Brass
Test	PSC	UC	all	UC	UC	UC
m	0.14	0.3	0.11	0.12	0.05–0.11	0.17

4.1. Carbon-manganese steel

All results obtained for the C-Mn steel are described in [17]. Selected graphs only, with comparison of stress–strain curves obtained from various tests, using direct interpretation and inverse analysis, are presented in this paper in Figure 3. PSC_L and PSC_S samples in Table 1 were used in the plane strain compression. It is seen that large differences between uniaxial and plane strain compression occur when direct interpretation is applied. Much better consistency is observed after inverse calculations, in particular at higher temperatures. Beyond this, the direct interpretation of the PSC tests gives the stress values exceeding those determined using inverse analysis. This is due to an influence of the rigid ends, which is neglected in the direct analysis.

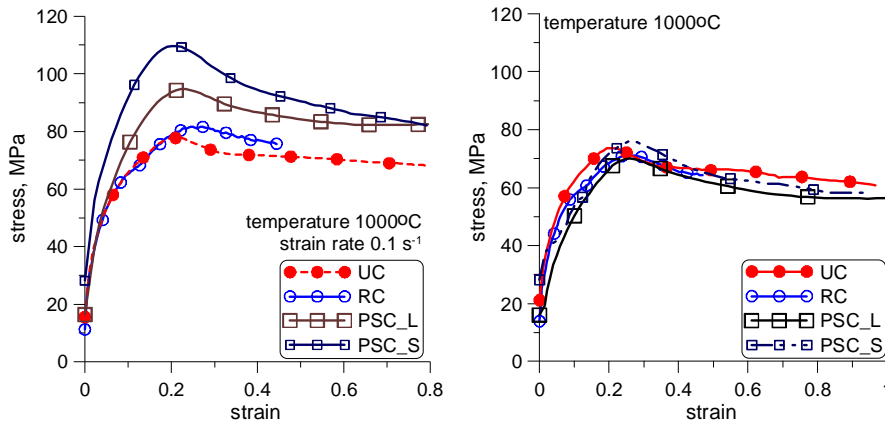


Fig. 3. Flow stress as a function of strain calculated directly from the tests as the load-to-contact area ratio (left) and determined from the inverse calculations (right)

Figure 4 shows selected examples of the inverse analysis for the temperatures of 900 °C and 1100 °C. Two conclusions can be drawn from these results. The first is that much better consistency in the results obtained from various tests is observed for lower strain rate. It might be due to the difficulties with maintaining the constant strain rate in fast tests. The second observation is that the flow stress obtained from the ring compression is always slightly lower than that obtained from the remaining tests. This is in agreement with observations in [18], where it is shown that the flow stress of material is correlated with the state of stress represented by the Lode coefficients:

$$\beta = \frac{2}{\sqrt{3 + \xi^2}}, \quad \xi = \frac{2\sigma_2 - \sigma_1 - \sigma_3}{\sigma_1 - \sigma_3}. \quad (9)$$

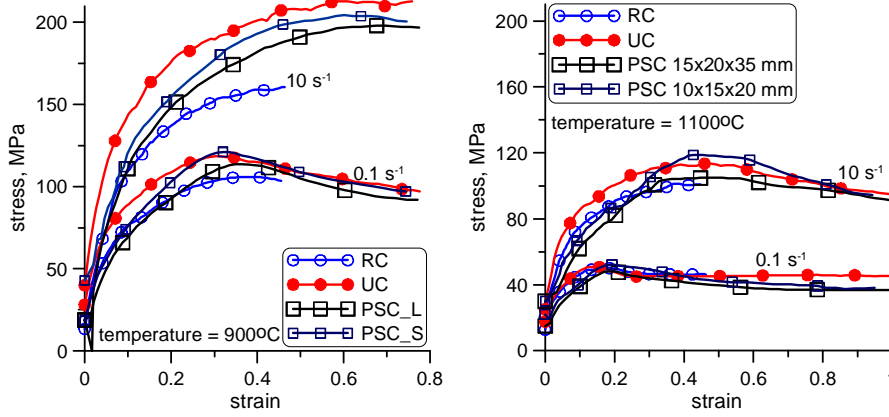


Fig. 4. Flows stress as a function of strain calculated directly from the tests as the load-to-contact area ratio (left) and determined from the inverse calculations (right)

The Lode coefficient β depends on the values of the main stresses (σ_1 , σ_2 , σ_3) and varies between $\beta = 1$ for $\sigma_2 = \sigma_1$ or $\sigma_2 = \sigma_3$ and $\beta = 2/\sqrt{3}$ for plane strain condition $\sigma_2 = 0.5(\sigma_1 + \sigma_3)$. It is shown in several publications, see for example [19, 20], that when the state of strain is close to the plane strain condition, the initiation of microshear bands in a material is easier and the resulting flow stress is lower. The state of strain in ring compression varies from $\sigma_2 = \sigma_1$ ($\beta = 1$) for very low friction to plane strain ($\beta = 2/\sqrt{3}$) for larger friction coefficients. In the case presented in Figure 4, the friction coefficient is large enough to create the state of strains close to the plane strain and the flow stress is lower than in the remaining tests. A similar decrease of the flow stress is observed in [19] for the channel test, where the plane strain condition is enforced by the walls of the channel.

4.2. Low-alloy steels

PSC_0 samples in Table 1 were used in all tests for low-alloy steels. Since both LA_1 and LA_2 steel samples were cut from the material, which was taken directly from plate rolling mill in one of the steel plants, the problems with repeatability of results were expected. Thus, the tests were repeated twice, or if necessary three times, under the same conditions. All recorded load–displacement data for the LA_1 steel are presented in Figure 5. At least two samples were tested for each case and reasonably good consistency was observed.

The results of the inverse analysis for this steel are shown in Figure 6. In Figure 7, selected examples of flow stress calculated directly as load-to-contact area ratio are compared with these determined by the inverse analysis. It is seen in this figure that direct interpretation of the results of the PSC tests yields flow stress significantly exceeding the real one. There are conventional methods allowing the PSC tests to be in-

dependent of the influence of various phenomena, see for example [15], but the results fully insensitive to these phenomena can be obtained only by the inverse analysis.

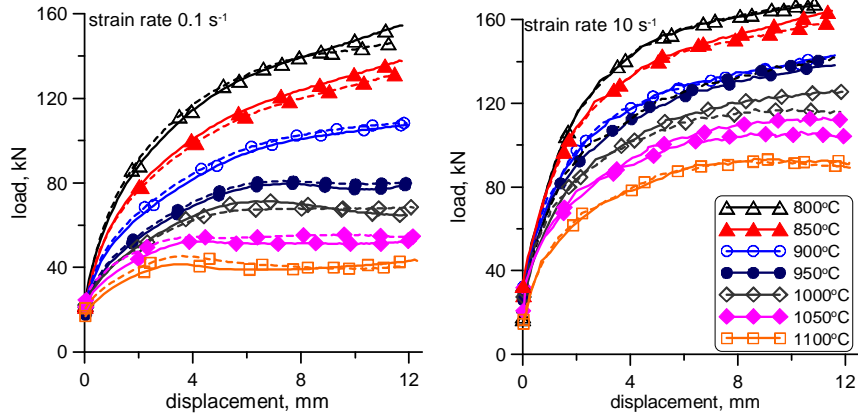


Fig. 5. Load–displacement data recorded during plane strain compression of LA_1 steel, strain rates of 0.1 s⁻¹ and 10 s⁻¹

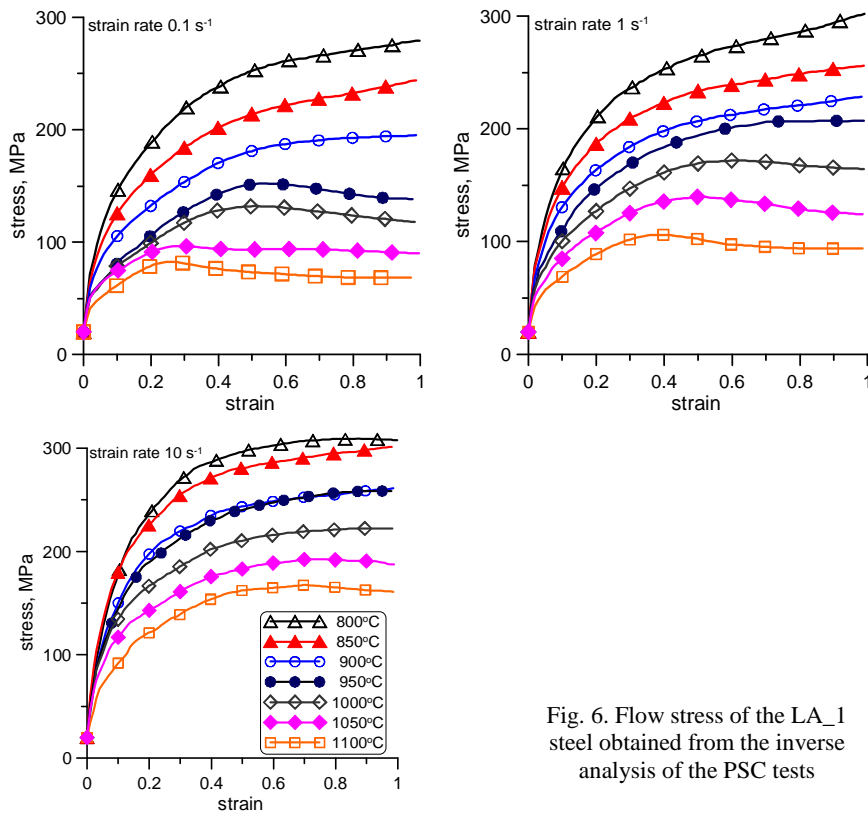


Fig. 6. Flow stress of the LA_1 steel obtained from the inverse analysis of the PSC tests

All recorded load–displacement data for the PSC tests of the LA_2 steel being presented in publication [1] are not repeated here. The results of the inverse calculations for this steel are shown in Figure 8.

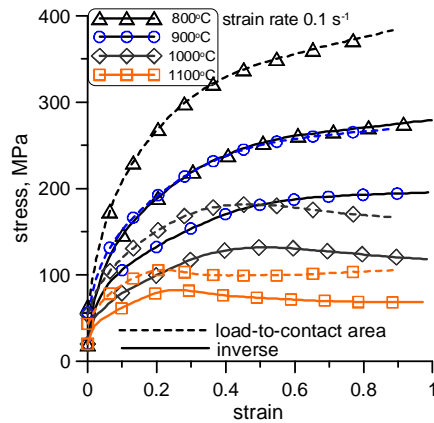


Fig. 7. Flow stress calculated directly as load-to-contact area ratio (dotted lines) and determined by the inverse analysis (solid lines) for the PSC test, steel LA_1

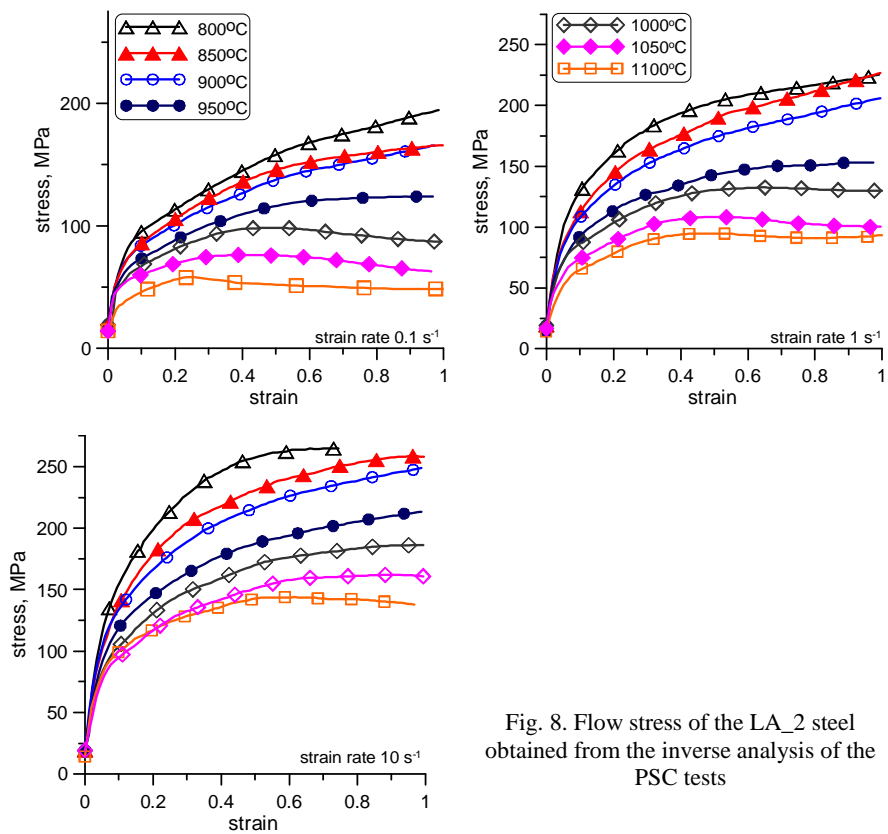


Fig. 8. Flow stress of the LA_2 steel obtained from the inverse analysis of the PSC tests

The behaviour of the low-alloy steels was rather complicated and the application of a simple function (4) to describe the flow stress did not give good results. Therefore, more complex Equation (5) was used. The coefficients in this equation obtained from the inverse analysis are given in Table 4. Validation of the inverse calculations is shown in Figure 9, where selected examples of the comparison between the loads measured and the loads calculated by the FEM model with the flow stress obtained from the inverse analysis are presented. FEM calculations were performed using flow stress function (5) with coefficients in Table 4 as the rheological model. Reasonably good agreement is observed for both steels.

Table 4. Coefficients in Equation (5) determined using the inverse analysis for the low-alloy steels (Q_{def} – is an activation energy in the Zener–Hollomon parameter Z)

Coefficient	LA_1	LA_2
A_0	5.07	61.9
n_0	6.62	6.04
α_0	0.642	0.396
A_{sse}	1.74×10^{14}	3.71×10^{14}
n_{sse}	6.62	6.04
α_{sse}	0.00934	0.00864
A_{ss}	3.38×10^{16}	4.23×10^{16}
n_{ss}	5.34	4.49
α_{ss}	0.00699	0.00404
q_1	0.954	0.739
q_2	4.0×10^{-6}	5.72×10^{-6}
C_c	6.43×10^{-7}	7.29×10^{-7}
N_c	0.557	0.555
C_x	154	200
N_x	0.239	-0.261
Q_{def}	377000	384000

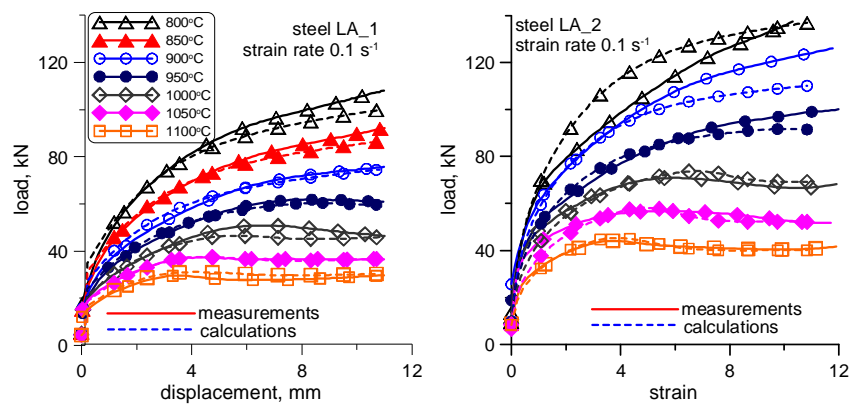


Fig. 9. PSC tests – loads measured and calculated by the FEM model with the flow stress obtained from the inverse analysis for the LA_1 steel (left) and LA_2 steel (right)

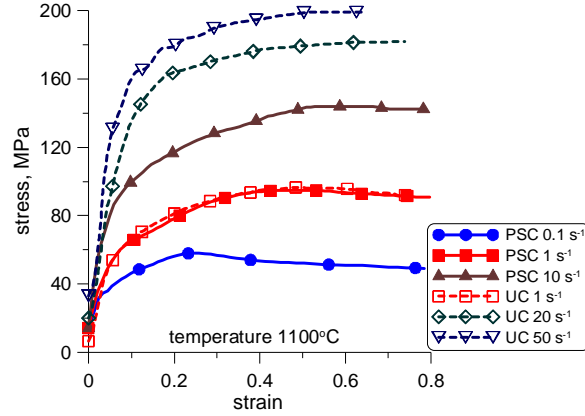


Fig. 10. Flow stress of LA_2 steel determined from PSC and UC tests at various strain rates

Figure 10 shows the comparison of the flow stress determined from the inverse analysis of the UC tests and PSC tests for the LA_2 steel. The UC tests were performed with a constant tool velocity at higher average strain rates of 1, 20 and 50 s^{-1} . PSC tests were carried out at constant strain rates of 0.1, 1 and 10 s^{-1} . No lubricant was used in the UC tests and the friction coefficient of 0.3 was determined from the inverse analysis with the goal function (1). In PSC tests, a lubricant was applied and the friction coefficient reached the value of 0.14. More information about these tests can be found in [9]. It is seen in Figure 10 that the inverse analysis accounted properly for different state of strains, friction conditions and mode of the tool velocity and yielded identical results for the common conditions of 1100 $^{\circ}\text{C}$ and 1 s^{-1} . This confirms an obvious capability of the inverse method to neutralize the influence of various disturbances in the plastometric tests.

4.3. Microalloy steel

Uniaxial compression was performed for the microalloy niobium steel. For details on this experiment, see [21]. All the results of the inverse analysis for this steel are presented in Figure 11. It is seen that the lowest temperature of 800 $^{\circ}\text{C}$ is close to the temperature of the beginning of phase transformation, which is confirmed by the results in [21]. The occurrence of ferrite is the reason for the softening observed in the tests at 0.1 s^{-1} . The inverse analysis yielded the values of coefficients in Equation (4), which are given in Table 5.

Table 5. Coefficients in Equation (5) determined using the inverse analysis for microalloy niobium steel, aluminum alloy and brass

	K_0	β	m	n	K_{sat}	β_{sat}	R_0
MA_Nb	3.97	3490	0.317	0.115	0.063	7806	1.575
Al alloy	0.671	2581	0.159	0.000067	0.149	3678	1.487
Brass	0.064	5132	0.213	0.117	0.407	137	0.387

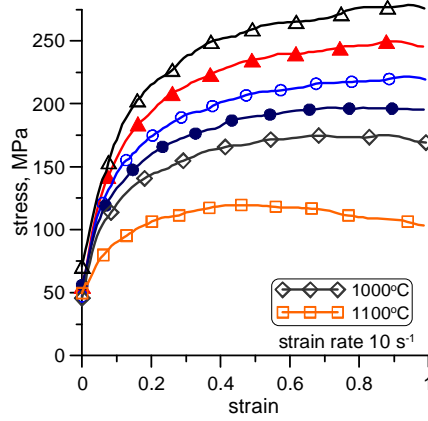


Fig. 11. Flow stress of the microalloy niobium steel calculated by the inverse analysis of the UC tests

4.4. Aluminum alloy

The composition of the alloys was not revealed by the supplier. The uniaxial compression tests were performed at four temperatures (400 °C, 450 °C, 500 °C and 550 °C) and two strain rates (0.1 s⁻¹ and 10 s⁻¹). The friction coefficient obtained by minimizing function (1) varied between 0.05 and 0.11, depending on the temperature and the strain rate. All the results of the inverse calculations for aluminum alloy are shown in Figure 12.

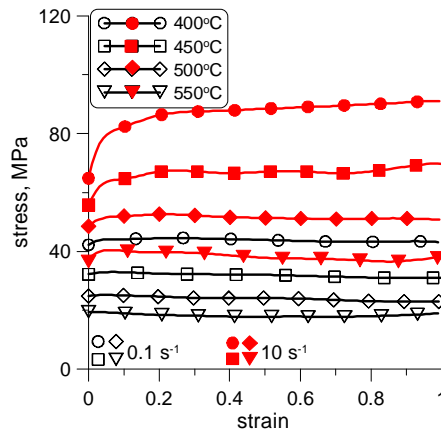


Fig. 12. Flow stress of the aluminum alloy calculated by the inverse analysis of the UC tests

Flow stress function (4) was used for the aluminum alloy with the coefficients determined by the inverse analysis given in Table 4. Validation of the flow stress model for the aluminum alloy is shown in Figure 13. The measured loads are compared with

the predictions of the FEM model with optimized Equation (4) used as constitutive model. Good agreement was obtained for the slow tests, and small discrepancies are observed in the fast tests.

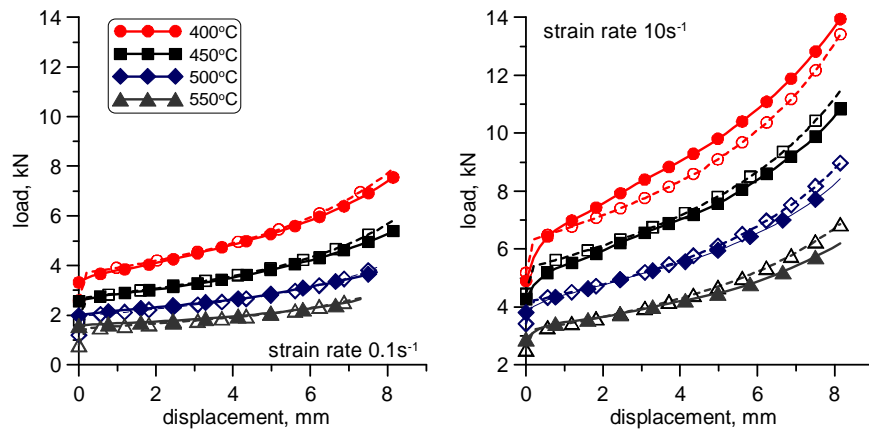


Fig. 13. Load–displacement data during uniaxial compression of aluminum alloy obtained from measurements (filled points, solid lines) and predicted by the FEM model with the flow stress determined by the inverse analysis (open points, dotted lines)

4.5. Brass

Detailed analysis of the tests for brass is given in [22]. Briefly, the UC was performed at five temperatures (500 °C, 550 °C, 600 °C, 650 °C and 700 °C) and three strain rates (0.01 s⁻¹, 0.1 s⁻¹ and 10 s⁻¹). The tests at 700 °C are not reliable because the material was very soft. The friction coefficient obtained by minimization of function (1) was 0.17. All the results of inverse calculations for brass are shown in Figure 14.

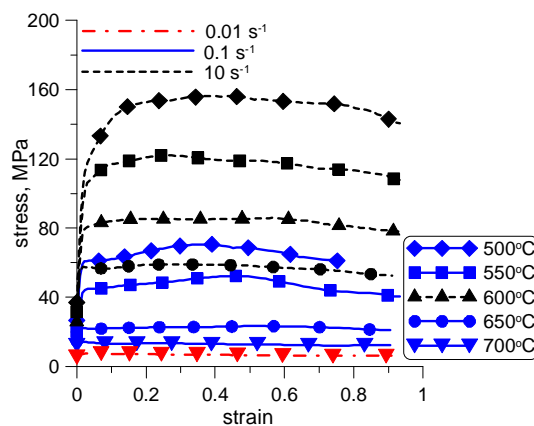


Fig. 14. Flow stress of brass calculated by the inverse analysis of the UC tests

Flow stress function (4) was used for brass and the coefficients of this function determined by the inverse analysis are given in Table 4. The results of validation of the flow stress model for brass are presented in Figure 15. The measured loads are compared with the predictions of the FEM model with optimized Equation (4) used as rheological model. The agreement between measurements and predictions is slightly worse than that for the aluminum alloy.

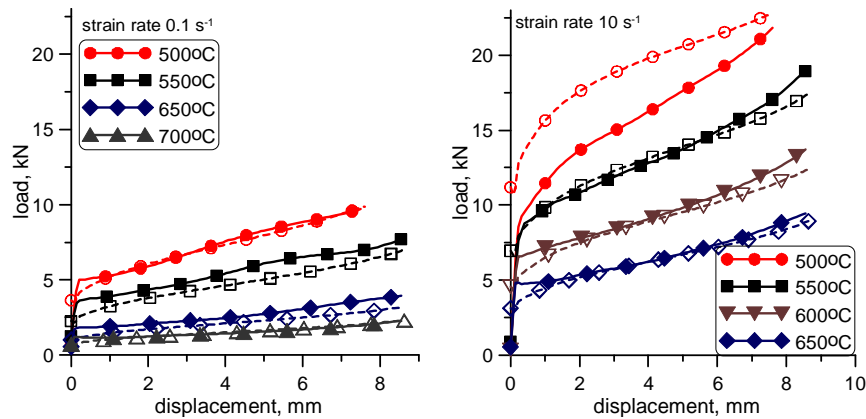


Fig. 15. Load–displacement data during uniaxial compression of brass obtained from measurements (filled points, solid lines) and predicted by the FEM model with the flow stress determined by the inverse analysis (open points, dotted lines)

5. Discussion

The inverse method was tested for a large number of experimental data. Very good capability of this technique to interpret correctly the results of plastometric tests has been confirmed. The inverse analysis allows us to investigate materials behaviour on the basis of various plastometric tests. It is shown in [9] that when the inverse analysis is applied it is possible to investigate an influence of the preheating before the test on the results, even if the tests are performed with different machines. The possibility of evaluating accurately the relationship between the peak stress and the test conditions is the next advantage of the inverse technique. Direct interpretation of the PSC tests did not yield any consistent relationship between peak stress, temperature and strain rate. After the inverse analysis was applied, quite consistent results were obtained for the low-alloy steels, which is shown in Figure 16.

The inverse analysis allows us also to investigate, with a reasonable certainty, the correlation between the flow stress and the state of stress in the material. When this analysis is applied, the convincing tendency that metallic materials show lower flow stress when the plane strain conditions are enforced could be observed. See the results for the ring compression [18] and channel die tests [19].

It is shown in the paper that application of the inverse analysis allows us to determine the flow stress, which is not sensitive to the disturbances occurring in the tests. The application of the direct method of interpreting the PSC tests, in which flow stress is calculated as load-to-contact surface ratio, gives the results which are far from the real flow stress of the material. When the flow stress obtained from the direct method is implemented in the FEM code, it gives the loads which vary noticeably from the measured ones. The flow stress obtained from the inverse analysis implemented in the FEM code gives loads, which are in a very good agreement with measurements.

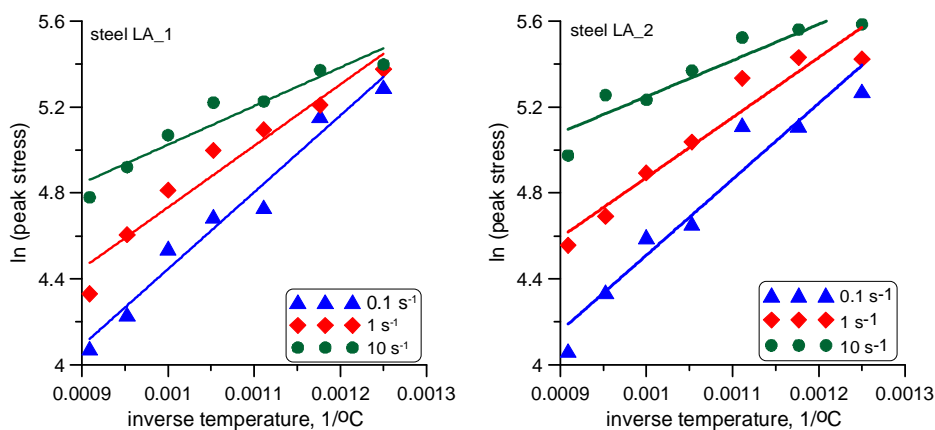


Fig. 16. Peak stress for the low-alloy steels determined on the basis of flow stress calculated using the inverse analysis

The problem mentioned is less important in the uniaxial compression, where the strains are more homogeneous, but it still exists. The application of the inverse analysis improves slightly the accuracy of the interpretation of the uniaxial tests. A general conclusion can be drawn that when the inverse analysis is applied the flow stress obtained is the property of materials, which is insensitive to the type of the test, sample dimensions, etc. As a result, an accurate analysis of the influence of parameters, which really affect the flow stress (such as state of stress, preheating, etc), became possible.

Acknowledgements

Financial assistance of KBN, project no. 4 T08B 009 24, is acknowledged. All the tests for low-alloy steels, aluminum alloy and brass were performed within the 5FP project TESTIFY.

References

- [1] Pietrzyk M., Szeliga D., Madej L.: *Validation of the inverse software for plastometric tests*, Proc. FORMING'2005, Lednice, 2005, 221–226.

-
- [2] Gelin J.C., Ghouati, O.: *The inverse method for determining viscoplastic properties of aluminium alloys*, J. Mat. Proc. Techn., 1994, Vol. 34, 435–440.
- [3] Gavrus A., Massoni E., Chenot J.L.: *An inverse analysis using a finite element model for identification of rheological parameters*, J. Mat. Proc. Techn., 1996, Vol. 60, 447–454.
- [4] Kusiak J., Kawalla R., Pietrzyk M., Pircher H.: *Inverse analysis applied to the evaluation of material parameters in the history dependent flow stress equation in hot forming of metals*, J. Mat. Proc. Techn., 1996, 60, 455–461.
- [5] Khoddam S., Lam Y.C., Thomson P.F.: *Numerical results achieved with an inverse computational method for determining the constitutive parameters using the hot torsion test results*, Steel res., 1996, Vol. 67, 39–43.
- [6] Forestier R., Massoni E., Chastel Y.: *Estimation of constitutive parameters using an inverse method coupled to a 3D finite element software*, J. Mat. Proc. Techn., 2002, Vol. 125, 594–601.
- [7] Boyer B., Massoni E.: *Inverse analysis for identification of parameters during thermo-mechanical tests*, Proc. NUMIFORM 2001, ed. by Mori K., publ. A. Balkema, Toyohashi, 2001, 281–284.
- [8] Szeliga D., Pietrzyk M.: *Identification of rheological and tribological parameters*, Metal Forming Science and Practice, A State-of-the-Art Volume in Honour of Professor J.A. Schey's 80th Birthday, ed. by Lenard J.G., Elsevier, Amsterdam, 2002, 227–258.
- [9] Pietrzyk M., Kuziak R., Loveday M., Roebuck B.: *Effect of Preheating and Testing Method on the Flow Stress of Steels*, *Advanced Technology of Plasticity*, Proc. 8th ICTP, Verona, 2005, CD ROM.
- [10] Lee C.H., Kobayashi S.: *New solution to rigid plastic deformation problems*, ASME, J. Eng. Ind., 1973, Vol. 95, 865–873.
- [11] Lenard J.G., Pietrzyk M., Cser L.: *Mathematical and Physical Simulation of the Properties of Hot Rolled Products*, Elsevier, Amsterdam, 1999.
- [12] Grosman F.: *Application of the flow stress function in programmes for computer simulation of plastic working processes*, J. Mat. Proc. Techn., 1997, Vol. 64, 169–180.
- [13] Gronostajski Z.: *Development of constitutive equations of copper-silicon alloys*, J. Mat. Proc. Techn., 1996, Vol. 60, 621–627.
- [14] Szeliga D., Węglarczyk S., Pietrzyk M.: *Estimation of simulation errors due to inaccurate evaluation of material properties in metal forming*, J. Machine Eng., 2006, Vol. 6, 64–72.
- [15] Kowalski B., Sellars C.M., Pietrzyk M.: *Development of a computer code for the interpretation of results of hot plane strain compression tests*, ISIJ Int., 2000, Vol. 40, 1230–1236.
- [16] Chen C.C., Kobayashi S.: *Rigid plastic finite element analysis of ring compression*, [in:] *Application of numerical methods to forming processes*, ASME, ADM, 1978, Vol. 28, 163–174.
- [17] Gawąd J., Kuziak R., Madej Ł., Szeliga D., Pietrzyk M.: *Identification of rheological parameters on the basis of various types of compression and tension tests*, Steel Res. Int., 2005, Vol. 76, 131–137.
- [18] Madej L., Pietrzyk M., Pidvysotsky V., Kuziak R.: *Analiza wrażliwości naprężenia uplastyczniającego, wyznaczonego z próby ściskania pierścieni, na współczynnik tarcia i wymiary próbki*, Informatyka w Technologii Materiałów, 2005, Vol. 5, 83–94.

- [19] Pidvysotsky V, Wajda W., Paćko M., Kuziak R., Pietrzyk M.: *Identification of the flow stress for copper in the room temperature*, Naukovi Visti, Suchasni Problemi Metalurgii, 2002, Vol. 5, 255–258.
- [20] Pecherki R. B.: *Modelling of large plastic deformations based on the mechanism of micro-shear banding. Physical foundation and theoretical description in plane strain*, Arch. Mech., 1992, Vol. 44, 563–584.
- [21] Pietrzyk M., Kuziak R.: *Development of the constitutive law for microalloyed steels deformed in the two-phase range of temperatures*, Steel GRIPS, 2004, Vol. 2, 465–470.
- [22] Gawąd J., Kusiak J., Pietrzyk M., Di Rosa J., Nicol G.: *Optimization Methods Used for Identification of Rheological Model for Brass*, Proc. ESAFORM 6 Conf. on Material Forming, ed. by Brucato V., Salerno, 2003, 359–362.

Testy numeryczne oprogramowania do analizy odwrotnej do identyfikacji parametrów reologicznych materiałów odkształcanych plastycznie

Celem niniejszej pracy było wykonanie testów numerycznych opracowanego przez autorów programu do analizy odwrotnej różnych prób plastometrycznych. Przedstawiono w skrócie model oraz algorytm programu. W części badawczej rozważono ściskanie próbek cylindrycznych, pierścieniowych i płaskich z różnych materiałów w różnych warunkach. Wyniki doświadczeń w formie zależności siły ściskania od przemieszczenia stempla, uzyskane w różnych laboratoriach dla różnych wymiarów próbek, zostały użyte jako dane wejściowe dla analizy odwrotnej. W konsekwencji dysponowano dużą ilością danych doświadczalnych i można było porównać wyniki uzyskane w różnych laboratoriach. Na tej podstawie wyciągnięto wnioski odnośnie do możliwości analizy *inverse* w zakresie identyfikacji modeli reologicznych materiału oraz odnośnie do wpływu rodzaju próby plastometrycznej na uzyskane wartości naprężenia uplastyczniającego. Wykazano, że kiedy wyniki prób plastometrycznych interpretuje się metodą analizy odwrotnej, wtedy wyznaczone własności materiału są niewrażliwe na rodzaj próby i na wymiary próbki.



Polyurethane coating for protecting concrete floors using the system with fillers produced by recycling

J. RYSZKOWSKA, J. RĘBIŚ, M. LANGNER

Warsaw University of Technology, Faculty of Materials Science and Engineering, Woloska 141, 02-507 Warsaw, Poland, www.materials.pl, jrysz@meil.pw.edu.pl

The top layer of the systems covering a concrete surface is made of polyurethane. The polyurethane layer should be characterized by high tensile strength and abrasive wear resistance, because this material is used in workshops, corridors, and warehouses.

Up till now the systems have been a mixture of polyurethane and different fillers. The recycle from polyurethane waste added to the systems can modify their properties.

Our purpose was to produce and to test the composites supplemented with recyclates of different hardness. The influence of the proportion of wastes on the composite properties was investigated as well.

As a result we obtained the materials of higher resistance to abrasive wear and of higher values of Young's modulus and with unchanged resistance to tensile strength, ultimate elongation and bending. Furthermore a permanent deformation of the materials tested was decreased. The recyclates of the 50°ShD hardness increase the abrasive wear resistance of composites by 50%, whilst the cost of the material is reduced.

Keywords: *coating, recycle, abrasive wear, polyurethane*

1. Introduction

It is estimated that in Poland 30 thousand tones of cast polyurethane are being produced. This material is used for producing some parts of machinery, which as a waste material are disposed of. Because polyurethane is considered to be one of the most expensive polymers that are widely used (one kilogram of PUR ranges in price from 5 to 20 euros), recycling polyurethane is being investigated [1, 2]. Of the utilization methods materials recycling seems to be the most interesting one. Recycling is not expensive, it does not meet any social objection and moreover it is the most cost-effective method in the case of expensive polymers such as polyurethanes [3, 4].

The quality of products containing duro plastic waste greatly depends on the degree of grinding. Grinding of polyurethane is difficult and its costs decide whether or not the process of utilization is economical. In Poland, research aiming at reducing the costs of grinding PUR is being performed. As a result a recycle from selected waste was obtained.

In recent years, used polyurethane machine parts are returned to their manufacturer, which makes the process of waste segregation easier, and therefore the preparation of recyclates of chosen properties is possible.

We tested the polyurethane layer consisting of two components: MC DUR 2052 and polyurethane recyclate of different hardness. The influence of the proportion and the type of waste on the density, hardness, abrasive wear resistance, tensile bending strength, compressive bending strength and Young's modulus of the composites obtained was established.

2. Experimental

2.1. Materials

The substrates for producing the top layer of floor system MC DUR 2052 (MC Bauchemie) were tested. The top layer is made of two-component polyurethane system from polyol (A) and isocyanate (B) ingredients. The top layer was modified with polyurethane recyclate. Soft recyclate: granule size between 0.4 and 1.5 mm obtained from polyurethane, 85°ShA hardness and the volume of 1.246 g/cm³; and hard recyclate: the same granule size, obtained from polyurethane of 55°ShD hardness and 1.273 g/cm³ volume.

2.2. Preparation of composite

Substrate A with recyclate was stirred at room temperature. 12–30 wt. % of recyclate was added to PUR matrix. This mixture was stirred with substrate B. The samples were conditioned for two weeks. The examples of the samples tested are shown in Figure 1.

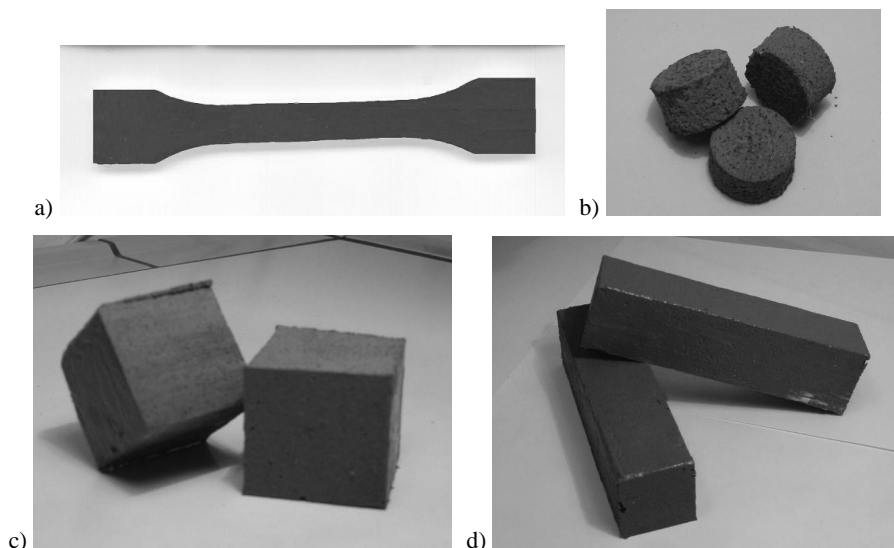


Fig. 1. Samples subjected to: a) stretching b) abrasive wear, c) compressing, d) bending

2.3. Characterization

The composite density was determined according to ISO 2781.

SEM examination. The microstructure of composites was examined by observing a cold fractured samples surface. The morphology of composites was observed under a scanning electron microscope (SEM) Hitachi 3500 N, in BSE mode, magnifications of 50× and 500×.

Mechanical properties. Tensile tests were performed using a tensile tester Instron 1115. The samples were elongated at the rate of 500 mm/min according to ISO 527. Their hardness was measured using the indentation hardness tester according to ASTM D2240-75, the abrasive wear according to ISO 4649, the compressive strength (PN-EN 197) and bending strength (PN-EN/ ISO 10545) according to respective standards. The last tests were performed in the Faculty of Civil Engineering at Warsaw University.

3. Results and discussion

Selected SEM micrographs of unmodified composite are shown in Figure 2. Figures 3 and 4 present the composite modified in such a way that it contains 30% of soft recycle and 30% of hard recycle. In Figure 2 spherical elements, i.e. the fillers used by the manufacturer, of various sizes are visible. In Figures 3 and 4, the elements of irregular shape, i.e., the recycle grains, are next to spherical fillers. In Figures 3b and 4b (500× magnification), a boundary between the filler and the matrix is presented. The air bubbles are not visible in composites being presented in Figures 3b and 4b.

During testing the sample resistance to bending the samples were not damaged. In the Table, the test results for the MC Dur 2052 system filled with soft recycle are presented. The addition of soft recycles of PUR did not significantly influence the following properties of the composite: tensile strength, compressive strength and bending strength, Young's modulus and elasticity. The hardness increased and abrasive wear increased by about 40%. In Figures 5–12, the influence of soft (1) and hard (2) recycles on the system's properties is presented.

Table. Physical and mechanical properties of composites with soft recycle

Soft recycle content (wt %)	Density ρ (g/cm ³)	Hardness H (°ShA)	Abrasive wear ΔV (cm ³)	Tensile strength R_m (MPa)	Young's modulus E (MPa)	Compressive strength σ_s (MPa)
0	1.41±0.01	80.5±0.7	1.23±0.04	2.13±0.15	18.1±0.6	10.4±0.6
12	1.37±0.01	81.8±0.9	1.11±0.07	2.62±0.35	17.5±0.7	10.2±0.5
18	1.34±0.01	82.2±0.7	1.01±0.04	2.55±0.15	17.2±0.6	10.5±0.6
24	1.29±0.02	82.8±0.8	0.97±0.06	2.48±0.18	16.8±0.9	10.7±0.9
30	1.27±0.01	84.4±0.7	0.74±0.04	2.48±0.15	17.2±0.6	7.0±0.6

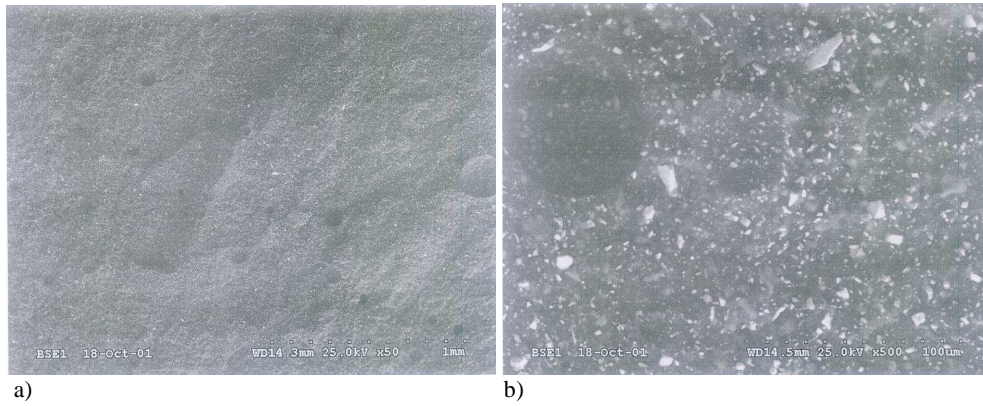


Fig. 2. SEM images of unmodified composite, magnification 50× (a), 500× (b)

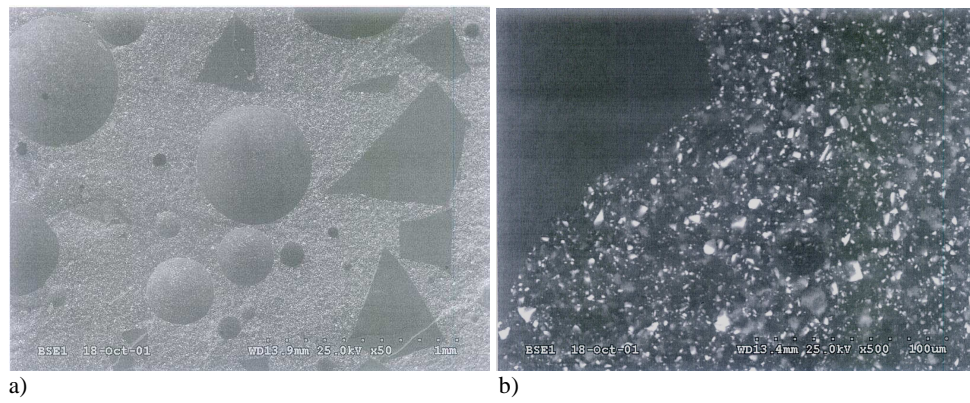


Fig. 3. SEM images of composite with 30 wt % of soft recyclate, magnification 50× (a), 500× (b)

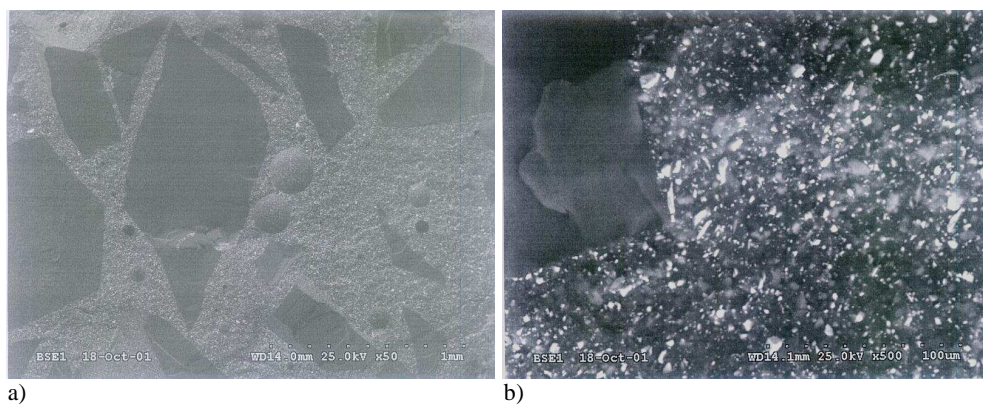


Fig. 4. SEM images of composite with 30wt % of hard recyclate, magnification 50× (a), 500× (b)

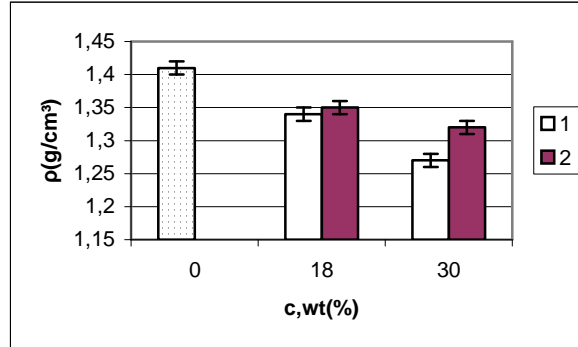


Fig. 5. Dependence of density ρ on soft (1) and hard (2) recyclate content c

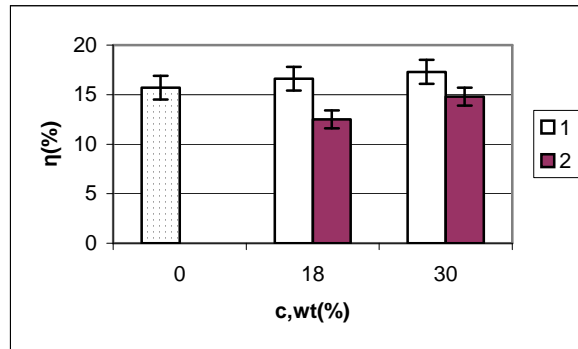


Fig. 6. Dependence of elasticity η on soft (1) and hard (2) recyclate content c

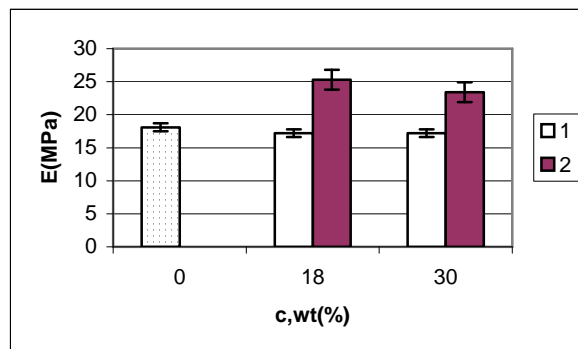


Fig. 7. Dependence of Young's modulus E on soft (1) and hard (2) recyclate content c

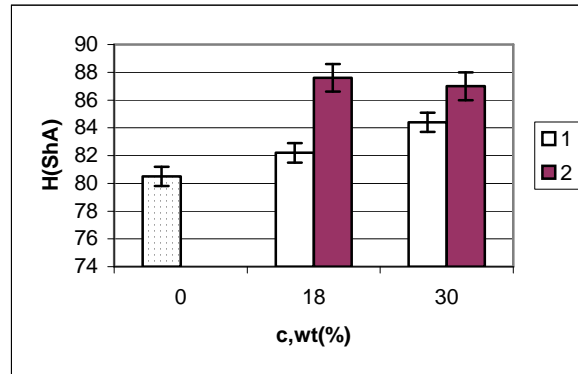


Fig. 8. Dependence of hardness H on soft (1) and hard (2) recyclate content c

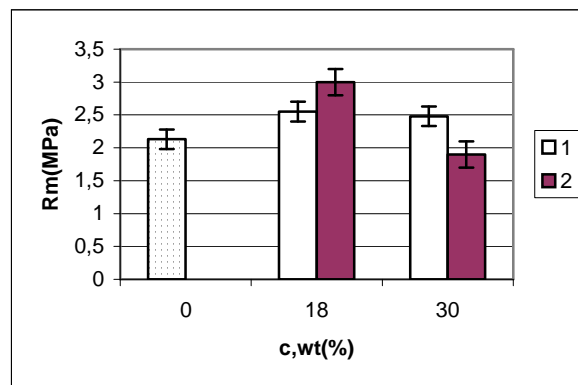


Fig. 9. Dependence of tensile strength R_m on soft (1) and hard (2) recyclate content c

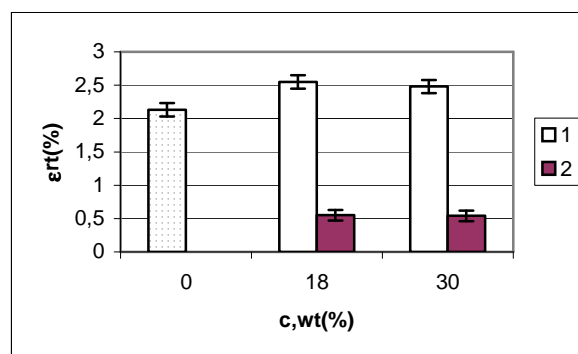


Fig. 10. Dependence of elongation ϵ_{rt} set on soft (1) and hard (2) recyclate content c

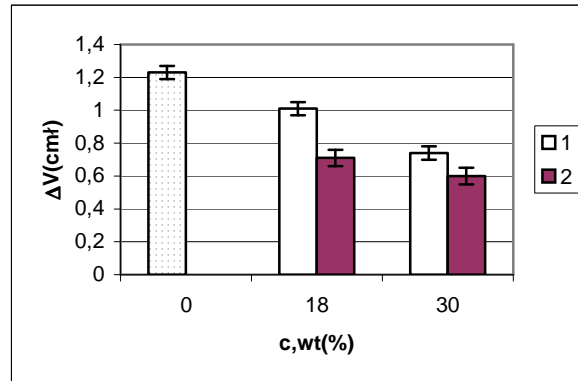


Fig. 11. Dependence of abrasive wear ΔV on soft (1) and hard (2) recycle content c

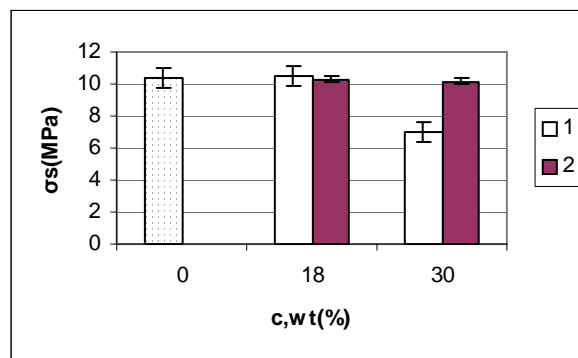


Fig. 12. Dependence of compressive strength σ_s on soft (1) and hard (2) recycle content c

The density of MC DUR 2052 system with soft and hard recycle (Figure 5) decreases, which is due to a lower density of recycle and probably due to the air bubbles occurring on the boundary of the matrix and the filler, remaining there after the mixing process. The elasticity of composites with soft recycle increases (Figure 6), while the elasticity of composites with hard recycle decreases in comparison with the unmodified MC DUR 2052 system. Hard recycles decrease the material ability to dissipate energy. Young's modulus of the materials with hard recycle increases by 30% (Figure 7) and hardness by about 10% (Figure 8). Hard recycle has an influence on the consolidation of this material, but does not work as a notch during the stretching process. Tensile strength of composite with 18% of hard recycle is by about 40% higher than that of unmodified material (Figure 9), but the tensile strength of the composite with 30% of recycle is similar. A decrease in the tensile strength and elongation set (Figure 10) is probably a result of an increase in a number of air bubbles remaining in the composite after the mixing process. Abrasive wear of composites with

hard recyclate decreases by 50% (Figure 11). Due to the introduction of fillers the compressive strength (Figure 12) decreases only in the system containing 30% of soft recyclate.

4. Conclusion

The most important, taking account of the MC Dur floor system, is a significant decrease in the abrasive wear of investigated composites by supplementing them with both soft and hard wastes. The addition of 18 wt. % of hard or soft recyclate in order to modify of MC Dur floor system might be recommended.

Acknowledgements

The authors thank MC Bauchemie Company for the samples of MC Dur 2052.

References

- [1] Rasshofer W.: *Recycling von Polyurethan Kuststoffen*, Hutthing Verlag, Heidelberg, 1994.
- [2] Modesti M.: *Adv Urethane Technol.*, 1996, Vol 13, 237.
- [3] Kozłowski M.: *Podstawy recyklingu materiałów polimerowych*, WPW, Wrocław, 1998.
- [4] Błędzki A.K.: *Recykling materiałów polimerowych*, WNT, Warszawa, 1997.
- [5] Konieczka R., Kałużny W., Sykutera D.: *Kautsch. Gummi Kunst.*, 1997, Vol. 50, 641.

Poliuretanowe pokrycia do ochrony betonowych posadzek z wypełniaczem pochodzącym z recyklingu

Zewnętrzna warstwa systemów posadzkowych do zabezpieczania podłoży betonowych jest wytwarzana z poliuretanów. Warstwa ta powinna odznaczać się dużą wytrzymałością na rozciąganie i dużą odpornością na zużycie ścierne, ponieważ materiały te są stosowane w fabrykach i magazynach oraz na korytarzach. Dotychczas stosowane systemy są mieszaniną poliuretanu i różnych napełniaczy. Właściwości tych systemów można modyfikować, dodając do nich recyklat z poużytkowych odpadów poliuretanów. W ramach pracy wytworzono i zbadano kompozyty z dodatkiem recyklatów o różnej twardości oraz oceniono wpływ zawartości odpadów na zmianę właściwości kompozytów.

Otrzymano kompozyty o większej odporności na zużycie ścierne i o wyższym module sprężystości, zachowując ich niezmienną wytrzymałość na rozciąganie i zginanie oraz wydłużenie do zerwania. Wprowadzenie recyklatów o twardości ok. 50°ShD spowodowało zwiększenie odporności kompozytów na zużycie ścierne o 50%.



Possibilities of diagnosing cavitation in hydraulic systems

W. KOLLEK, Z. KUDŹMA, M. STOSIAK

Institute of Machines Design and Operation, Faculty of Mechanical Engineering, Wrocław University of Technology, 50-371 Wrocław, ul. Łukasiewicza 7/9, Poland
waclaw.kollek@pwr.wroc.pl, zygmunt.kudzma@pwr.wroc.pl, michal.stosiak@pwr.wroc.pl

J. MACKIEWICZ,

Institute of Product Engineering, Faculty of Mechanical Engineering, Szczecin Polytechnic, 70-310 Szczecin, al. Piastów 19, Poland
jan.mackiewicz@ps.pl

Conditions of arising cavitation and experimental investigations of this phenomenon by means of a special vacuum vessel are described. A simulation model of the piston–cylinder unit of a pump with an inclinable cylinder block was used to visualize cavitation in the pump. The results of tests aimed at showing a correlation between the onset of cavitation and an audible diagnostic signal are presented. The suction space of the tested axial-flow multipiston positive-displacement pump with an inclinable cam plate was selected as the most likely place for cavitation to occur. An audible diagnostic signal indicating the onset of cavitation was also detected in the case of a multipiston pump with an inclinable cylinder block. An example of the configuration of an acoustic probe kit for use under industrial conditions is presented.

Keywords: *cavitation, diagnosing*

Nomenclature

d	hydraulic diameter of conduit	[m]
f	frequency	[Hz]
l	measuring length	[m]
L_m	acoustic pressure level	[dB]
n	rotational speed of pump shaft	[min ⁻¹]
p	pressure	[Pa]
p_{cav}	pressure at which air is liberated from hydraulic oil, cavitation onset pressure	[Pa]
p_s	pressure in pump suction stub	[Pa]
p_{scav}	pressure in pump suction stub at onset of cavitation	[Pa]
p_t	pressure in pump pressure stub	[Pa]
Q	rate of flow	[m ³ /s]
Q_n	rated delivery of pump	[m ³ /s]
t	temperature	[°C]
V_{ol}	oil volume	[m ³]
V_{gas}	volume of gas dissolved in oil	[m ³]
z	number of lift elements	[–]

α_V	Bunsen absorption coefficient for oils is in range of 0.7–1.2 (for pressure in MPa)	[-]
ϕ	diameter of air bubble	[m]
Δp	pressure drop along measuring length	[mmHg]
ΔQ_p	drop in pump delivery	[m ³ /s]
μ	absolute viscosity of working liquid	[Ns/m ²]

1. Introduction

The main advantage of a hydrostatic drive is that exceptionally high power flux densities in the power transmission system can be obtained. A working pressure of 35–40 MPa is quite normal today. At such pressure values the power of 1 kW can be generated from a working liquid stream with a volumetric flow rate of just 30–25 cm³/s (1.8–1.5 dm³/min). As a result, the power transmission system's units are characterized by design compactness (low mass per generated or transmitted unit power) unattainable by other kinds of drives. Trends in the development of hydrostatic drives are towards minimizing energy losses and mass and increasing transferred power, and so further increasing the power to mass ratio (Backe [2]).

One of the constraints on this increase is the noisiness of hydrostatic systems and drives, increasing with the amount of generated or transmitted power. Measurement practice and the literature indicate that the positive-displacement pump is usually the noisiest unit in the power transmission system. The causes of the noisiness of hydraulic components and systems include:

- liquid pressure surges,
- pressure fluctuation,
- cavitation.

Considering the above, research on diagnosing the onset of cavitation was undertaken.

2. Cavitation

Cavitation is one of the major constraints imposed on hydraulic system operating specifications such as the maximum rotational speeds of the positive-displacement pumps' shafts and the maximum working medium flow rates at a given hydraulic diameter (Bugala, Szkoda [3]).

The amount of air which an oil can dissolve to reach the saturation point depends on the pressure and temperature conditions under which absorption takes place.

Henry's law, according to which the amount of air dissolved in oil is proportional to the pressure (Kleinbrener [7]):

$$V_{\text{gas}} = a_V \cdot V_{\text{ol}} \cdot p \quad (1)$$

holds for the common range of pressures (up to 30 MPa).

One can say that it is mainly the pressure at which absorption occurs which determines the amount of dissolved air. According to the literature (Głuchowski [6]), the amount of air dissolved in oil AMG-10 at the pressure $p = 20$ MPa is about 20 times larger than the volume of the oil in which absorption took place.

Cavitation appears when the pressure at any point of a hydraulic circuit drops below the saturation point for a given temperature. In order to determine the cavitation onset pressure p_{cav} , the moment when air bubbles appear in the space occupied by the tested oil is observed using the device shown in Figure 1.

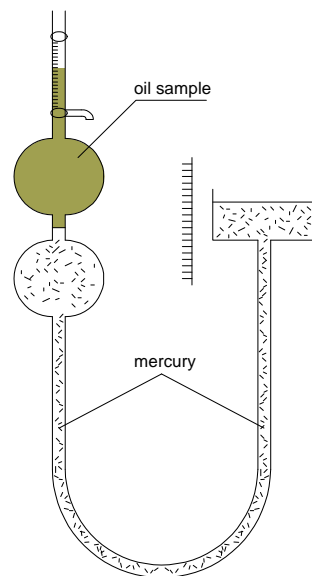


Fig. 1. Device for determining the pressure at which air begins to be liberated (schematic)

The oil tested is in the calibrating tank (the top one). When the upper valve is closed and the test volume is tightly cut off from the environment, the pressure in the test space is reduced by lowering the mercury reservoir. As the latter is slowly lowered, tiny bubbles ($\phi 0.2\text{--}0.3$ mm) begin to appear on the walls around the test volume. As the pressure is further slightly reduced, the tiny bubbles expand and rise, collecting into one small bubble in the upper part of the measuring tube. After about 3–5 minutes no more bubbles appear. As the pressure is further reduced, single, relatively large ($\phi 1\text{--}1.5$ mm) air bubbles begin to appear in the lower part of the space occupied by the oil and slowly move upwards. It is then that the liberation of the air dissolved in the oil can be said to occur. The pressure then prevailing in the space occupied by the tested oil can be regarded as the pressure at which air is liberated from the oil. By heating up (with heat lamps) the oil in the device one can determine the air liberation

pressure for different temperatures. In order to measure the temperature of the oil, a thermo-couple probe is introduced into the calibrating tank.

Graphically the test results are presented as the pressure p_{cav} at which air is liberated as bubbles from hydraulic oil versus temperature (Figure 2).

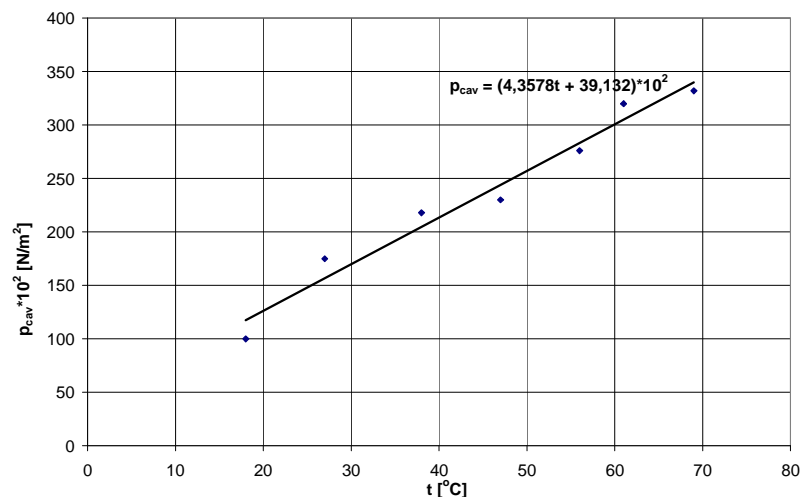


Fig. 2. Influence of temperature on pressure at which air is liberated from hydraulic oil HL 68

By approximating the measuring points (Figure 2) the following analytical relation was obtained:

$$p_{cav} = (4.3t + 39.13) \cdot 10^2. \quad (2)$$

According to relation (2), in a temperature range from 10 to 70 °C (in which oil HL 68 was tested using the vacuum vessel) the cavitation onset pressure $p_{cav} = (75-330) \cdot 10^2$ Pa (absolute pressure).

Even if the pressure p_{cav} is known, in practice it is difficult to determine the beginning of cavitation in a particular place and in a particular power transmission system without measuring the pressure at the point where it is suspected that adverse air liberation from oil takes place (Kudźma and Lempart [11], DyMENIBUS O. H, [5], (Koivula [8], Bachert et al. [1], Lecoffre and Archer [14], Lecoffre [13]).

Moreover, measurement practice (Kollek [9]) shows that the positive-displacement pump belongs to the principal noise-generating sources in hydrostatic power-transmission systems. By his/her choice of the positive-displacement pump the designer codeetermines the system's noisiness. Although axial-flow multipiston pumps are noisiest, their efficiencies and operating specifications are higher than those of other pumps and so they are commonly used in power-transmission systems, particularly high-power ones.

Figure 3 shows a simulation model incorporating a PNZ-25 pump piston and an inlet port with the same dimensions as in a real pump. Oil is fed by a feeding pump through a pipe into the model. Flowing through a rectangular channel simulating the distributor's collector groove the oil is sucked in by a variable delivery pump PNZ-25. The rate of the flow of oil through this channel corresponds to the average shear flow rate (Kudźma and Mackiewicz [12]). The flow rate is measured downstream from the pump by a special flowmeter consisting of gear pump PZ-10 coupled with a CPPU rotational impulse converter. The pressure in the channel is set by a maximum valve and measured by a vacuum meter. The model's piston is driven via a crank mechanism by a hydraulic engine whose rotational speed can be easily changed. The piston performs reciprocating motion effecting the flow of oil through the inlet port into the cylinder and back. As the simulation model's casing is made of organic glass, cavitation in the model cylinder space can be observed and photographs of cavitation during the suction stroke can be taken under stroboscopic illumination. During oscillographic measurements the pressure waveforms in the model cylinder were recorded and the action inside it was filmed with a Pentazet 16 film camera at 2000 frames per second.

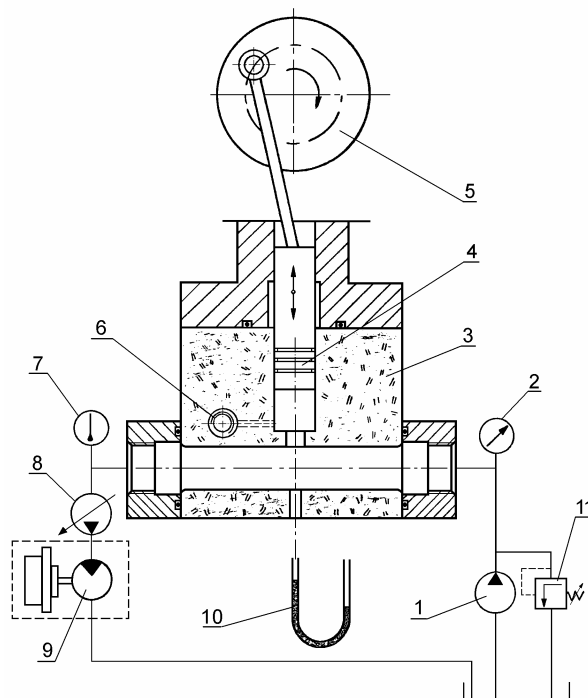


Fig. 3. Simulation model of piston–cylinder–inlet port unit of axial-flow multipiston pump PNZ-25 (hydraulic diagram): 1 – feed pump, 2 – manometer, 3 – organic glass casing, 4 – piston, 5 – crank mechanism, 6 – pressure converter terminal, 7 – thermometer, 8 – sucking in pump, 9 – flowmeter, 10 – underpressure gauge (U-tube), 11 – maximum valve

Figure 4 shows the photographs of the piston during the suction stroke in the simulation model for different pressures p_s in the suction stub. The cylinder pressure waveform during piston motion is marked with a continuous line. The dashed line represents the air liberation pressure determined (at a temperature of 40 °C) using the vacuum vessel shown in Figure 1.

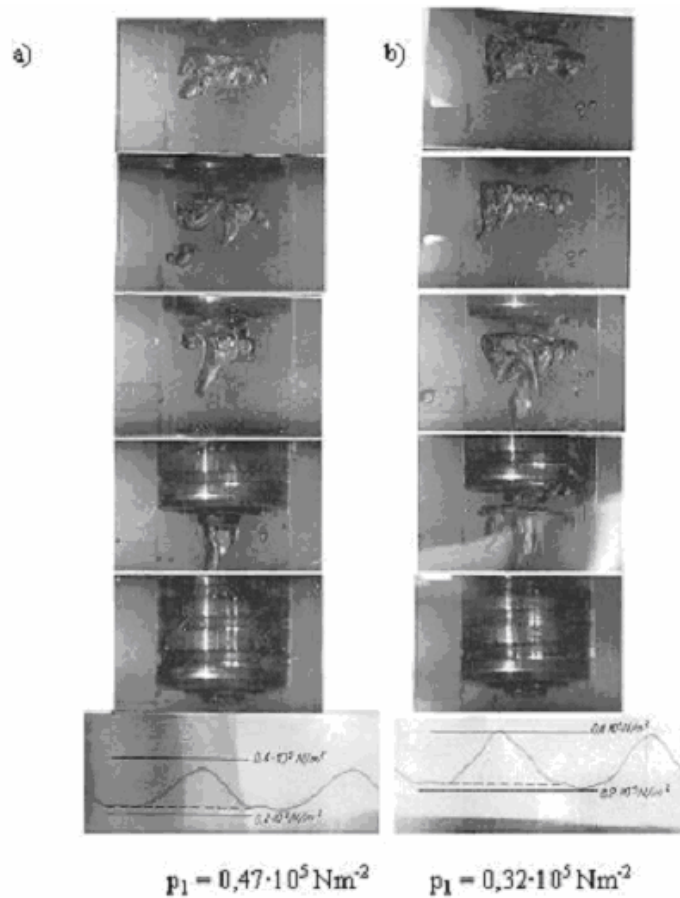


Fig. 4. Liberation of air in simulation pump model cylinder (a), cylinder pressure waveform during suction stroke (b)

3. Audible diagnostic signal in cavitation onset identification

Considering the above, there is a need to undertake research to determine the onset of cavitation in a working hydraulic system. Since the positive-displacement pump's suction space is commonly regarded to be particularly vulnerable to cavitation with all its consequences, investigations into the onset of cavitation, i.e., the instant when air

bubbles begin to be liberated from oil, in the suction stub of a multipiston pump PTOZ2-01-40-R1 with an inclinable cam plate ($Q_{\text{nom}} = 40 \text{ dm}^3/\text{min}$ at $n = 1450 \text{ rpm}$) and in an axial-flow multipiston pump PNZ-25 with an inclinable cylinder block ($Q_{\text{nom}} = 25 \text{ dm}^3/\text{min}$ at $n = 1450 \text{ rpm}$) were carried out. A schematic of the test rig is shown in Figure 5.

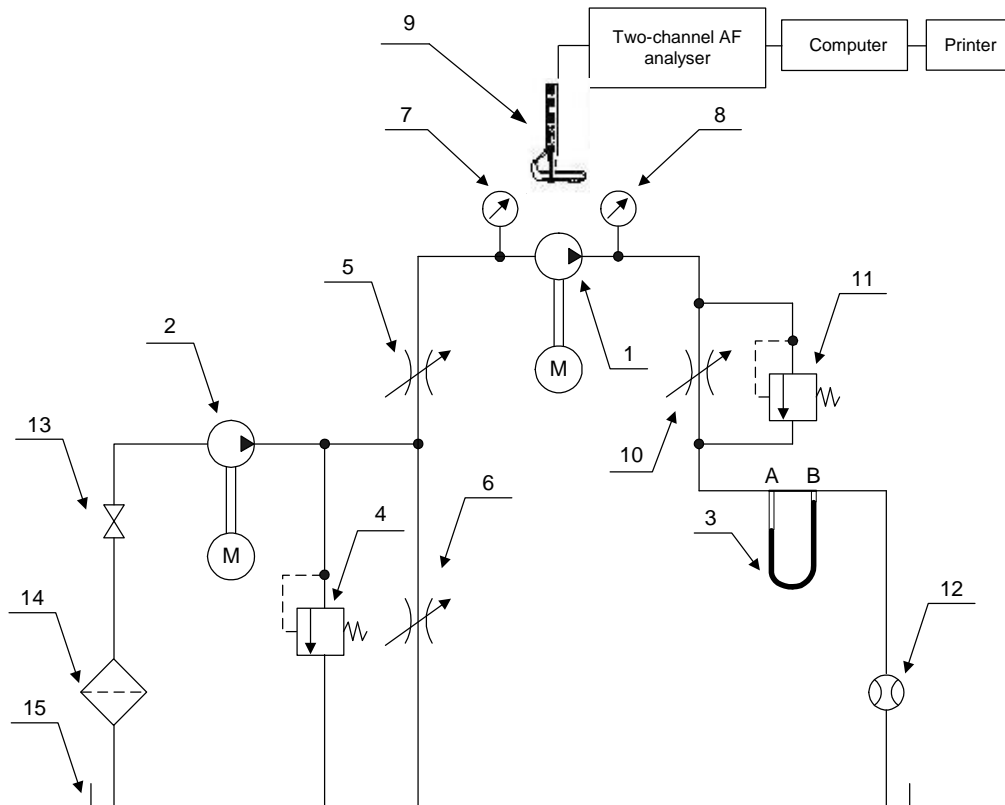


Fig. 5. Schematic of test rig for investigating origin of cavitation: 1 – tested positive-displacement pump, 2 – supercharging pump, 3 – U-tube on 1 m long pipe, 4 – maximum valve, 5 – adjustable throttle valve, 6 – adjustable throttle valve, 7 – vacuum meter, 8 – manometer, 9 – B&K ZB0017 acoustic probe, 10 – adjustable throttle valve, 11 – maximum valve, 12 – flowmeter, 13 – cut-off valve, 14 – filter, 15 – tank

4. Description of investigations

A multipiston pump PTOZ2-01-40-R1 (with an inclinable cam plate) made by PZL-HYDRAL Wrocław or a PNZ-25 pump (with an inclinable cylinder block) made by HYDROMA-Szczecin was used in the investigations. Acoustic probe 9 with the associated equipment was located in the vicinity of the tested pump (1) driven by a d.c. motor. The system is protected against overload by maximum valve 4. The

working liquid is sucked in through filter 14 by supercharging pump 2 and fed into the system. Adjustable maximum valve 5 sets the suction pressure in pump 1. The pressure in the suction stub of pump 1 was checked by vacuum meter 7 to make sure that it corresponded to its test plan value. Adjustable throttle valve 10 sets the forcing pressure of pump 1. Manometer 8 indicates the forcing pressure of pump 1, set at 8 MPa. Maximum valve 11 protects against an excessive increase in pressure on the pump's delivery side. U-tube 3 indicated (highly accurately) the flow loss, being a measure of a drop in pump delivery, in a 1 m long steel pipe with an inside diameter of 0.014 m. A pressure drop Δp [mmHg] along the measuring length versus suction pressure p_s [MPa] of pump 1 was plotted. Drop in delivery $\Delta Q_p = 2\% Q_n$ was adopted as the hydraulic criterion for the onset of cavitation.

Since a laminar flow occurs, the Hagen–Poiseuille equation holds true:

$$\Delta p = \frac{128 \cdot Q \cdot \mu \cdot l}{\pi \cdot d^4}. \quad (3)$$

If it is assumed that

$$\frac{d^4 \cdot \pi}{128 \cdot \mu \cdot l} = A = \text{const},$$

the above equation can be written as: $Q = A \cdot \Delta p$, which represents the linear relation between Q and Δp .

4.1. Tests on multipiston pump with inclinable cam plate

The tests consisted in the simultaneous measurement of the pressure in the pump's suction stub, the pressure drop along measuring length $A-B$ and the sound pressure level. The onset of cavitation was assumed to correspond to a 2% drop in delivery. The suction pressure at this instant was assumed as p_{scav} . As the acoustic pressure level was recorded, an audible signal whose value sharply increased at the onset of cavitation was detected. In addition, spectral analysis of noise in the cavitation range shows the predomination of higher components over the fundamental component (which is the highest in a noncavitation area).

5. Test results

The pressure drop Δp (along the measuring length $A-B$ as shown in Figure 4) at a constant pump forcing pressure and variable (in accordance with the test plan) suction pressure p_s was measured and on this basis the graph $\Delta p-p_s$ was plotted.

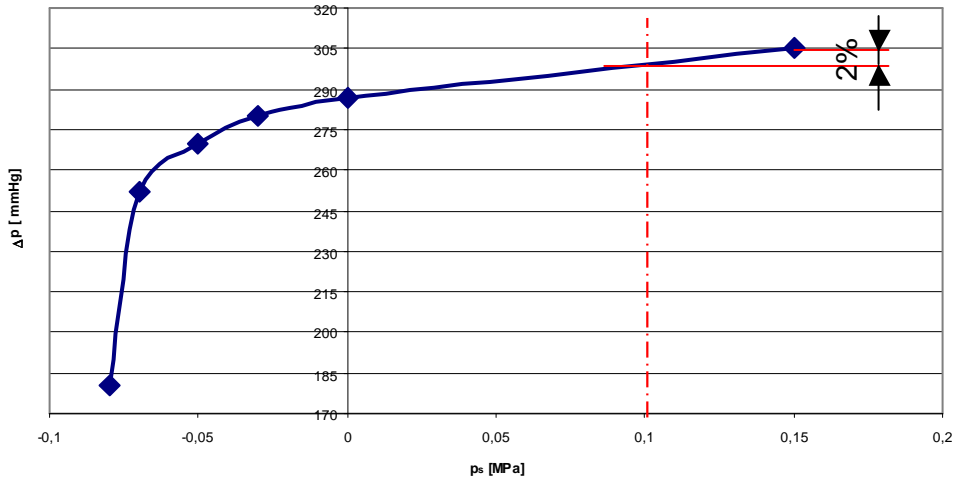


Fig. 6. Flow loss Δp , being measure of drop in pump delivery, versus suction pressure p_s at 1500 rpm and forcing pressure $p_t = 8$ MPa. Tested pump PTOZ2-01-40-R1 with inclinable cam plate

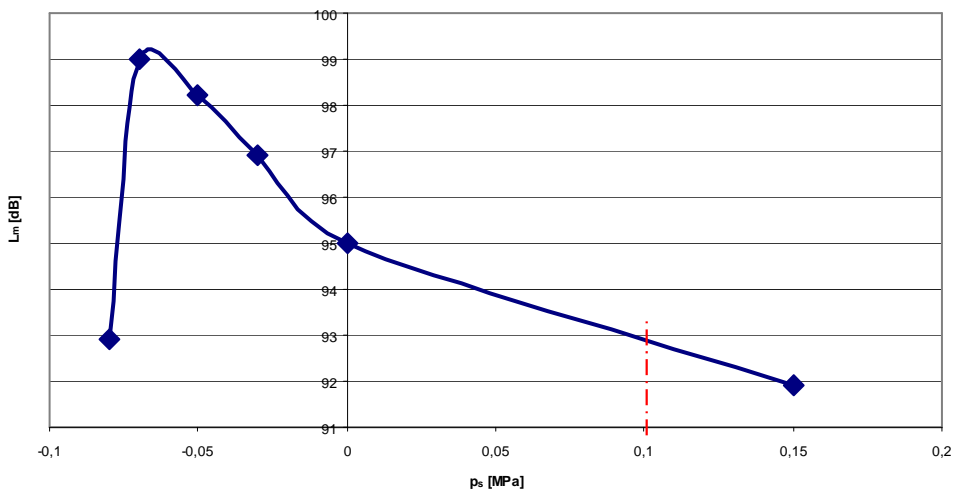


Fig. 7. Sound pressure L_m versus suction pressure p_s at 1500 rpm and forcing pressure $p_t = 8$ MPa. Tested pump PTOZ2-01-40-R1 with inclinable cam plate

After processing the measured signals, the third-octave spectra of the acoustic pressure level and a waveform of pressure fluctuation on the tested pump's suction side and delivery side were obtained (Figures 8 and 9).

As the rotational speed was fixed at $n = 1500$ rpm and the tested multipiston pump PTOZ2-01-40-R1 had $z = 7$ pistons, the dominant frequency was $f \approx 175$ Hz. A sound pressure level L_m versus pump suction pressure bar chart was constructed for the first three harmonic components of the third-octave spectrum, as shown in Figure 10.

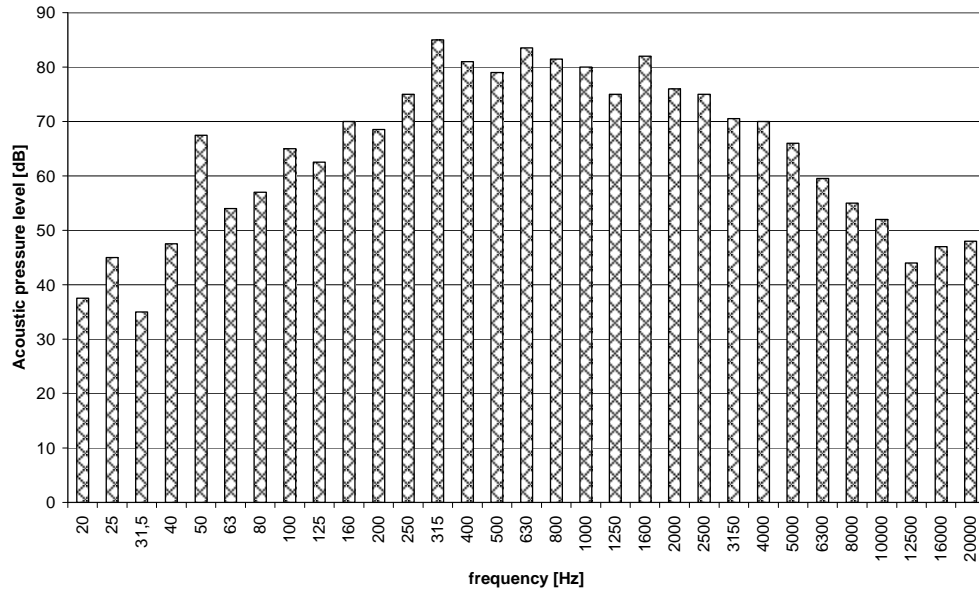


Fig. 8. Third-octave spectrum of sound pressure for pump PTOZ2-01-40-R1; $n = 1500 \text{ min}^{-1}$; forcing pressure $p_t = 8 \text{ MPa}$; suction pressure $p_s = 0.15 \text{ MPa}$. Flow without cavitation in pump channels

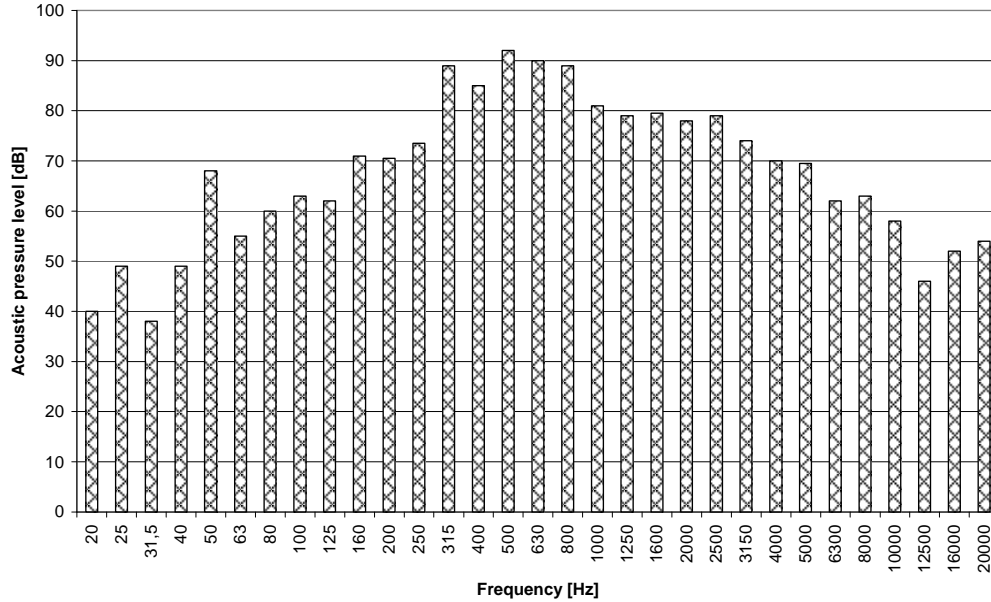


Fig. 9. Third-octave spectrum of sound pressure for pump PTOZ2-01-40-R1; $n = 1500 \text{ min}^{-1}$; forcing pressure $p_t = 8 \text{ MPa}$; suction pressure $p_s = -0.03 \text{ MPa}$. Flow with cavitation in pump channels

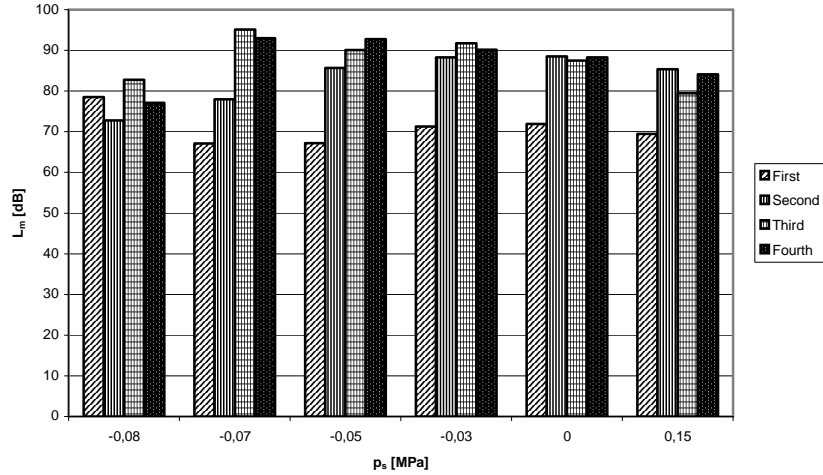


Fig. 10. Sound pressure level L_m versus suction pressure at 1500 rpm and forcing pressure $p_f = 8$ MPa; three harmonic components of third-octave spectrum. Tested pump PTOZ2-01-40-R1 with inclinable cam plate

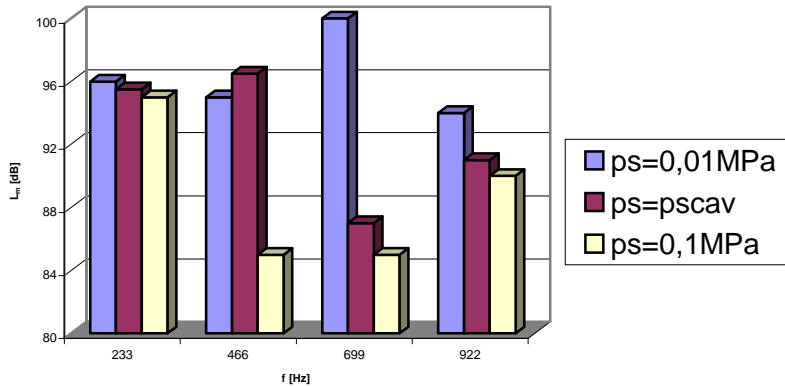


Fig. 11. Amplitude spectrum of sound pressure L_m versus suction conduit pressure p_s for pump PNZ-25 with inclinable cylinder block

A bar chart (Figure 11) showing the level of four consecutive spectral sound pressure components for different pressures in the tested pump's suction conduit was constructed for the PNZ25 pump with an inclinable cylinder.

6. Conclusion

The presented results reveal a significant relationship between cavitation and the acoustic effect, as reflected by the increase in the sound pressure level L_m as cavitation develops (Figures 8 and 9). This is corroborated by the graphs of respectively: pres-

sure drop Δp versus suction pressure p_s and sound pressure level L_m versus suction pressure p_s , shown in Figures 6 and 7. One should notice that as the pressure in the pump's suction conduit, measured in the suction stub, falls down to negative values, the emitted noise greatly increases (by about 10 dB) and a clearly audible diagnostic signal indicating cavitation pump operation can be heard. Moreover, the included analyses show that higher harmonic components of the noise spectrum dominate when the pump is operating in the cavitation range (Figures 10 and 11). The acoustic criterion can be applied under industrial conditions through an acoustic probe (Figure 12) – an instrument which is easy to use and sufficiently precise as demonstrated by Doma-gała and Kollek [4] as well as by Kollek et al. [10].

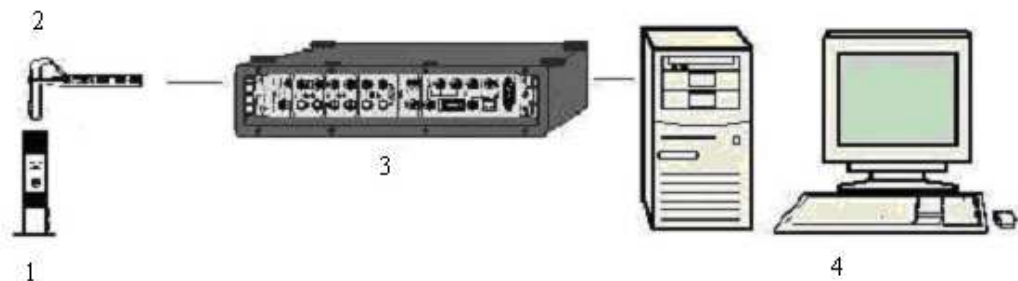


Fig. 12. Block diagram of measurement path incorporating acoustic probe: 1 – intensity calibrator B&K 3541, 2 – acoustic probe B&K ZB0017, 3 – two-channel frequency analyser B&K 2144, 4 – PC

References

- [1] Bachert R., Ludwig G., Stoffel B., Frobenius M., Schilling R.: *Three-dimensional unsteady cavitation effects on a single hydrofoil and in a radial pump – measurements and numerical simulations*, Fifth International Symposium on Cavitation (CAV2003), Osaka, 2003, Japan.
- [2] Backe W.: *Entwicklung der Hydraulik für mobile Anwendungen*, 12 AFK, Aachen, 1996, Germany.
- [3] Bugała R., Szkoda M.: *Cavitation damage curves and fractional distribution of cavitation load* (in Polish), Domestic Conference on Selection and Use of Engineering Materials, Gdańsk Polytechnic, Jurata, 1997, Poland.
- [4] Domagała T., Kollek W.: *Possibilities of applying energy methods to diagnosing acoustic state of hydraulic machines* (in Polish), Series: Sprawozdania, report no. S-058/97, Wrocław University of Technology, Wrocław, 1997, Poland.
- [5] DyMENIBUS O. H.: *Degazage de Fluide Hydraulique. Energie Fluide l'Air Industriel*, Hors serie cahur technique, 1984, 2.
- [6] Głuchowski E.: *Air in hydraulic systems* (in Polish), Przegląd Mechaniczny, 1973, No. 9.
- [7] Kleinbrener W.: *Werkstoffzerstörung durch Kavitation in ölhydraulischen Systemen*, Industrie Anzeiger, 1976, No. 61.

- [8] Koivula T.: *On cavitation in fluid power*, Proc. of 1st FPNI-PhD Symp, Hamburg, 2000, Germany.
- [9] Kollek W., Kudźma Z., Rutański J.: *Effectiveness in reducing noise of heavy earthmoving machines with hydrostatic drive* (in Polish), Ninth Conference on Development of Earthmoving Machinery, Zakopane, 1996, Poland.
- [10] Kollek W., Kudźma Z., Stosiak M.: *Acoustic diagnostic testing in identification of phenomena associated with flow of working medium in hydraulic systems* (in Polish), Twelve Power Seminar '2003 on Current Flow, Design and Operational Problems of Hydraulic Machines and Equipment, Gliwice, 2003, Poland.
- [11] Kudźma Z., Lempart A.: *Endurance testing of non-return valves of low-speed hydraulic engines* (in Polish), *Hydraulika i Pneumatyka*, 1996, No. 1.
- [12] Kudźma Z., Mackiewicz J.: *Influence of multipiston pump's operating specifications on its noisiness in cavitation conditions* (in Polish), Scientific-Technical Conference '96 on Hydraulic Drives and Controls, Szklarska Poręba, 1996, Poland.
- [13] Lecoffre Y.: *Cavitation Erosion, Hydrodynamic Scaling Laws, Practical Method of Long Term Damage Prediction*, CAV'95 International Symposium on Cavitation, Deauville, 1995, France.
- [14] Lecoffre Y., Archer A.: *A method to evaluate cavitation erosion in valves*, Third International Symposium on Cavitation, Grenoble, 1998, France.

Możliwości diagnozowania kawitacji w układach hydraulicznych

W artykule przybliżono warunki, w jakich może powstawać zjawisko kawitacji, opisując przebieg przeprowadzonych badań doświadczalnych z wykorzystaniem specjalnego naczynia próżniowego. Przedstawiony model symulacyjny zespołu tłoczek–cylinder pompy z wychylnym blokiem cylindrów umożliwił autorom wizualizację zjawiska kawitacji w pompie. Przedstawiono ponadto wyniki badań eksperymentalnych, których celem było wykazanie korelacji między początkiem powstawania kawitacji a akustycznym sygnałem diagnostycznym. Jako miejsce szczególnie narażone na wystąpienie kawitacji wytypowano obszar ssania badanej pompy wporowej wielotłokowej osiowej z wychylną tarczą. Wykazano również występowanie akustycznego sygnału diagnostycznego świadczącego o początku powstawania kawitacji w przypadku pompy wielotłokowej w wychylnym blokiem cylindrów. Przedstawiono też przykładową konfigurację zestawu z sondą akustyczną, którą można wykorzystać w warunkach przemysłowych.



Optimum assembly automation level selection module as the component of advisory system

B. REIFUR

Wrocław University of Technology, Wybrzeże Wyspiańskiego 25, 50-370 Wrocław

When designing assembly processes it is particularly difficult to determine the optimum automation level, i.e., the ratio of manual to automatic assembly operation times. This factor considerably affects the productivity since it determines product assembly labour intensity, the number of assemblers and the type and cost of equipment. The system module presented allows considerable flexibility in the analysis and assessment of product suitability for automatic assembly, the selection of assembly equipment and the creation of new configurations of assembly stands, depending on changing needs of manufactured products. By interrelating product design and technological features with productivity and production cost-effectiveness ratios the module allows one to derive a simpler and more objective method of determining the automation level.

Keywords: *automatic assembly, module, expert system*

1. Assembly automation level

In the last decade, increasing production automation has seemed to be the only proper strategy to remain competitive in the highly developed countries. As a result, the number of companies using advanced automated assembly systems have shot up. At the same time the number of opinions suggesting that for many companies unlimited automation amounts to a costly engineering transformation have been growing. The opinions have become increasingly credible as the number of reports about companies which had bet on automation solutions and now started to back out searching for reduced automation level concepts increased. The anticipated economic benefits have been quickly reduced by unforeseen costs: manufacturing chain losses, losses due to assembly line stoppages, the necessity of employing a large number of technical assistance and service personnel, the high costs of changing over to new product models and the high spare parts inventories needed to meet the demand.

Because of the increasingly asked questions about assembled products' design and producibility and the price of a wrong choice of an automation level more and more research centres do assessments of the producibility of products to be automatically assembled and the suitability of product components for such assembly. Automated systems began to be widely implemented without giving thought to the producibility of the products to be assembled in this way or to the producibility of the assembly joints which determine the costs of the assembly operations.

Because of the changing demand for short runs of new products the designer and the production engineer must be equipped with specialized advisory systems to help them assess the suitability of a product component for automated assembly and the economic feasibility of the assembly process.

Optimum assembly automation level selection is made possible by the assembly process analysis & assembly equipment selection system (described in SOP 04") developed by the author [5], currently supplemented with a module assessing the suitability of product parts for automatic assembly and selecting the optimum automation level and the type and cost of equipment.

If automatic assembly systems are to be effectively used, the parts, the assembly units and the whole product must be properly designed. Therefore special attention should be given to this requirement. The design and technological preparation of a product for automated assembly requires continuous analysis and evaluation, resulting in improved producibility of the design. For this purpose the producibility indicators of the parts, the assembly units and the assemblies are usually defined and weights are assigned to them whereby automatic product assembly possibilities can be evaluated and compared and the indicators can be calculated. It is necessary to verify continuously the producibility of a designed product during manufacturing, because for many reasons producibility issues are not analysed properly at the design stage and later.

The design solutions of a product and its components to be automatically assembled determine not only the ease of assembly, but also the design (structure) of the assembly machines and of the special devices and tools. Product producibility is also closely connected with the reliability and stable operation of the assembly equipment.

In order to ensure proper product design producibility [1, 2], a special approach to the design of the individual parts should be adopted. Parts for automatic assembly should be characterized by:

- high amenability to automatic orientation and feeding into assembly machines,
- high amenability to reliable basing and transporting in assembly position zones,
- optimum automatic joining and control parameters,
- a minimum number of parts in the assembled product,
- the simplest possible design,
- modularity and automatic assembly of modules.

In an automated assembly system, the individual parts must be delivered in a specific way to the places where joining is performed. Therefore all the elements crucial for the behaviour of the parts in the manipulation processes and affecting the way in which the joint is made must be identified. Assembly joining should take into account the mutual orientation of the assembled parts (one of them being the base part and the other, the attached part), the joining of the parts, i.e., bringing into contact the proper surfaces, and the fixing of the joint, i.e., immobilization of the two parts relative to each other.

Using design and joint producibility evaluation algorithms the developed computer expert system automatically determines the suitability of a product design for automatic assembly. The algorithm of product and assembly evaluation (from the producibility point of view) criteria allows designers and process engineers to select the most advantageous solutions and avoid accidental errors. Given a detailed description of an assembly joint the program performs an in-depth analysis of the assembly joint, evaluates its suitability for automatic assembly and gives an expert opinion about the design, indicating its faulty elements.

2. System of evaluating producibility of parts and units to be automatically assembled

The presented module evaluating the producibility of a design and its suitability for automatic assembly was built using frame knowledge base systems, artificial neural networks and specially developed software procedures. The module is based on GURU.

The developed system allows one to analyse a design and the joints in it, using the form shown in Figure 1, and to derive the results. In order to evaluate the producibility of a design the system asks the user a series of questions. The questions are displayed in successive dialogue windows where the user may answer 'Yes' or 'No' to the question asked.

If any product feature is incompatible with the general producibility rules for automatically assembled structures, a message (see Figure 1b) about the irregularity is displayed in the field 'Expert Opinion'. If the system does not detect any structural errors, the message 'The structure is correct with regard to producibility' will be displayed (Figure 1c).

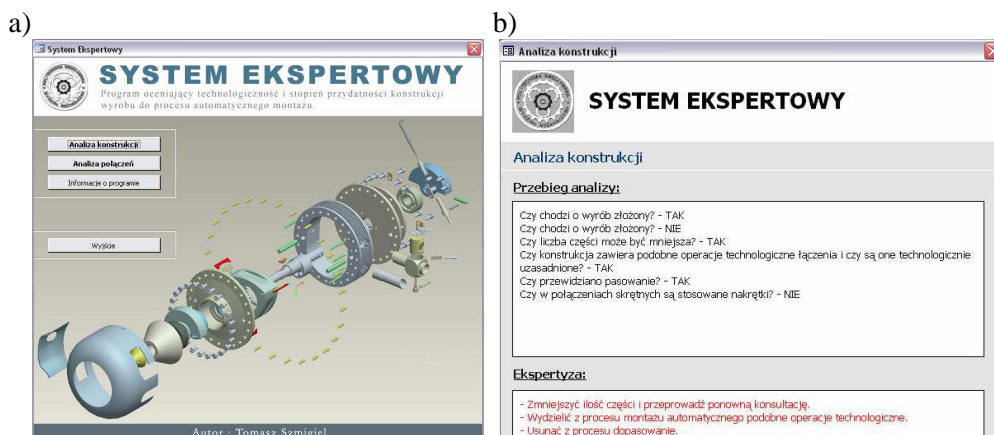


Fig. 1a,b. Expert system design consultation and analysis windows

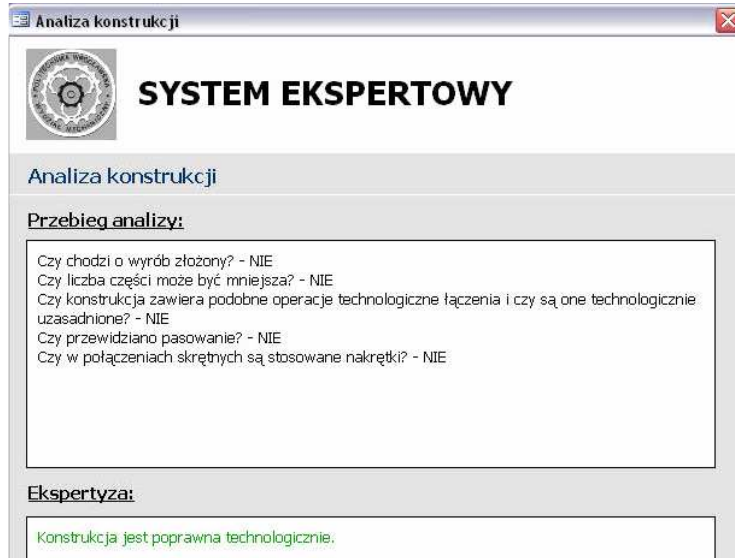


Fig. 1c. Expert system design consultation and analysis windows

When the option ‘Analysis of joints’ is selected, consultation with the system begins (Figure 1d). One must enter the assembly joint’s major features such as: base part class, attached part class, orientability (the number of axes and symmetry planes), overall dimensions (length, width/diameter, height), material, type of joint, accuracy, mass of parts and type of surface.

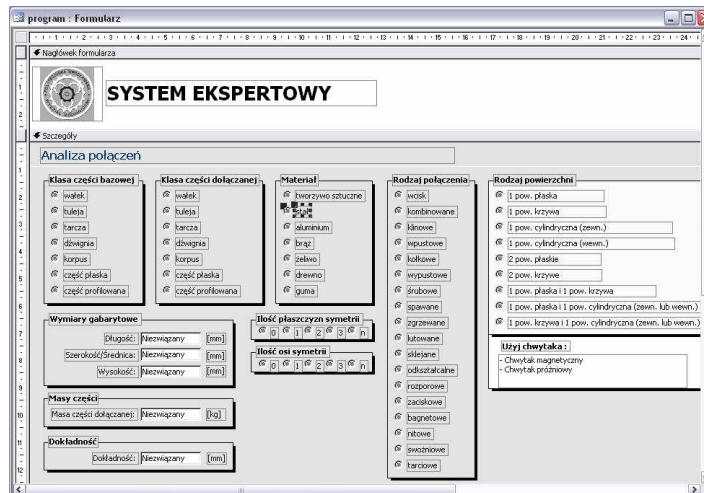


Fig. 1d. Expert system design consultation and analysis windows

Once the data have been entered, the system analyzes them and using the knowledge base gives an expert opinion, assesses whether the joint is suitable for automatic assembly and recommends (in the form of a detailed report or a message, depending on the selected option) a gripping device (Figures 2 and 3).

SYSTEM EKSPERTOWY
Przydatność konstrukcji wyrobu do procesu montażu automatycznego

Informacje o połączeniu

Klasa części bazowej: Walek	Długość: 12,25 [mm]
Klasa części dołączanej: Tuleja	Szerokość / Średnica: 21,25 [mm]
Materiał: Stal	Wysokość: 15,22 [mm]
Rodzaj połączenia: Włosk	
	Masa części bazowej: 1,25 [kg]
Ilość płaszczyzn symetrii: 3	Masa części dołączanej: 1,36 [kg]
Ilość osi symetrii: 1	Dokładność: 0,12 [mm]

Chwytnak

Rodzaj powierzchni: 1 pow. płaska
Użyj chwytaka: - Chwytnak magnetyczny
- Chwytnak próżniowy

Ekspertyza

Połączenie nadaje się do montażu automatycznego

Fig. 2. Final expert opinion in report form

SYSTEM EKSPERTOWY
Przydatność konstrukcji wyrobu do procesu montażu automatycznego

Informacje o połączeniu

Klasa części bazowej: Walek	Długość: 356 [mm]
Klasa części dołączanej: Tuleja	Szerokość / Średnica: 12,6 [mm]
Materiał: Gum	Wysokość: 3,56 [mm]
Rodzaj połączenia: Lutowane	
	Masa części bazowej: 1,58 [kg]
Ilość płaszczyzn symetrii: 3	Masa części dołączanej: 6,68 [kg]
Ilość osi symetrii: 0	Dokładność: 0,1 [mm]

Chwytnak

Rodzaj powierzchni: 1 pow. płaska
Użyj chwytaka: - Chwytnak magnetyczny
- Chwytnak próżniowy

Ekspertyza

To połączenie NIE nadaje się do montażu automatycznego:

- Łączone elementy są zbyt ciężkie!
- Części te są trudnoorientowalne. Przeprojektuj konstrukcję tak aby części miały jak najwięcej osi i płaszczyzn symetrii!
- Takie utrwalenie połączenia jest rzadko stosowane i nie nadaje się do montażu automatycznego. Spróbuj zastosować inne połączenie i przeprowadź ponowną analizę!

Fig. 3. Report with appropriate design recommendations

If the joint does not satisfy the producibility requirements, the program explains why the design is unsuitable for automatic assembly and offers design recommendations (an expert opinion in Figure 3).

3. Automation level selection module

When designing assembly processes it is particularly difficult to determine the optimum automation level, i.e. the ratio of manual to automatic assembly operation times.

This factor considerably affects the productivity since it determines product assembly labour intensity, the number of assemblers and the type and cost of equipment. An incorrect degree of automation entails additional costs, lower productivity or flexibility and often the need for new investments aimed at reducing this degree.

The rather inefficient existing methods of determining the optimum assembly automation level, consisting in the subjective assessment of automation levels for a few variants, calculation of their cost-effectiveness and the selection of a solution which best meets the initial assumptions are very time-consuming and the results are often rather unsatisfactory. This later leads to problems with productivity and further expenditures aimed at reducing the degree of automation.

The principle of relating product design and technological features to productivity and cost-effectiveness allows one to objectively determine the automation level and justify the assembly equipment configuration [4].

As a numerical assembly automation level characteristic it is purposeful to use relative quantity X_j :

$$X_j = 1 - \frac{t_p}{t_j}, \quad (1)$$

where:

t_p – a manual product assembly labour intensity, in min.;

t_j – the product assembly labour intensity for the j -th process variant, in min.

According to the above, depending on the necessary parameter, all the assembly processes are in an interval of 0–1, where $X = 0$ corresponds to manual assembly and X increases with the automation level. For example, in assembly automation level calculations (for different types of production) in [6] X is equal to zero for manual assembly, up to 0.25 for mechanized assembly, close to 1 for semiautomatic assembly and equal to 1 for automatic assembly.

Considering that the kind of product, the product manufacturing conditions, the kind of equipment, the automation level and the production cost-effectiveness ratios are interconnected in the assembly process, a functional-cost analysis in which the above parameters were considered in relation to each other was carried out. The main criterion interrelating the above parameters was a reduction function in the form [6]

$$Z_j = (\delta + \beta) \cdot S \cdot N \cdot t_j + E_n \cdot \sum_{i=1}^M A_{ij} a_{ij}, \quad (2)$$

where:

Z_j – the variable part of reduced expenditures, in PLN/year,

M – the number of operations needed to completely assemble a product, in units,

j – a variant number,

i – an operation number,

$\delta = 1.5$ – a pay + charges ratio,

β – total charges proportional to direct pay,

S – the assembler's per minute rate,

N – an annual product production program, in units,

E_n – a standard capital effectiveness coefficient (about 1.15–1.25),

t_j – the product assembly labour intensity, in min.,

A_{ij} – a device unit cost in the i -th operation, in PLN,

a_{ij} – the number of devices operating in parallel in the i -th operation.

Minimum automation level X_{\min} corresponds to the minimum of function (3) and is calculated from the following relation [6]:

$$X_{\min} = 1 - \sqrt{\frac{E_n \cdot \left[(p_1 + q_1) + \frac{p_2 + q_2}{N} \right]}{(\delta + \beta) \cdot 8 \cdot S \cdot t_p}}, \quad (3)$$

where:

E_n – a standard capital effectiveness coefficient (about 1.15–1.25),

p_1, q_1, p_2, q_2 – simple regression coefficients,

N – an annual product production program, in units,

δ – a pay + charges ratio,

β – total charges proportional to direct pay,

S – the assembler's per minute rate,

t_p – the product manual assembly labour intensity, in min.

An exemplary optimum automation level for any gear pump production program is shown in Figure 4.

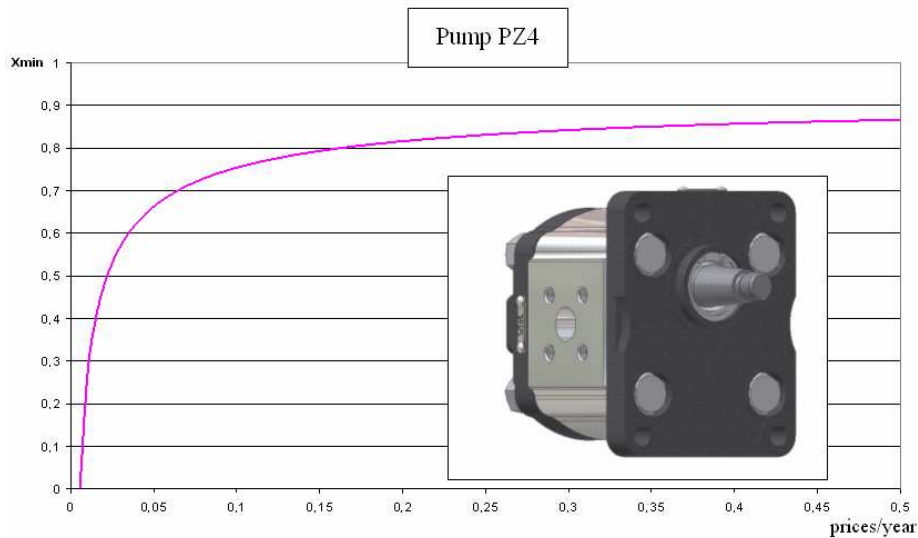


Fig. 4. Automation level (X_{\min}) depending on gear pump PZ4 production program

4. Conclusion

The developed system is an effective software tool for designers and planners, enabling work in a hardware-software environment specifically geared to the comprehen-

sive solving of design and technological tasks and problems, including assembly joints analysis and assembly organization. Thanks to this system one can take informed decisions about the suitability of a given coupling for automatic assembly and get an expert opinion indicating faulty places in the design. As a result the time which the designer would spend on a series of time-consuming routine intellectual activities is much reduced.

The main advantages of the engineering design decision aiding AI-based computer system include:

- design time reduction,
- quick access to the results of work,
- easy modifiability in cases where the initial data are changed at different design stages,
- reduction in the costs of designing the required technology.

The presented advisory system combined with the assembly work zone analysis and design modules for the selection of auxiliary instrumentation, transport systems, feeders, etc., brings notable benefits stemming from reductions in design implementation costs and design process preparation time.

References

- [1] Żurek J., Briese W.: *Algorithmization of producibility evaluation for automatically assembled machine parts and units* (in Polish), Technologia i Automatyizacja Montażu, 1999, No. 4.
- [2] Łunarski J.: *Producibility of automatically assembled machine structures* (in Polish), Wyd. OBR TEKOMA, Warsaw, 1991.
- [3] Reifur B.: *Costs of automatic orientation equipment as expert system module* (in Polish), Technologia i Automatyizacja Montażu, 2002, No. 4.
- [4] Zha X.F., Du H.J.: *Knowledge-based approach and system for assembly oriented design. Part I. The approach*, Engineering Applications of Artificial Intelligence I, 1 Febr. 2001.
- [5] Reifur B.: SOP, Cracow, 2004.
- [6] Zenkin A.S., Łabutina W.O., Kozęłto N.Ł.: *Wyznaczanie optymalnego poziomu automatyzacji procesów technologicznych montażu wyrobów*, Technologia i automatyzacja montażu, 2003, No. 2.

Moduł wyboru optymalnego poziomu automatyzacji montażu jako składnik systemu doradczego

Podczas projektowania procesów technologicznych montażu szczególnie trudnym zadaniem jest wyznaczenie optymalnego poziomu automatyzacji, tzn. stosunku czasów ręcznie i automatycznie wykonywanych zabiegów związanych z montażem wyrobu. Czynniki te znacznie wpływają na efektywność produkcji, ponieważ determinuje pracochłonność montażu wyrobu, liczbę monterów oraz typ urządzeń i ich koszty. Zaprezentowany moduł systemu

umożliwia znaczną elastyczność w analizie i ocenie przydatności wyrobu do automatycznego montażu, doborze urządzeń montażowych, tworzeniu nowych konfiguracji stanowisk, odpowiednio do zmieniających się potrzeb produkowanych wyrobów. W powiązaniu cech konstrukcyjnych i technologicznych wyrobu ze wskaźnikami efektywności i ekonomiczności produkcji umożliwia uzyskanie prostszej i obiektywnej metody wyznaczania poziomu automatyzacji.



Determination of the flow curves of austenite steel wire in the drawing process

J. PRZONDZIONO, D. HALACZEK, J. SZYMSZAL

Silesian Technical University, ul. Krasińskiego 8, 40-019 Katowice

Flow curves enable to predict the response of material during metal forming processes. To establish properly the magnitude of flow stress, precise determination of the true stress from a tensile test is necessary. Calculation of true stress corresponding to the proof strength made it possible to determine the flow curves and select the appropriate flow stress equation for the tested drawn wires.

Keywords: *mechanical properties, tensile test, flow curve, wire drawing, austenite steel*

1. Introduction

One of the elements that determine obtaining correct characteristics of technological plasticity of materials is proper description of flow stress functions. Flow curves enable to predict the response of material during metal forming [1,2]. An important matter for the correct determination of flow stress values is precise determination of true stress that wire samples undergo while tensile test.

Presented test results showed to what extent the true stress defined for the range of plastic strain differs from conventional stress (F/S_0) determined in the tensile test. Calculations that were made, enabled to determine the flow curves of drawn wire made of austenite stainless steel together with the description of flow stress functions.

2. Methodology of research

To determine the true stress it is necessary to calculate real section area of a sample S and force applied F . Calculation of the real sample section area requires determination of real sample diameter d that changes due to present elastic and plastic elongation which are respectively transferred to transverse strain components. This diameter can be calculated by means of the following equation [3]:

$$d = d_0 + \Delta d_e + \Delta d_p, \quad (1)$$

where:

d_0 – initial sample diameter,

Δd_e – modification of sample diameter as result of elastic strain,

Δd_p – modification of sample diameter as result of plastic strain.

Within the range corresponding to the contribution of elastic strain in the total strain, the transverse strain component Δd_e can be calculated by means of the following equation:

$$\Delta d_e = -\nu \cdot \frac{F \cdot d_0}{E \cdot S_0} \quad (2)$$

where:

ν – Poisson's ratio,

E – Young's modulus,

S_0 – initial section area.

Elastic strain ε_{1e} then can be calculated by means of the following equation:

$$\varepsilon_{1e} = \frac{F}{E \cdot S_0} \cdot \quad (3)$$

Modification of diameter (Δd_p), caused by plastic strain, can be calculated by means of the following equation:

$$\Delta d_p = d_0 \cdot \left(e^{\frac{1}{2} \ln \left(\frac{l_0 + \Delta l}{l_0} \frac{F}{E \cdot S_0} \right)} - 1 \right) = d_0 \cdot \left(e^{\ln \left(\sqrt{\frac{1}{\left(\frac{l_0 + \Delta l}{l_0} \frac{F}{E \cdot S_0} \right)}} \right)} - 1 \right) \quad (4)$$

If we assume that $e^{\ln x} = x$, the Equation (4) will be as follows:

$$\Delta d_p = d_0 \cdot \left(\sqrt{\frac{1}{\frac{l_0 + \Delta l}{l_0} \frac{F}{E \cdot S_0}}} - 1 \right) \quad (5)$$

Considering total change of diameter, that is the global effect of elastic ε_{de} and plastic strain ε_{dp} , the actual section area of sample S is calculated by means of the following equation:

$$S = \frac{\pi}{4} d^2 = \frac{\pi}{4} \left[d_0 - \frac{\nu \cdot F \cdot d_0}{E \cdot S_0} + d_0 \cdot \left(\sqrt{\frac{1}{\frac{l_0 + \Delta l}{l_0} - \frac{F}{E \cdot S_0}} - 1} \right) \right]^2. \quad (6)$$

Having done adequate transformations this equation assumes the following shape:

$$S = S_0 \left[1 - \frac{\nu \cdot F}{E \cdot S_0} + \left(\sqrt{\frac{1}{\frac{l_0 + \Delta l}{l_0} - \frac{F}{E \cdot S_0}} - 1} \right) \right]^2 = S_0 \left[\sqrt{\frac{1}{\frac{l_0 + \Delta l}{l_0} - \frac{F}{E \cdot S_0}} - \frac{\nu \cdot F}{E \cdot S_0}} \right]^2 \quad (7)$$

Final equation of the true stress is as follows:

$$\sigma = \frac{\frac{F}{S_0}}{\left[\sqrt{\frac{1}{\frac{l_0 + \Delta l}{l_0} - \frac{F}{E \cdot S_0}} - \frac{\nu \cdot F}{E \cdot S_0}} \right]^2}. \quad (8)$$

For the load corresponding to the proof stress ($R_{p0.2}$), the value of true stress can be calculated by means of the Equation (8):

$$\sigma_{0.2} = \frac{R_{p0.2}}{\left[\sqrt{\frac{1}{1.002} - \frac{\nu \cdot R_{p0.2}}{E}} \right]^2}. \quad (9)$$

For the load corresponding to the tensile strength (R_m), the value of true stress using the Equation (8):

$$\sigma_{Rm} = \frac{R_m}{\left[\sqrt{\frac{1}{1 + A_u - \frac{R_m}{E}} - \frac{\nu \cdot R_m}{E}} \right]^2}, \quad (10)$$

where:

A_u – uniform elongation.

3. Results of the research

Wires made of stainless steel grades 1.4310 and 1.4404 were chosen for the research. Chemical composition of tested materials is given in Table 1.

Table 1. Chemical composition of tested steels

Steel grade	C	Mn	Si	P	S	Cr	Ni	Mo
1.4310	0.08	0.91	0.68	0.028	0.001	17.96	8.42	
1.4404	0.021	1.57	0.44	0.030	0.001	16.57	11.02	2.12

Table 2. Conventional and true stresses for drawn wire made of steel grade 1.4310 determined during tensile test

Wire diameter, d_0	ϵ_d	$A_u = \Delta l / l_0$	ϵ_u	$\epsilon_d + \epsilon_u$	$R_{p0.2}$	$\sigma_{0.2}$	R_m	σ_{Rm}
mm					MPa	MPa	MPa	MPa
5.65	0	0.527	0.4233	0.4233	252.3	253.1	603.9	923.4
4.305	0.5438	0.104	0.0989	0.6427	821.6	826.5	1110.1	1226.8
3.56	0.9238	0.077	0.0742	0.9980	1054.0	1061.4	1404.8	1513.8
3.00	1.2661	0.07	0.0677	1.3337	1402.9	1415.2	1606.9	1716.8
2.50	1.6307	0.067	0.0649	1.6956	1419.2	1431.7	1701.1	1817.4
2.00	2.0770	0.064	0.0620	2.1391	1506.7	1520.7	1827.1	1945.8
1.86	2.2222	0.062	0.0602	2.2823	1640.2	1656.4	1845.1	1960.1
1.64	2.4739	0.055	0.0535	2.5275	1660.6	1677.4	2163.4	2284.5
1.499	2.6537	0.049	0.0478	2.7016	1652.7	1669.1	2177.8	2287.6

Table 3. Conventional and true stresses for drawn wire made of steel grade 1.4404 determined during tensile test

Wire diameter, d_0	ϵ_d	$A_u = \Delta l / l_0$	ϵ_u	$\epsilon_d + \epsilon_u$	$R_{p0.2}$	$\sigma_{0.2}$	R_m	σ_{Rm}
mm					MPa	MPa	MPa	MPa
5.56	0	0.507	0.4101	0.4101	224.1	224.8	533.4	802.1
4.30	0.5140	0.142	0.1328	0.6467	853.9	859.1	971.5	1110.3
3.56	0.8917	0.087	0.0834	0.9751	1064.2	1071.8	1212.3	1317.7
3.00	1.2340	0.052	0.0507	1.2847	1208.4	1217.8	1353.4	1424.6
2.50	1.5986	0.047	0.0459	1.6445	1292.3	1302.9	1432.8	1500.3
2.195	1.8588	0.044	0.0431	1.9019	1326.6	1337.7	1521.3	1589.9
2.145	1.9049	0.042	0.0411	1.9461	1363.0	1374.7	1539.5	1605.3
2.005	2.0399	0.039	0.0383	2.0782	1327.1	1388.9	1549.8	1611.0
1.845	2.2062	0.036	0.0354	2.2416	1406.4	1418.7	1578.5	1635.8
1.65	2.4296	0.035	0.0344	2.4640	1407.7	1440.4	1644.7	1702.6
1.43	2.7158	0.031	0.0305	2.7464	1462.2	1475.4	1673.9	1725.1
1.35	2.8310	0.029	0.0286	2.8596	1428.7	1502.4	1725.6	1777.1

When the drawing was finished, static tensile test was made using Instron tester type 1116. Conventional stress was determined and after calculation of actual section

– the true stresses corresponding to conventional stresses. Tests were made according to methodology described in p. 2 within the range of permanent strain, i.e. within the range of uniform elongation. Test results for both grades of steel are shown in Tables 2 and 3.

In the tables ε_d means logarithmic strain that takes place during the drawing process, and ε_u is a logarithmic strain corresponding to uniform elongation A_u . Determined values of true stress were used to trace out the flow curve of tested materials and establish mathematical form of flow stress function. The curve was used to approximate function of $\sigma_p = \sigma_{p0} + C\varepsilon^n$ type, which takes the initial value of flow stress into consideration. The flow stress functions for tested drawn wires of austenite steel are as follows:

- 1.4310 steel $\sigma_p = 253.1 + 894.6\varepsilon^{0.51}$, (11)

- 1.4404 steel $\sigma_p = 224.8 + 878\varepsilon^{0.4}$. (12)

Figures 1 and 2 show the flow curves of tested wires.

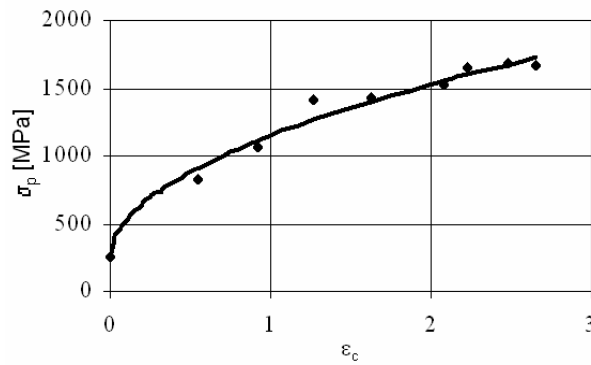


Fig. 1. Flow curve of wire made of 1.4310 steel

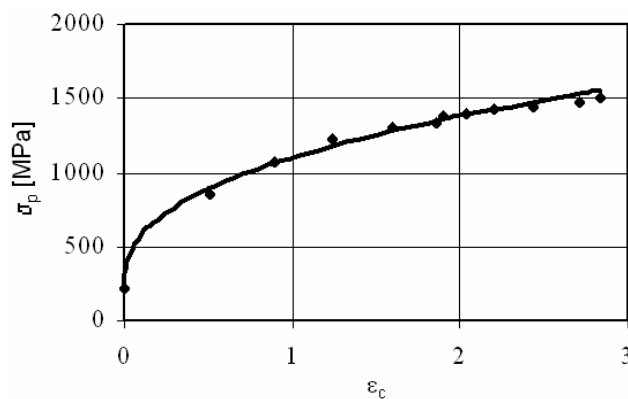


Fig. 2. Flow stress curve of wire made of 1.4404 steel

4. Summary

One formulated the relationship enabling to determine true stress during tensile test with consideration given to elastic and plastic strain. Given relationship enabled to determine true stress present during tensile test for wires made of 1.4310 and 1.4404 steels. It was ascertained that the differences of conventional and true stress levels considerably depend on the strain taking place within the range of uniform elongation. Substantial uniform elongation observed in case of wire with initial diameter ($A_r = 52.7\%$ for wire made of 1.4310 steel and $A_r = 50.7\%$ for wire made of 1.4404 steel), causes meaningful differences in the magnitude of conventional and true stress, corresponding to the tensile strength. Ultimate tensile strength of initial wire made of 1.4310 steel is 603.9 MPa, and corresponding to it true stress equals 923.4 MPa. For 1.4404 steel these values equal respectively $R_m = 533.4$ MPa, and $\sigma_{Rm} = 802.1$ MPa. When uniform elongation is smaller than 10%, the difference in both of tested steel types is of the order of 50÷120 MPa.

Initial wire tests showed very small differences in the level of conventional and true stress in case of load corresponding to proof stress. In case of wire with initial diameter, true stress is higher by 0.8 MPa (1.4310 steel) and 0.7 MPa (1.4404 steel) than conventional stress. Together with the increase of total relative section used in drawing the differences in the level of conventional and true stress amount to from a few to several MPa.

Carried calculations of true stress corresponding to conventional stress enabled to determine the course of flow curves and select the appropriate flow stress equation for the tested drawn wires of austenite steel.

The problem of proper description of material technological plasticity is closely related to the selection of optimal parameters for the wire production. Therefore the presented subject matter seems to be interesting to the technologists who design the processes of drawing. Determination of true stress is synonymous with obtaining information concerning wire plasticity reserve, which is especially important for wire products manufacturers as well as for the users of drawn materials.

Acknowledgement

Research financed from science budget in the years 2005-2006 as a research project No. 3 T08B 050 28.

References

- [1] Grosman F.: *Problemy doboru funkcji naprężenia uplastyczniającego do programów komputerowej symulacji procesów przeróbki plastycznej*, Materiały Konferencji „Plastyczność materiałów”, Ustroń, Wrzesień 1996, 11.

- [2] Grosman F.: *Zastosowanie charakterystyk technologicznej plastyczności materiałów do symulacji procesów przeróbki plastycznej*, Materiały Konferencji „Forming 2003”, Podlesice k/Kroczyń, Wrzesień 2003, 39.
- [3] Grosman F., Przędziona J.: *Metodyka wyznaczania naprężeń rzeczywistych w statycznej próbie rozciągania cienkich drutów*, Obróbka Plastyczna Metali, Vol. 15, No. 4, 2004, 5.

Wyznaczenie krzywych umocnienia drutów ze stali austenitycznych w procesie ciągnięcia

Jednym z elementów determinujących uzyskanie prawidłowych charakterystyk technologicznej plastyczności materiałów jest poprawny opis funkcji naprężenia uplastyczniającego. Krzywe zmiany naprężenia uplastyczniającego w funkcji odkształcenia pozwalają na przewidywanie zachowania się materiału w trakcie procesów przeróbki plastycznej. Dla prawidłowego ustalenia wielkości naprężenia uplastyczniającego istotnym zagadnieniem staje się precyzyjne wyznaczenie naprężeń rzeczywistych, jakim podlegają próbki drutu w trakcie realizacji próby rozciągania.

Zaprezentowane wyniki badań wykazały, w jakim stopniu wielkość naprężenia rzeczywistego, określona dla zakresu odkształceń plastycznych, różni się od naprężeń umownych wyznaczonych w próbie rozciągania. Przeprowadzone obliczenia pozwoliły na wyznaczenie przebiegu krzywych umocnienia ciągniętych drutów wykonanych z austenitycznych stali odpornych na korozję wraz z opisem funkcji naprężenia uplastyczniającego.



Deformation behaviour of low carbon deep-drawing steels influenced by phase transformation

I. SCHINDLER, M. LEGERSKI, P. SUCHÁNEK, S. RUSZ, M. JANOŠEC

Institute of Modelling and Control of Forming Processes, VŠB – Technical University of Ostrava,
17. listopadu 15, 708 33 Ostrava, Czech Republic

R. PACHLOPNÍK

Mittal Steel Ostrava a.s, Vratimovská 689, 707 02 Ostrava-Kunčice, Czech Republic

The aim was to determine the phase transformations temperatures of a specific IF steel grade, microalloyed by titanium, and quantify influence of phase composition on its deformation resistance in comparison with a common low carbon deep-drawing steel grade. In the case of the IF steel separate, sufficiently accurate, models describing mean equivalent stress after heating of the material directly to the forming temperature, matter for three temperature regions (ferrite, ferrite + austenite, or austenite), were developed.

Keywords: *IF steel, phase transformation, hot rolling, deformation resistance*

1. Introduction

Warm rolling (ferritic rolling) of low-carbon deep-drawing steels has received much attention to its potentiality broaden the product range and reduce the production costs. Interstitial-free (IF) steels with the extensively limited carbon content have become important materials in the automotive industry [1] due to their very good capability to being shaped in press. At a glance at recently issued selected publications one can be assured that research works performed in the given area are up-to-date. Their topics are e.g. rolling in the ferrite region [2,3], dynamic recrystallization of ferrite [4], investigation of deformation resistance [5], micro-structure, texture, plastic and other properties, associated with the deformation behavior in cold state [6], properties of galvanized sheets made of IF steel [7], or special methods of forming (creation of a near-surface ultra fine grain structure [8], accumulative roll-bonding [9]).

In our case the target was to determine the phase transformations temperatures of specific IF steel grade, microalloyed by titanium, and quantify influence of phase composition on its deformation resistance.

2. Experimental procedures

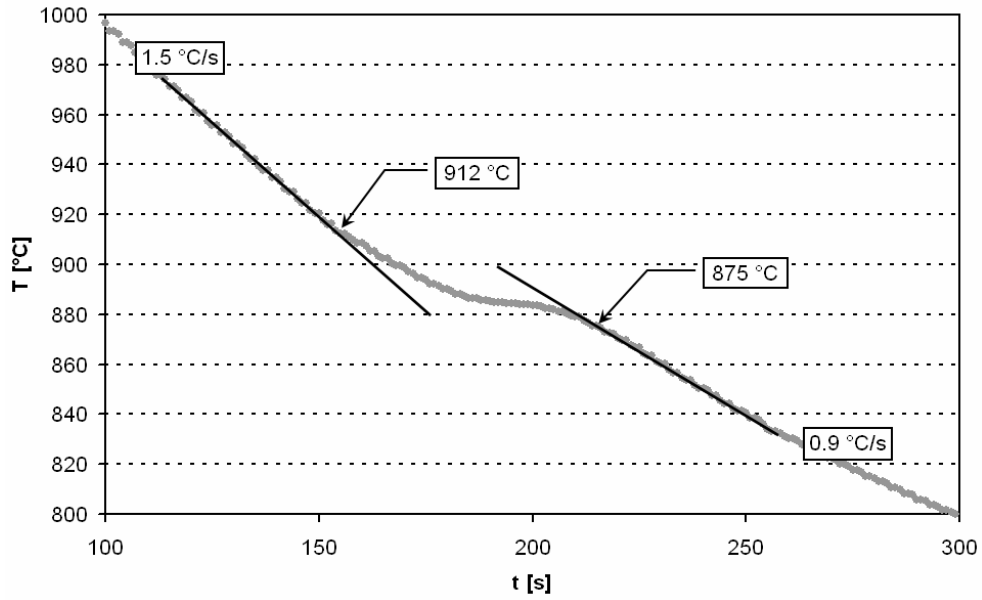
At first the interstitial-free steel (further designated as IF), with the following chemical composition in wt. %, was investigated: 0.004 C – 0.13 Mn – 0.008 Si – 0.008 P – 0.009 S – 0.041 Al – 0.003 N – 0.072 Ti. For comparison selected experi-

ments were performed also with a low carbon steel grade, killed with aluminium (designation DD), chemical composition of which was as follows (in wt. %): 0.058 C – 0.21 Mn – 0.017 Si – 0.006 P – 0.004 S – 0.046 Al.

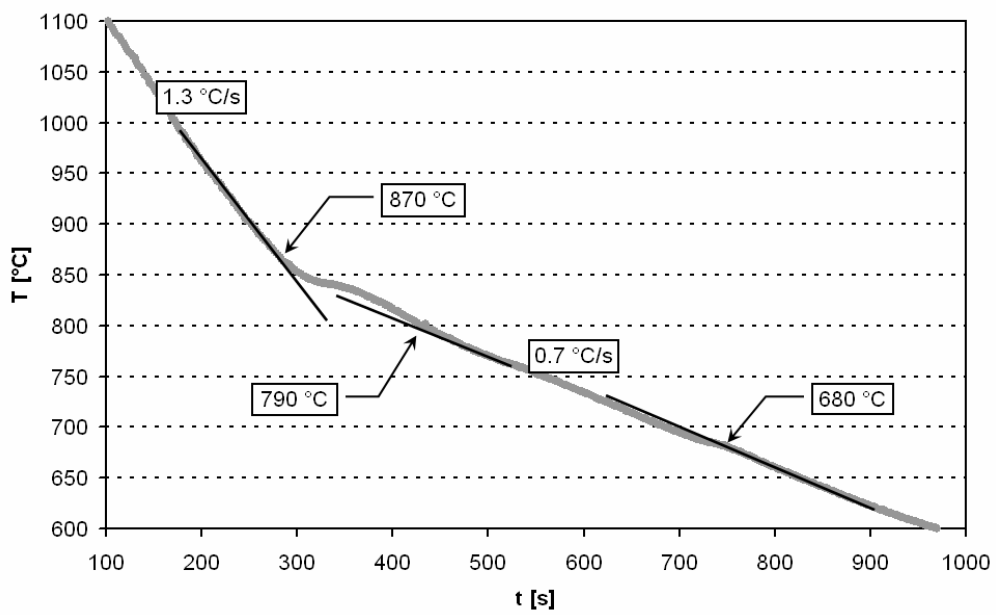
Determination of phase transformations temperatures was proceeded in two stages. At first, the inner temperature of prismatic samples with weight ca 1.5 kg and thickness 30 – 40 mm, which were cooled in the air, was computer registered [10]. Holes with diameter of max. 2.5 mm, reaching nearly a half of thickness, were drilled in these samples. Thermocouples of K type were inserted into the holes. After heating of samples, prepared in such a way, in the mobile resistance furnace LAC L09V at temperatures from 1050 to 1150 °C, the samples with thermocouples were taken out of the furnace, put on a brick and their inner temperature was measured by means of the manual thermometer OMEGA HH506R. The cooling speeds and temperatures of phase transformations, determined from changes in cooling curves, are given in graphs in Fig. 1 (where t is time [s], T is temperature [°C]).

The second work stage was based on the roll forces measurement in the course of forming samples with initial thickness of 21 mm and width of 31 mm (DD steel), or 40 mm (IF steel). Samples were heated to the temperature 1150 °C in the mobile resistance furnace CLASIC 1313LS and afterwards rolled in a set of up to 13 passes (each draught with the a height reduction of ca 12 %) and subsequently cooled in the air. The surface temperature of the rolling stock was measured before each partial reduction by pyrometer MINOLTA/LAND Cyclops 153A, computer registered and evaluated, together with roll forces. Reversible rolling was performed in the computer controlled laboratory stand K350 with arrangement of a two-high mill. Rolls with diameter 140 mm rotated with nominal speed of 100 rpm. Graphs in Figure 2 show results that were achieved in selected experiments.

In the case of IF steel the development of a model for mean equivalent stress σ_{pm} [MPa] was implemented, in dependence on the logarithmic height strain e_h , mean equivalent strain rate $\dot{\epsilon}$ [s⁻¹] (according to [11]) and temperature T [°C]. This development was realized on the basis of a methodology described earlier, see e.g. [12,13], based on the computer registration of forces F [kN] that arise during rolling of flat samples with scaled in size thickness. In this case the samples had the following dimensions: width of 25 mm, total length of 120 mm and thickness of individual stages of 4.6 mm, 5.4 mm, or 6.5 mm. The samples were heated in the resistance furnace CLASIC 1313LS directly to the forming temperature and subsequently rolled in the two-high stand A of the laboratory mill Tandem. During rolling the roll gap was differently adjusted in an appropriate way. Rolls with diameter of 158 mm rotated with nominal speed in the range of 40 to 400 rpm. An example of registered roll forces is given in Figure 3. Deformation resistance was calculated from roll forces based on knowledge of the forming factor for the particular mill stand [14]. Detailed information on the applied experimental technique can be found e.g. in [15].

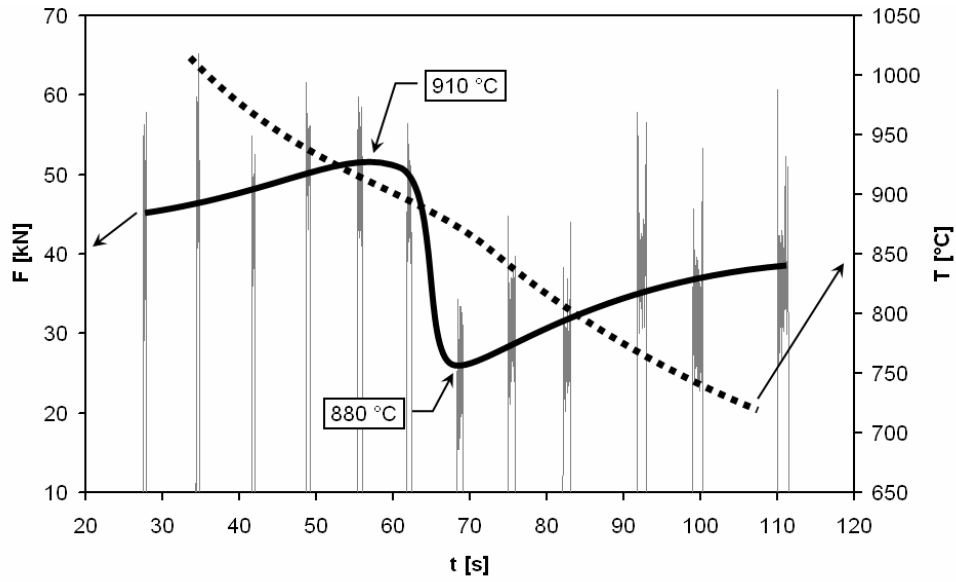


a) IF steel

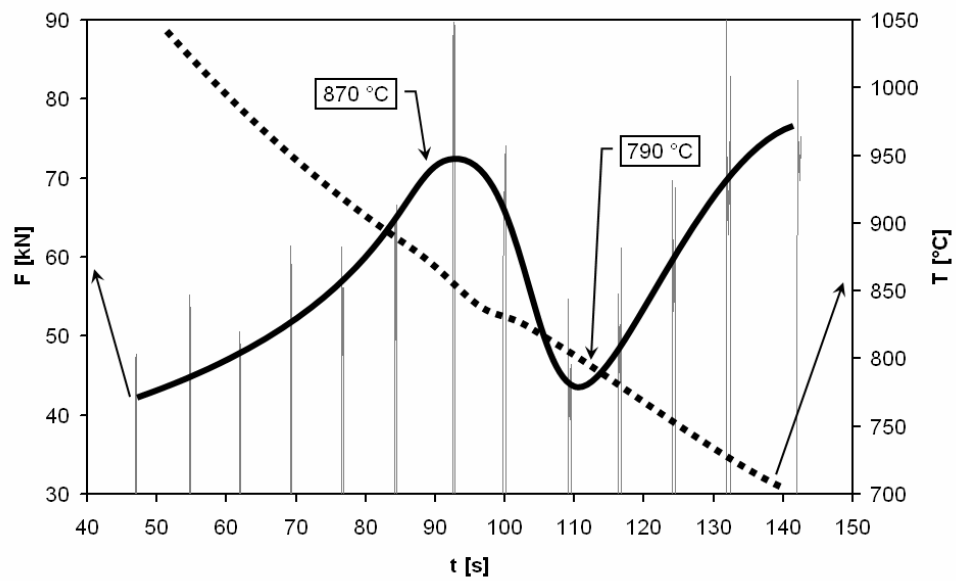


b) DD steel

Fig. 1. Cooling curves for both steels, gained from the bored-in thermocouple



a) IF steel



b) DD steel

Fig. 2. Impact of temperature and phase composition on roll forces during forming of both steels
 (a dotted line – interpolated course of surface temperature;
 a thick solid line – interpolated course of roll forces)

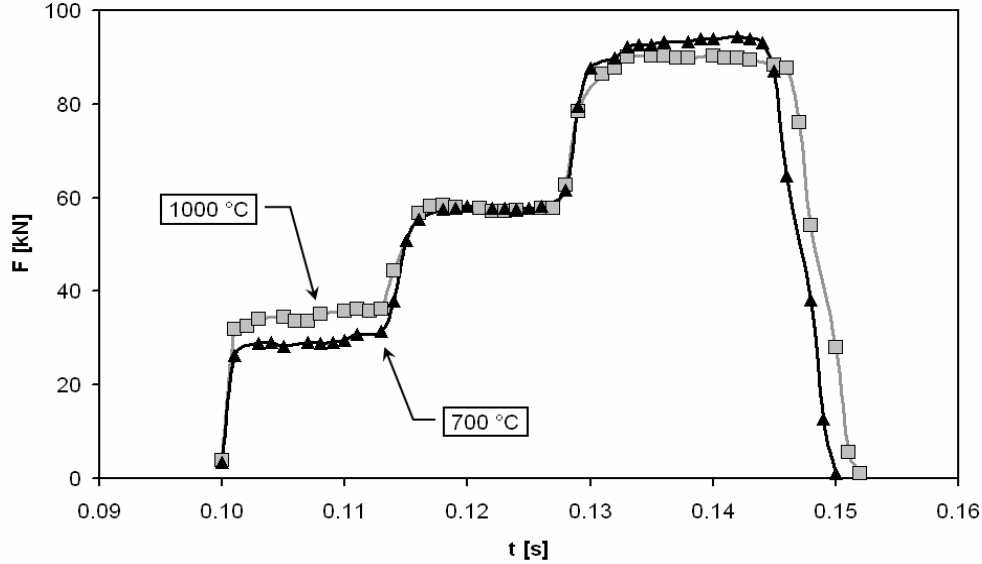


Fig. 3. Roll forces in relation to time during forming of two samples from IF steel (identical adjustment of roll gap 2.4 mm; rotation speed of rolls 400 rpm)

3. Models of deformation resistance

All values of σ_{pm} achieved by rolling of samples made of IF steel are plotted in a graph in Figure 4 in dependence on temperature. The apparently threatening scattering of experimental data is given by the fact that these values are significantly influenced also by various strains and strain rates. Moreover, despite this fact a non-monotonous influence of temperature on deformation resistance, resulting from effects of various phase composition of the material, is obvious. The mean equivalent stress cannot be described in the whole temperature range by a single equation by means of a multiple non-linear regression analysis in the program UNISTAT. Therefore particular models for three temperature regions had to be developed:

$$\text{Ferrite } (< 917 \text{ }^\circ\text{C}): \quad \sigma_{pm} = 781 \cdot e_h^{0.22} \cdot \dot{e}^{0.064} \cdot \exp(-0.0020 \cdot T), \quad (1)$$

$$\text{Ferrite + Austenite:} \quad \sigma_{pm} = 0.02 \cdot e_h^{0.19} \cdot \dot{e}^{-0.005} \cdot \exp(0.0098 \cdot T), \quad (2)$$

$$\text{Austenite } (> 959 \text{ }^\circ\text{C}): \quad \sigma_{pm} = 639 \cdot e_h^{0.16} \cdot \dot{e}^{0.082} \cdot \exp(-0.0015 \cdot T), \quad (3)$$

An idealized example of the temperature relationship of mean equivalent stress, computed according to Equations (1–3), is also given in Figure 4.

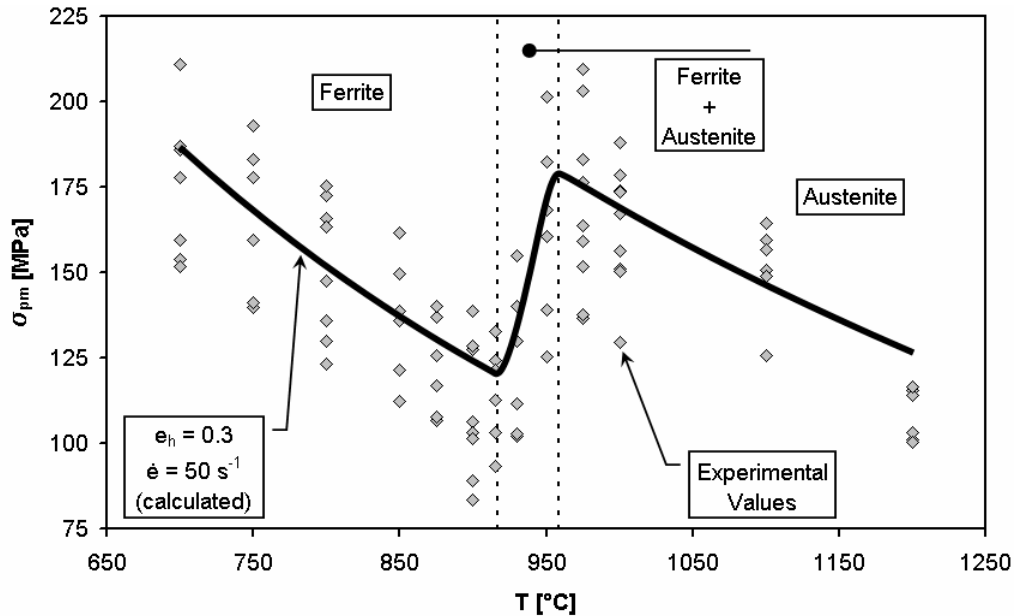


Fig. 4. Temperature dependence of mean equivalent stress, gained by rolling of all samples from IF steel, or by calculation according to Equations 1–3 for selected specific values of strain and strain rate

4. Summary of results

From the cooling curves (Figure 1) it is possible to determine, in the given conditions, temperature $Ar_3 = 870$ °C for DD steel and temperature $Ar_3 = 912$ °C for IF steel. The phase transformation austenite/ferrite should be finished at temperature 790 °C (DD steel), or 875 °C (IF steel). Furthermore for DD steel a certain trend change of the cooling curve also in the vicinity of temperature 680 °C is visible. The results reached in this way confirm theoretical assumptions. The temperature Ar_3 for IF steel is higher due to influence of various carbon contents for both investigated materials and the temperature region of transformation austenite/ferrite is significantly narrower. Data derived from the cooling curves correspond exactly with results achieved by rolling tests (Figure 2).

It follows from values of deformation resistance, calculated for orientation from roll forces, without including influence of the forming factor at repeated height reductions of ca 12 % (Figure 2), that with the decreasing forming temperature DD steel exhibits more intensive work hardening than IF steel, namely in the austenite and ferrite region. Mean deformation resistance values of both steels are at temperature 1050 °C comparable on the whole (the difference of 14 % favours the harder DD steel), but when rolling is implemented in a two-phase and also in the ferrite region the IF steel is characterized by significantly lower deformation resistance – e.g. at temperature 700

°C by ca 62 %. Due to changes in structural composition in the two-phase region the mean deformation resistance fell in the case of DD steel (on the given conditions of forming) by up to 34 % (between 870 and 790 °C), whereas in the case of IF steel it fell by up to 43 % (between 910 and 880 °C).

In the case of IF steel, separate models describing the mean equivalent stress $\sigma_{pm} = f(e_h, \dot{e}, T)$ were developed for three temperature regions (ferrite, ferrite + austenite or austenite). Their temperature limits do not exactly correspond to points of phase transformations, found out in cooling of the material, because entry data for these models were gained – with regard to the planned use of models developed in laboratory warm rolling – after heating of steel to the forming temperature.

Achieved data confirmed theoretical assumptions about decreasing in deformation resistance due to decrease in the carbon content and due to occurrence of the softer ferrite phase in low carbon steels. Relatively low deformation resistance of ferrite (see Figs. 3 and 4) can be utilized favourably in ferritic rolling of IF steel. The following stage of work will (among others) be focused on demanding mathematical description of the relationship $\sigma_{pm} = f(e_h, \dot{e}, T)$ by a single equation in a wide temperature range and under combined effects of various phase compositions.

Acknowledgement

The applied laboratory rolling devices have been developed within research plan MSM 6198910015, supported by the Ministry of Education, Youth and Sports of the Czech Republic. The models of mean equivalent stress were obtained when solving the project 106/04/1351 financed by the Czech Science Foundation.

References

- [1] Grosman F., Woźniak D.: *Technological progress of sheet production for motorization*, Hutnik – Wiadomości Hutnicze, 2002, L XIX, p. 196.
- [2] Kawalla R., Lehnert W.: *Hot rolling in ferrite region*, Scandinavian Journal of Metallurgy, 2002, 31, p. 281.
- [3] Wang Z. et al.: *Effect of Processing Parameters on Properties and Microstructure of Warm-rolled Interstitial-Free (IF) Steel Sheets*, Key Engineering Materials, 2005, 297–300, p. 477.
- [4] Ki S.I., Choi S.H., Lee Y.: *Influence of phosphorous and boron on dynamic recrystallization and microstructure of hot-rolled interstitial free steel*, Material Science and Engineering A, 2005, 406, p. 125.
- [5] Lino R.E., Barbosa R.: *Modeling stress-strain curves of hot deformed Ti-Nb interstitial free austenite*, ISIJ International, 2005, 45, p. 1758.
- [6] Chen Q.Z., Duggan B.J.: *On Cells and Microbands Formed in an Interstitial-Free Steel during Cold Rolling at Low to Medium Reductions*, Metallurgical and Material Transactions A, 2004, 35, p. 3423.
- [7] Gupta A.K., Kumar D.R.: *Formability of galvanized interstitial-free sheets*, Journal of Materials Processing Technology, 2006, 172, p. 225.

- [8] *Enhancement of reaction of zinc on superficially nanocrystallized IF steel by near surface-severe plastic deformation*, Materials Science Forum, 2006, 512, p. 361.
- [9] Costa A.L.M et al.: *Ultra grain refinement and hardening of IF-steel during accumulative roll-bonding*, Materials Science and Engineering A, 2005, 406, p. 279.
- [10] Schindler I. et al.: *Influence of phase transformation on deformation behaviour of deep-drawing and IF steels*, In Forming 2006, PS Katowice, 2006, p. 181.
- [11] Krejndlin N. N.: *Rascot obzatiy pri prokatke cvetnykh metallov*. Metallurgizdat, Moskva, 1963.
- [12] Schindler I., Marek M.: *Plasticity of metallic materials*, Deformation Behaviour, Structure Development, Testing, Modeling, Editors E. Hadasik, I. Schindler, Publishers of the Silesian University of Technology, Gliwice 2004. 244 pp. Chapter 6, *Plasticity, deformation behavior and structure development of metallic materials studied by laboratory rolling*, pp. 171–198.
- [13] Kratochvíl P., Schindler I.: *Conditions for Hot Rolling of Iron Aluminide*, Advanced Engineering Materials, 2004, 6, p. 307.
- [14] Rusz S. et al.: *Hot deformation resistance models based on the rolling forces measurement*, Acta Metallurgica Slovaca, 2005, 11, p. 265.
- [15] <http://www.fmmi.vsb.cz/model/>

Wpływ przemiany fazowej na plastyczność niskowęglowej stali do głębokiego tłoczenia

Celem badań było wyznaczenie temperatur przemian fazowych dla stali typu IF z mikrostopowym dodatkiem tytanu oraz ilościowe określenie wpływu składu fazowego na opory kształtowania, szczególnie w porównaniu ze zwykłym gatunkiem niskowęglowej stali do głębokiego tłoczenia. Zastosowano odrębne modele opisujące średnie odkształcenie zastępcze w funkcji temperatury, odkształcenia i prędkości odkształcenia dla trzech zakresów temperatur (odpowiadających występowaniu struktury ferrytu, ferrytu i austenitu oraz samego austenitu). Wartości temperatur określających te zakresy nie odpowiadają dokładnie temperaturze przemian fazowych, wyznaczanych podczas chłodzenia materiału. Wynika to stąd, że dane wejściowe dla tych modeli były uzyskane podczas nagrzewania stali do temperatury obróbki plastycznej. Uzyskane wyniki potwierdzają teoretyczne założenia o spadku oporów kształtowania w wyniku zmniejszenia zawartości węgla oraz w wyniku obecności miękkiej fazy ferrytycznej w stalach niskowęglowych. Względnie niski opór kształtowania ferrytu może być wykorzystany podczas walcowania stali IF w zakresie występowania struktury ferrytycznej.

Information for Authors

Send to: *Archives of Civil and Mechanical Engineering*
Polish Academy of Sciences, Wrocław Branch
Podwale 75, 50-449 Wrocław, Poland

Archives of Civil and Mechanical Engineering (ACME) publishes both theoretical and experimental papers which explore or exploit new ideas and techniques in the following areas: structural engineering (structures, machines and mechanical systems), mechanics of materials (elasticity, plasticity, rheology, fatigue, fracture mechanics), materials science (metals, composites, ceramics, plastics, wood, concrete, etc., their structures and properties, methods of evaluation), manufacturing engineering (process design, simulation, diagnostics, maintenance, durability, reliability). In addition to research papers, the Editorial Board welcome: state-of-the-art reviews of specialized topics, letters to the Editor for quick publication, brief work-in-progress reports, brief accounts of completed doctoral thesis (one page is maximum), and bibliographical note on habilitation theses (maximum 250 words). All papers are subject to a referee procedure, except for letters, work-in-progress reports and doctoral and habilitation theses, which are briefly reviewed by the Editorial Board.

The papers submitted have to be unpublished works and should not be considered for publication elsewhere.

The Editorial Board would be grateful for all comments on the idea of the journal.

Submit three copies, each complete with abstract, tables, and figures.

Detailed information about the Journal on web:

<http://www.pan.wroc.pl>

www.ib.pwr.wroc.pl/wydzial/czasopismoACME.html

<http://www.wmech.pwr.wroc.pl>

Price 15 zł
(0% VAT)

Subscription orders should be addressed to:
Oficyna Wydawnicza Politechniki Wrocławskiej
Wybrzeże Wyspiańskiego 27
50-370 Wrocław